THE DEVELOPMENT OF DECELLULARISED LIVER AS A NATURAL 3D SCAFFOLD FOR ORGAN ENGINEERING AND 3D-DISEASE MODELLING

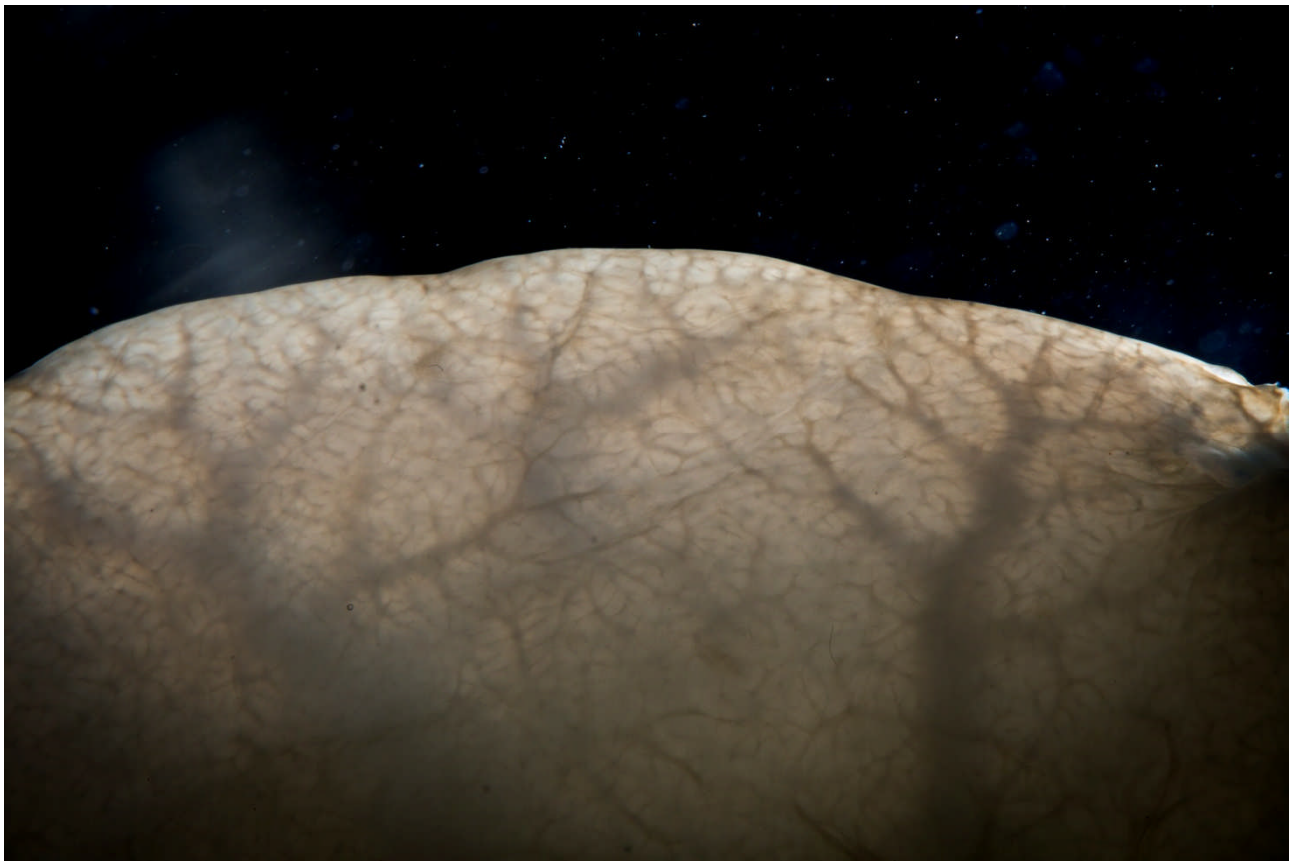

by

Giuseppe Mazza

A thesis submitted for the degree of

Doctor of Philosophy of the University College of London

Achievements

During my PhD studentship the following achievements were obtained:

Patent

UK patent application 1409858.6 filed with UCLB (2014); **Mazza G**, Malago' M, De Coppi P, Pinzani M. "Human Liver Scaffolds"

UK patent application 1513461.2 filed with UCLB (2015); Mazza G, Al-Akkad W, Pinzani M, Proctor T, Lowdell M. "Methods and device for the production of decellularised tissue scaffolds"

Publications and Written Work

- **Mazza G**, De Coppi P, Gissen P, Pinzani M. Hepatic regenerative medicine. Journal of hepatology 63, 523-524, doi:10.1016/j.jhep.2015.05.001 (2015).
- **Mazza G**, Rombouts K, Hall AR, Urbani L, Luong TV, Al-Akkad W, Longato L, David Brown D, Maghsoudlou P, Dhillon P, Fuller F, Davidson B, Moore K, Dhar D, De Coppi P, Malago' M, and Pinzani M. Decellularized human liver as a natural 3D-scaffold for liver bioengineering and transplantation. Scientific reports 5, 13079, doi:10.1038/srep13079 (2015).
- Patil SB, Vögtli M, Webb B, **Mazza G**, Pinzani M, Soh YA, McKendry R and Ndieyira JW. Decoupling competing surface binding kinetics and reconfiguration of receptor footprint for ultrasensitive stress assays. Nature nanotechnology 10, 899-907, doi:10.1038/nnano.2015.174 (2015).
- **Mazza G**, Paul S, Urbani L, Al-Shaawi R, Hall AR, Dhar D, De Coppi P, Pepys M, Pinzani P, Bellotti V, Mangione M,. Amyloid persistence in decellularized liver: biochemical and histopathological characterization. Amyloid : the international journal of experimental and clinical investigation : the official journal of the International Society of Amyloidosis, 1-7, doi:10.3109/13506129.2015.1110518 (2015)
- **Mazza G**, Al-Akkad W, Longato L, Telese A, Urbani L, Robinson B, Fuller B, Davidson B, Malago' M, Del Rio AH, De Coppi P, Rombouts K and Pinzani M. Engineering human liver 3D-biological scaffold. Manuscript in preparation. 2015.
- Sokal E, Lombard C and **Mazza G**. Mesenchymal stem cell treatment for hemophilia: a review of current knowledge. Journal of thrombosis and haemostasis : JTH 13 Suppl 1, S161-166, doi:10.1111/jth.12933 (2015).
- Arcieri R, Molinari AC, Farace S, **Mazza G**, Garnero A, Calizzani G, Giordano P, Oliovecchio E, Mantovani L, Manzoli L, Giangrande P.Uncovered needs in the management of inherited bleeding disorders in Italy. Blood Transfus Review 2014; 3:s563-6.
- Arcieri R, Molinari AC, Farace S, **Mazza G**, Garnero A, Calizzani G, Giordano P, Olivecchio E, Mantovani L, Manzoli L, Giangrande P. Present and future challenges in the treatment of haemophilia: the patient's perspective. Blood Transfus Review 2013; 4:s82-5

Posters/Presentations/Conferences

I have attended more than 50 conferences regarding hemophilia, cell therapy, liver disease and tissue engineering

- **Mazza G** et al. ISCHSR 2015 – Asilomar, California. Oral presentation number 12
- **Mazza G** et al. AASLD 2015 The 66th Annual Meeting of the American Association for the Study of Liver Diseases: The Liver Meeting 2015. Poster number 337
- **Mazza G** et al. AASLD 2015 The 66th Annual Meeting of the American Association for the Study of Liver Diseases: The Liver Meeting 2015. Poster number 1388
- **Mazza G** et al. London Liver Group 2015 - St George's Hospital. Oral presentation number 3.
- **Mazza G** et al. EASL 2015 The International Liver Congress™ 2015 – 50th Annual meeting of the European Association for the Study of the Liver. Poster number 281.
- **Mazza G** et al. AASLD 2014 The 65th Annual Meeting of the American Association for the Study of Liver Diseases: The Liver Meeting 2014. Oral presentation number 89.
- **Mazza G** et al. APAM 2014 The Annual meeting of the Association of Physicians of Great Britain and Ireland. Oral presentation number 7.
- **Mazza G** et al. BASL 2014 The Annual meeting of the British Association for the Study of the Liver. Oral presentation number A17.
- **Mazza G** et al. EASL 2014 The International Liver Congress™ 2014 – 49th Annual meeting of the European Association for the Study of the Liver. Poster number 8.
- **Mazza G** et al. UCL, Dean's Postgraduate Research Prize 2014. Oral Presentation number 5.
- **Mazza G** et al. UCL, Division of Medicine Research Retreat Day 2014 - Annual meeting. Oral presentation number 11.
- **Mazza G**. AICE 2014 The 14th Meeting of the Italian Hemophilia Center Association: The future of hemophilia research and access to therapy. Oral Presentation number 2.
- **Mazza G**. AICE 2014 The 14th Meeting of the Italian Hemophilia Center Association: The future of hemophilia research and access to therapy. Oral Presentation number 15.

Awards

- BASL Travel Award 2014
- UCL Division of Medicine Research Day 2015 : NC3R choice
- AASLD Young Investigator Award 2015
- AASLD Presidential Poster Award 2015
- EASL Young Investigator Bursary Award 2016

Declaration

I, Giuseppe Mazza, confirm that the work presented in this thesis is my own and I have either coordinated or followed the analyses which were not performed mainly by me. Where information has been derived from other sources, I confirm that this has been indicated in my thesis.

All histological and immunohistochemical analyses were performed together with Mr Andrew Rennie Hall, Department of Cellular Pathology, UCL Medical school Royal Free Campus. All animal handling described in Chapter 2 was done with Dr Dipok Dhar, UCL Institute for Liver and Digestive health and I observed the procedure. Tissue samples for scanning electron miscroscopy were processed by Dr. Luca Urbani, UCL Institute of Child Health. All cell culture was performed together with Prof. Res. Ass. Krista Rombouts. All proteomic analysis was performed by Dr Graham Taylor, UCL Center for Amyloidosis and Acute Phase Proteins.

The transgenic mice employed in Chapter 2 were provided by Dr Paul Simons and Dr Raya Al-Shawi. The protein composition of amyloidotic and healthy mice liver scaffolds was performed together with Dr. Patrizia Mangione. The amyloid enhancing factor activity was performed by Dr.Stephen Ellmerich, UCL Center for Amyloidosis and Acute Phase Proteins.

All biomechanical analysis described in Chapter 3 were performed by Dr. Benjamin Robinson, Imperial College. The CAM assay was done by Dr. Luca Urbani. The Raman spectroscopy analysis was performed by Professor Ioan Nottingher and Dr. Kenny Kong, University of Nottingham School of Physics and Astronomy. The gene expression analysis was performed together with Dr Lisa Longato, UCL Institute for Liver and Digestive Health.

Signed

Acknowledgments

I would like to thank my supervisor Professor Pinzani, for his constant help and care for my academic development. I would like to thank you for encouraging my research and for allowing me to grow as a junior research group leader. In fact, without his faith in me none of this would have been possible.

I am also hugely appreciative to my co-supervisors Professor Clare Selden and Professorial Research Associate Krista Rombouts, for their continuous support and guidance. Indeed, their constant advice and help has been priceless.

I would also like to thank my colleagues Professor Paolo De Coppi, Mr Max Malago', Mr Andrew Hall, Dr Dipok Dhar, Dr. Lisa Longato, Dr Amir Gander for their mentoring and support since the beginning of my PhD.

In addition, I would like to thank Professor Vittorio Bellotti, Dr Patrizia Mangione, Dr Raya Al-Shawi and Dr Paul Simons for their continuous support for the development of the "amyloidosis-ECM interaction" project.

A big thank to all my friends and students who I have been supervising during these past 3 years. Thank you to: Walid Al-Akkad, Andrea Telese, Luca Frenguelli, Marco Curti, Oliver Willacy, Gabriele Spoletini, Domenico Tamburrino. *Grazie mille!*

Last but not least, a special thanks goes to my family (Rocco, Sara, Francesca, Michele, Sara jr. and Elisa) for your tremendous support and love during my PhD and in my life. You are the most important people in my world and I dedicate this thesis to you.

Table of contents

List of figures

List of tables

Abbreviations

AA-mL – Amyloid A protein-mouse Liver

AA-mL$_{dec}$ – Amyloid A protein-mouse Liver from decellularised tissue

AB – Alcian blue

AEF – Amyloid enhancing factor

ALD – Alcoholic liver disease

αSMA – alpha-smooth muscle actin

AFP – alpha feto protein

AFM – atomic force microscope

3D – three-dimensional

BD – Bile duct

CAM – chicken chorioallantoic membrane angiogenic assay

CHAPS - 3-[(3-cholamidopropyl)dimethylammonio]-1-propanesulfonate

CLD – chronic liver disease

DET – detergent-enzymatic treatment

dH2O – distilled water

ECM – extra-cellular matrix

EDTA – ethylene diamine tetra-acetic acid

EGF – epidermal growth factor

EVG – verhöff's van gieson

FGF – fibroblast growth factor

GAG – glycosaminoglycans

HA – hepatic artery

H&E – haematoxylin & eosin

HCC – hepatocellular carcinoma

HSC – hepatic stellate cells

HVG – haematoxylin van gieson

IVC – inferior vein cava

IDA – industrial denatuarated alcohol

LSEC – liver sinusoidal endothelial cells

LSC – liver scaffold

LTC –liver tissue cubes

NaCl – sodium chloride

NPC – non-parenchymal cells

PAA/EtOH – paracetic acid and ethanol

PBS – phosphate buffered saline.

PBS/AA – phosphate buffered saline + antibiotic + antimycotic

PIPAAm – poly(N-isoproplyacrylamide)

PLA – poly(l)-lactic acid

PGA – poly-glycolic acid

PLGA – poly-lactic-co-glycolic acid

PDGF-β – platelet perived growth factor –β

PV – portal vein

RA – recipient adipose tissue

RI – recipient intestine

rpm – revolutions per minute

RO – recipient omentum

RS – recipient skin

RT – room temperature

SAA – serum amyloid A protein

SEM – scanning electron microscopy

SDC – sodium deoxycholate

SDS – sodium dodecyl sulphate v/v – volume/volume

SIS – small intestinal submucosa

SR – picro-sirius red

TEM – transmission electron microscopy

TGF-β – tumour growth factor-β

TPPS – 5,10,15,20-tetraphenyl-21H,23H-porphine tetrasulfonate

VEGF – vascular endothelial growth factor

w/v – weight/volume

Chapter 1: General Introduction

1.1. Human liver anatomy

1.1.1. Liver anatomy and main functions

The liver is the largest organ in the human body and is located in the upper right abdomen[1]. The liver contributes to the maintenance of the homeostasis and metabolism in the organism[2] and filters the blood from the digestive tract before it is delivered to the systemic circulation. Furthermore, the liver metabolises drugs and detoxifies chemicals while producing several vital molecules such as blood-clotting proteins and bile. In addition, the liver accumulate glycogen as energy store and has a key role in protecting the body from foreign antigens and gut-derived[1,2] microbes.

1.1.2. Liver cell types and liver Extra Cellular Matrix (ECM)

The main cell type in the liver are hepatocytes, or liver parenchymal cells, that constitute up to 80% of the entire liver mass carrying out most of the hepatic functions[3]. The remaining 20% of the liver mass is characterized by non-parenchymal cells (NPCs) and namely Hepatic Stellate Cells (HSC), Liver Sinusoidal Endothelial Cells (LSECs), Kupffer cells, and different types of immune cells (e.g. natural killer cells) [4].

The different cell types of the liver are organised within the microvascular unit, named sinusoid. The sub-endothelial space of Disse divides the epithelium (hepatocytes) from the sinusoidal endothelium. In normal liver this space is characterized by basement-membrane matrix, although it has a higher capability of exchanging nutrients compared to other basement membrane. This key feature allows the maintenance of the differentiated function of hepatic cells. During liver

fibrosis, the composition of hepatic ECM is dramatically affected both at qualitative and quantity level. Indeed, the amount of ECM proteins increases 3-5 fold and the basement membrane is characterized by increased density composed of fibrillary collagens (Figure 1.1)[5].

The different NPC have a distinct and specific role in addition to providing support to the specialised work of liver parenchymal cells. Hepatic Stellate Cells, liver specific pericytes, store Vitamin A and play an essential role in the physiology of the space of Disse where they are located [6]. In response to liver injury HSC undergo a phenotypic transformation from "quiescent" cells (non-proliferating and non-contractile), into "activated" cells characterized by markedly increased cell proliferation, contractility and increased secretion of extracellular matrix (ECM)[7,8]. Accordingly, HSC are considered the key cellular effectors of liver fibrogenesis following chronic tissue injury[5,8,9].

The hepatic ECM is mainly composed by fibronectin, collagen type I, and minimal amounts of collagen type III, IV, V, and VI[10]. The liver ECM, in its biochemical and biomechanical integrity, has a critical role in maintaining the healthy phenotype of both hepatocytes and NPCs[10]. It is evident that the progressive changes in the composition and 3D structure of the liver ECM occurring in chronic fibrogenic disorders of the liver markedly affect the biology of hepatocytes, cholangiocytes and NPCs and ultimately represent key factors towards the evolution to liver cirrhosis[11,12].

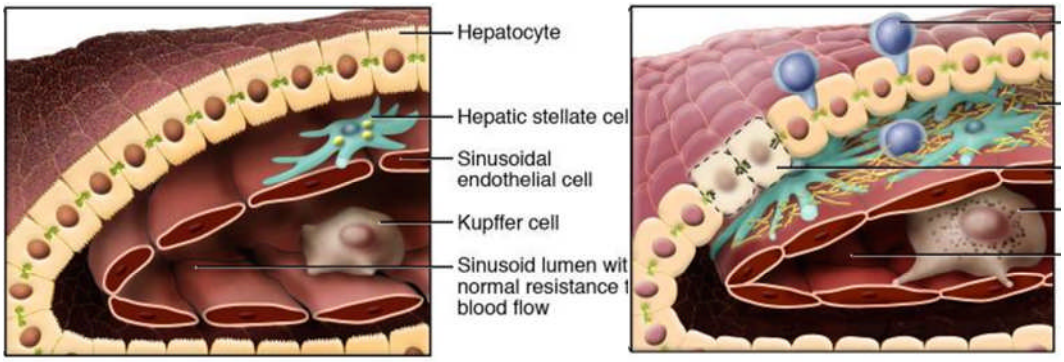

Figure 1.1 Scheme of a healthy liver sinusoid where hepatic stellate cells (HSC), residing within the Disse Space between sinusoidal endothelial cells (LSECs) and hepatocytes; store retinoids within lipid droplets. (D) Upon liver injury, stellate cells become activated

and secret higher levels of extracellular matrix (ECM) proteins. Image modified from Friedman et al 2004[5]

1.2. Chronic liver diseases (CLD) evolving to cirrhosis and potentially requiring liver transplantation

Liver disease affects almost 2 million people in UK[13]. Most liver diseases have a chronic fibrogenic evolution leading to an advanced stage commonly defined as cirrhosis. Cirrhosis is defined as a pathological stage characterised by the accumulation of fibrillar ECM and by a marked alteration of the vascular architecture of the liver with the establishment of abnormal communications between the portal system and the hepatic veins associated with a marked arterialisation of the liver tissue[14]. These changes lead to the development of portal hypertension which is the main cause of the clinical complications of cirrhosis leading to end stage liver disease. More than 4,000 people in the UK die each year from cirrhosis. The most common chronic fibrogenic liver diseases potentially leading to cirrhosis and liver failure are:

1. **Chronic viral hepatitis due to a chronic hepatitis B or C virus infection**. HBV is the most common among those hepatitis viruses that cause chronic infections of the liver in humans, and it represents a global public health problem. Chronic hepatitis caused by HBV is the leading cause of cirrhosis worldwide and approximately one-quarter of patients with cirrhosis develops decompensated liver disease within 5 years[15,16]. In addition, chronic HBV infection is the major cause of HCC worldwide[17]. Approximately 15 million of the estimated 350 million individuals with chronic HBV infection have evidence of exposure to hepatitis D (delta) virus (HDV), which requires hepatitis B surface antigen for transmission and packaging[18]. HBV/HDV co-infection is associated with more severe acute hepatitis and higher mortality than acute HBV mono-infection. Chronic co-infection is clearly associated with a higher risk of cirrhosis and decompensated liver disease. Hepatitis B and all of the complications resulting from it, as well HDV and its complications, are globally preventable by hepatitis B vaccination,

and therefore elimination of HBV transmission and of new acute and chronic infections appear to be a feasible goal.

Worldwide, an estimated 130–170 million people have HCV infection[19,20]. Differences in past HCV incidence and current HCV prevalence, together with the generally protracted nature of HCV disease progression, has led to considerable diversity in the burden of advanced liver disease in different countries around the globe. Morbidity and mortality rates from chronic HCV infection will increase because the infection incidence peaked in the mid-1980s and because the liver disease progresses slowly and is clinically silent to cirrhosis and end-stage-liver disease over a 15-20 year time period for 15%-20% of chronically infected individuals. About 75% of patients infected by HCV will develop a chronic HCV infection and are subsequently at risk of progression to hepatic fibrosis, cirrhosis and HCC[21]. Chronic hepatitis C generally progresses slowly in the initial two decades, but can be accelerated during this time as a result of advancing age and co-factors such as heavy alcohol intake, HIV co-infection, obesity/diabetes and hereditary haemocromatosis[22]

2. **Non-alcoholic fatty liver disease (NAFLD).** In the UK as well as in other industrialised Countries, it is estimated that 20-30% of the population is affected by NAFLD[23]. NAFLD can range from a condition defined as "simple fatty liver" characterised by triglyceride vacuoles accumulation in hepatocytes to a condition defined non-alcoholic steatohepatitis (NASH) branded by the presence of cell necrosis, inflammation and progressive fibrosis leading to the development of cirrhosis. Five to 20% of patients with NAFLD develop NASH, which undergoes a further transition to higher-grade fibrosis in 10% to 20% of cases[24]. In fewer than 5% of cases, fibrosis progresses to cirrhosis. These approximate figures lead to an estimate of 0.05% to 0.3% for the prevalence of cirrhosis in the general population. Moreover, NAFLD can progress to hepatocellular carcinoma also in the absence of apparent cirrhosis[21,25]. In general NAFLD and NASH are associated with other clinical manifestations of the so-called "metabolic syndrome" (insulin resistance, dislypidemia, and high blood pressure). NASH is predicted to become the leading cause of liver transplantation in the USA and likely in Europe by the year 2020[24]. The increasing burden of NAFLD and the

current lack of effective treatments to halt or reverse disease progression in patients with NASH have led to intense investigation into the basic mechanisms involved in the development and progression of the disease. The most accepted concept outlining the pathogenesis of NAFLD implies the occurrence of parallel events ('hits') that involve a complex interaction and crosstalk between environmental factors, host genetics and gut microflora[26]. This interaction might promote isolated steatosis, cell death or progressive liver damage, innate immune activation, inflammation and fibrosis.

3. **Alcoholic liver disease (ALD).** Liver damage and fibrosis due to excessive consumption of alcohol are one of the most common causes of cirrhosis and liver failure in the UK. Incidence rates of ALD in the UK have increased alarmingly in recent years with death rates rising from 3,236 in 2002 to 4,400 in 2008[27]. The association between alcohol intake and alcoholic liver disease has been well documented, although cirrhosis of the liver develops in only a relatively small proportion of heavy drinkers[28]. The risk of cirrhosis increases proportionally with consumption of more than 30 g of alcohol per day, and the highest risk is associated with consumption of more than 120 g per day[28]. Similarly to NAFLD, the pathological manifestations of ALD range from simple fatty accumulation in hepatocytes, to marked cell necrosis associated to inflammation and fibrosis (i.e. alcoholic steatohepatitis: ASH) to full blown cirrhosis. Importantly, the clinical course of ALD is characterized by frequent episodes of acute on chronic damage or even episodes of frank acute liver failure that represent an important emergency in hepatology.

4. **Other chronic liver diseases.** Other less common chronic liver diseases characterised by fibrogenic progression and evolution to cirrhosis are autoimmune hepatitis (AIH), primary biliary cholangitis (PBC, previously defined primary biliary cirrhosis) and primary sclerosing cholangitis (PSC). Autoimmune hepatitis is a chronic inflammatory disease of the liver that occurs worldwide with a low but probably underestimated prevalence. Although AIH typically affects young

and middle-aged women, it can occur in both sexes and across all age groups[29]. Prognosis of severe AIH is poor if untreated. The pathogenesis is complex, combining environmental factors (external chemical or infectious triggers) and host genetic susceptibility. Primary biliary cirrhosis is a chronic, progressive, cholestatic, organ-specific autoimmune disease of unknown aetiology. It predominantly affects middle-aged women, and is characterized by autoimmune-mediated destruction of small- and medium-size intrahepatic bile ducts, portal inflammation and progressive scarring, which without proper treatment can ultimately lead to biliary fibrosis and hepatic failure. Currently, it is believed that PBC is likely to be triggered by a combination of environmental factors including infection in a genetically susceptible individual[30,31]. Primary sclerosing cholangitis is a chronic cholestatic disease of the liver that is characterized by progressive inflammation, fibrosis, and stricturing of the intrahepatic and extrahepatic bile ducts leading to cirrhosis[32]. PSC likely, which occurs in genetically susceptible individuals, perhaps after exposure to environmental triggers, is a rare disease, mostly affecting people of northern European descent, males greater than females. Inflammatory bowel disease (IBD) is present in ~75% of the patients with PSC, mostly ulcerative colitis (~85% of the cases). In addition to biliary fibrosis and cirrhosis, complications of PSC include dominant strictures of the bile ducts, cholangitis, and cholangiocarcinoma.

Aetiology-dependent fibrogenic patterns of evolution to cirrhosis. It is increasingly clear that different CLD are characterised by different predominant pro-fibrogenic mechanisms and, while cirrhosis is the common result of progressive fibrogenesis, there are distinct patterns of fibrosis development in different and even within the same CLD. These aetiology-related patterns are linked to the relative prevalence of different pro-fibrogenic mechanisms, such as the activation of a chronic wound healing reaction, oxidative stress and derangement of the epithelial-stromal equilibrium around bile ducts. The pattern of fibrosis development typical of chronic viral hepatitis or of autoimmune hepatitis is considered the results of portal-central (vein) bridging necrosis, thus originating portal-central septa. In addition, this form of fibrogenic evolution is characterized by the presence of “interface” hepatitis and development of portal to

portal septa and septa ending blind in the parenchyma, and by rapid derangement of the vascular connections with the portal system (early portal hypertension)[34]. Chronic viral hepatitis and autoimmune hepatitis are characterized primarily by chronic hepatocellular necrosis and apoptosis. Consequently, the main drive of fibrogenesis is a typical chronic would healing reaction. This process, which is highly efficient in the presence of single acute tissue insult, leads to progressive scarring when tissue damage is chronic. In other words, deposition of fibrillar matrix rather than organized tissue regeneration becomes the best option in order to maintain tissue continuity. In addition to chronic hepatocellular necrosis and apoptosis, hepatic fibrogenesis due to the chronic activation of the wound healing reaction is characterized by the following key features: 1) a complex inflammatory infiltrate including mononuclear cells and immunocompetent cells; 2) the activation of different types of ECM-producing cells (HSC, portal myofibroblasts, etc.) with marked proliferative, synthetic and contractile features; and 3) marked changes in the quality and quantity of the hepatic ECM associated with very limited or absent possibilities of remodeling and regeneration[33,34].

The general pathological features of liver fibrosis developing in ASH and NASH are very similar, if not indistinguishable. Typically, fibrosis is initially limited to lobular zone 3 and is concentrated around the sinusoids (capillarization) and around groups of hepatocytes (chicken-wire pattern) on a general background of hepatocellular steatosis/ballooning with different degrees of lobular inflammation. This pericellular fibrosis eventually forms septa isolating regenerating nodules leading to a picture typical of cirrhosis. Although the mechanisms underlying fibrosis in ALD and NAFLD are in part common to those observed in other chronic liver diseases ("core pathways" of hepatic fibrogenesis), there are specific "regulatory pathways" for ASH and NASH. In both conditions, oxidative stress-induced inflammation and fibrosis play a central role in the progression of the disease[35]. In alcoholic liver injury, for example, acetaldehyde, the main metabolite of ethanol, is able to increase gene transcription and synthesis of different ECM components in activated hepatic stellate cells (HSC)[36]. In addition to acetaldehyde, products of lipid peroxidation generated by exposure to ethanol or the production of iron overload may also perpetuate HSC activation. Along these lines, stimulation of lipid peroxidation or exposure to 4-hydroxynonenal (4-HNE), a

highly reactive aldehydic end-product of lipid peroxidation, increases procollagen I gene expression in activated human HSC[37,38].

The difference in the patterns of evolution underlines the prevalence of different fibrogenic mechanisms and different cellular effectors of fibrogenesis. Accordingly, the natural history of disease associated with a cirrhotic liver caused by chronic alcohol abuse could be markedly different when compared to a cirrhotic liver caused by chronic viral hepatitis. The knowledge of these aspects of the pathophysiology of CLD leads to the awareness that a correct interpretation of the development of cirrhosis should take into consideration the correlation between time of progression of liver disease, the aetiological agents, the dynamics of the necro-inflammatory infiltrate, the distribution of fibrosis and the onset and progression of portal hypertension depending on the aetiological agent[39].

Hepatocellular carcinoma (HCC). Hepatocellular carcinoma represents a frequent complication of cirrhosis and more than 4,000 new cases are diagnosed each year in the UK[40]. As for any other type of cancer, the mechanisms leading to HCC are characterised by mutations of the genes regulating cell replication and the relationship between cells and the surrounding microenvironment. These mutations are amplified in number and occurrence since the liver has a natural tendency to regenerate and the presence of chronic damage leads to a continuous regenerative stimulus. For this reason, a large proportion of patients with cirrhosis develop HCC during the long clinical course of chronic hepatitis and cirrhosis.

The most radical treatments for HCC are represented by liver transplantation that resolves also the underlying cirrhosis, and the surgical resection of the tumour. In patients who are not candidates for liver transplantation or resection, tumor ablation can be offered to extend life and to potentially downstage the tumor to permit transplantation or resection.

1.3. The treatment of end-stage liver diseases: need for new treatment strategies

As previously mentioned , liver disease is currently the 5th most common cause of death in UK[41]. Unfortunately, liver transplantation is the only effective treatment for patients with end-stage liver disease[42] but it is limited by both high cost and severe shortage of donor organs. Indeed, almost 11,575 patients die each year in the UK while waiting for a liver transplant[43].

Thus, there is an unmet need to develop new treatments for liver diseases as a potential alternative to donor-liver transplantation.

1.4. Tissue engineering of the liver

Over the last decades several studies have demonstrated the suitability of techniques enabling to the decellularisation of human and animal tissues thus providing the basis for tissue engineering employing naturally occurring ECM scaffolds. In this context, liver bioengineering has potential for transplantations and for toxicity testing during preclinical drug development. There is indeed convincing experimental evidence that "Decellularisation-Recellularisation" technologies provide a valuable platform for liver bioengineering through the repopulation of a liver ECM scaffold with appropriate parenchymal and non-parenchymal liver cells.

In 2010, Shupe *et al.* firstly reported the methodology for the decellularisation of rodent livers highlighting the need of employing SDS in the decellularisation process to effectively remove any cellular components, specifically DNA[44].

During the same period, Uygun *et al.* described an efficient perfusion-decellularisation method able to successfully preserve the vascular network. The acellular translucent scaffold was then infused with rat-derived hepatocytes through perfusion of the portal vein. Approximately 12.5 million of cells were introduced during each of the four steps repeated at ten-minute intervals. The recellularised grafts were maintained in a perfusion chamber for up to 2 weeks in vitro. This was the first report providing evidence of the level of functionality of the hepatocytes grown on a decellularised 3D ECM scaffold[45].

The report by Baptista et al. firstly demonstrated the possibility of repopulating decellularised pig right lobes with human hepatocyte progenitors[46]. Subsequently, Barakat et al developed a method to decellularise whole porcine livers, to be repopulated with human cells with the goal of producing a clinically relevant model of liver bioengineering. Foetal hepatocytes co-cultured with foetal stellate cells were seeded within the pig liver ECM scaffold and the constructs were perfused up to 13 days. Liver organoids showed active metabolism and preserved capability to synthesize albumin, and were able to sustain physiological blood pressure without harm[47] .

While the primary goal for liver tissue bioengineering is to reproduce a functional organ suitable for transplantation in recipient hosts, there is increasing interest for using this technology for more immediate applications and particularly the creation of an advanced disease modelling platform for preclinical drug development and drug toxicity testing.

1.5. Current in vitro and in vivo disease modelling for chronic liver diseases and liver cancer

The development of new drugs for the treatment of liver disease has been limited during the last decades due to the lack of more physiological models in which human cell biology and pathogenesis can be investigated.

1.5.1. Two-dimensional (2D) *in vitro* models

To date, plastic 2D monolayers are commonly used to identify molecular targets for drug development as well as to test treatments for liver diseases[48,49]. Recent advances of *in vitro* hepatocyte models have involved the pre-treatment of plastic surface with ECM proteins such as collagen biomatrices, proteoglycan derivates, soft collagen and Matrigel. However, hepatocytes cultured in this 2D-ECM coated

systems show reduced hepatocyte-specific functions such as ammonia metabolism, hepatic transport activity, albumin secretion and polarity[50].

Because of these limitations, a novel culture system was developed in which hepatocytes are placed between collagen type I layers ("2D sandwich")[51]. However, this system lacks of 3D organization, is degradable and characterized by high variability[52,53]. Practically, the main limitation of standard 2D monolayers is that they do not recapitulate the physiological hepatic 3D microenvironment. As a consequence, 2D cell culture models are not reliable for providing extrapolative data of *in vivo* responses[54-56]. In addition, drug candidates showing high efficacy in 2D systems did not replicate their efficiency *in vivo*[57].

1.5.2. Animal models

Animal models have been largely explored for developing drug compounds during last three decades[58]. These systems overcome some of the 2D models' limitations by providing essential physiological features such as hepatic microenvironment, three-dimensional(3D) architecture and cellular heterogeneity[59]. However, none of the existing human chronic liver diseases can be fully reproduced in an animal model. In addition, animal models are limited in predicting drug effectiveness because of the interspecies differences in gene and protein expression with humans. Indeed, these differences can alter the evaluation of drug pharmacokinetic, drug metabolism and disease adaptive mechanisms[60,61].

In addition, these models are expensive, time-consuming and animal testing have raised several ethical criticisms.

1.5.3. The need for more accurate *in vitro* systems

As mentioned above, *in vitro* and *in vivo* models are inefficient in recapitulating the complexity of human physiology. This is confirmed by the high failure rate of drug candidates in advancing through clinical trials[62] mainly due to unexpected toxicity or lack of clinical benefits in humans[63].

Thus, the development of new systems for modelling human diseases is strongly

required in order to improve the prediction of drug targets, safety and to reduce drug development costs.

Therefore, several researchers have focused their attention on developing *in vitro* 3D-tissue specific platform for recapitulating the complexity of tissue microenvironment that could be potentially scaled up to high throughput screening (HTS) platform for evaluating new compounds/molecules and therefore reducing animals requirement[64].

1.6. 2D vs. 3D in vitro systems: the role of the microenvironment in cell phenotype

Several studies have shown that hepatic 3D cultures show a better correlation with the *in vivo* cellular response compared with 2D systems[65,66]. Indeed, 3D models enable the maintenance of essential features of tissue microenvironment such as cell-matrix and cell-cell interactions, ECM protein composition, tissue-specific mechanical cues, topography and 3D microarchitecture. Therefore, 3D models are considered more suitable for evaluating cell biology and investigating drug targets than 2D culture systems.

1.6.1. Cell–cell interactions and co-culture systems

Differentiation, migration and proliferation are key cellular functions strongly regulated by signals from other cells[67].

Therefore, an ideal *in vitro* model needs to resemble tissue specific cell-cell interactions to improve drug screening outcomes. 3D culture systems enable the establishment of platform in which cell-cell interactions can be fully investigated within 3D microenvironment[68,69]. The morphology and spatial organization maintained within 3D culture systems allow for preservation of natural adhesion between cells and this process is mainly mediated by cadherin proteins. Besides their organizational role, cadherins transduce mechanical signals within the cells

which in turn regulates gene expression signalling pathways[70]. Therefore, key signalling pathways are maintained in 3D cultures and better resemble the in vivo scenario when compared to 2D systems.

Furthermore, cellular heterogeneity is an essential feature of all tissues and therefore it is crucial to recapitulate the interactions between different cell types in order to reproduce the *in vivo* complexity thus enabling a full assessment of key molecular pathways *in vitro*. This has been demonstrated in several studies demonstrating a superior correlation with *in vivo* cellular phenotype by employing co-culture rather than monoculture systems. For instance, 3D co-culture of hepatic stellate cells with hepatocytes has been shown to influence several cellular functions such as engraftment, proliferation and differentiation[71-73].

1.6.2. Cell-ECM interactions

The interaction between ECM proteins and cellular receptors influence different physiological and pathological processes[74,75]. This interaction leads to series of chemical and mechanical stimuli which may affect the phenotype and function of both ECM and cells[76,77]. Thus, recreating human tissue-specific ECM composition and architecture represents an area of research actively pursued in medicine and biology for improving the quality and validity of data generated from *in vitro* cultures.

Integrins are transmembrane receptors with a key role in mediating the interaction between cell and ECM by connecting ECM receptors with both cell membranes and nucleus.

These proteins allow continuous regulation of cellular mechanisms in response to environmental stimuli[78] by regulating cell survival, motility, migration, invasion, cytoskeletal arrangement and gene expression[79].

Moreover, integrins are able to sense changes in ECM biomechanical properties (e.g. liver fibrosis and cirrhosis) during liver fibrosis and cirrhosis.

Therefore, changes in biomechanical features of tissues or materials may affect integrin signalling pathways[80]. This has been showed by researchers which highlighted significant differences in signalling pathways of cells cultured in 2D and 3D models[76,81] leading to different cell response after drug treatment.

1.6.3. Tissue architecture and oxygenation

Tissue architecture and topography has been shown to orchestrate several cellular functions such as cell morphology, differentiation, polarization and gene expression [82]. Therefore, the development of 3D culture models needs to resemble the complexity of spatial organization of human tissues. Indeed, the cellular interaction with ECM proteins is mediated through the binding of both apical and basal membrane with layers of ECM structural proteins. Unfortunately, these bi-directional interactions are absent or disrupted in 2D models[83].

In addition, oxygenation plays a key role in preserving cell function and the process of oxygen distribution is mediated by blood vessels and capillaries *in vivo.* Indeed, a key limitations of *in vitro* culture is the capability of generating vascularized microtissue considering that the maximum distance between cells and vessel is between 150 and 200 μm *in vivo*[84]. Moreover, oxygen level mediates key cellular functions because its alteration (e.g hypoxia) affects cell proliferation and metabolism[85].

This parameter is not considered in 2D culture system because it is not possible to recreate the oxygen gradient which characterize biological tissues[86].

Therefore, the design of 3D *in vitro* platform requires mimicking the tissue-specific oxygen and nutrient gradients in order to satisfy the tissue-specific metabolic request.

1.7. 3D *in vitro* hepatic systems

During last decade, advanced liver 3D models have been established for engineering hepatic tissue by employing cell spheroids, cell sheets and scaffold-based 3D-cultures aiming at recreating the physiological and pathological hepatic microenvironment[87]. These models are summarized in the next sections highlighting key features that require optimization.

1.7.1. Spheroids

This system allows the development of 3D hepatocyte culture by suspending those cells in an appropriate medium and represents one of the first models developed [88]. Hepatocytes grown in 3D spheroids form multicellular clusters that produce ECM and therefore allow cell-ECM and cell-cell interactions[89,90]. Therefore, this 3D system has been proved to preserve hepatic-specific functions and differentiation rather than 2D culture systems[91]. In addition, 3D spheroids allow the study of drug pharmacokinetics and toxicity in order to identify the most appropriate dose[92].

However, the main limitation of this system is the difficulty to standardize the size of the spheroids which is a key condition for reproducing data gathered during drug efficacy and toxicity studies. Furthermore, the assembly of 3D spheroids requires long time[89].

1.7.2 Cell sheet stacking

The temperature-responsive culture surface can be developed by implanting a temperature-responsive gel such as poly(N-isoproplyacrylamide) (PIPAAm), into a standard tissue culture polystyrene dish.

This material alternates between hydrophobicity and hydrophilicity based on the working temperatures and this further influences the capability of the cells to attach to the material. Indeed, at low temperature (20°C) the surface of the

material becomes hydrophilic and cells cannot attach. However, at 37°C the shell turns hydrophobic and cells can attach and proliferate on the surface. Thus, cells expanded on the surface can be harvested without enzymatic treatment (e.g trypsin) but simply by reducing the temperature.

Interestingly, the interaction between cells remains preserved and several layers of cell sheets can be assembled together in order to build more complex 3D structures. Notably, hepatic cell sheets have been produced by employing both parenchymal and non-parenchymal cells and this system enhanced hepatic functions such as albumin and urea synthesis compared with 2D monolayer cultures[87,93].

Nevertheless due to absence of vascularisation and therefore of oxygen supply, the cell sheet system can only be used for a short period of time because of the consequent ischemic process.

1.7.3. Scaffolds/matrix-based 3D cultures

One of the most exploited systems for the development of 3D in vitro culture platform consists in reseeding cells into 3D scaffolds. These scaffolds can be derived from both synthetic and biological sources.

Synthetic scaffolds can be easily manufactured but lack key features such as physiological bioactivity and biomechanics. The most common artificial matrices employed for engineering biological tissues are synthetic polymers (e.g. polylactide-co-glycolide (PLG), Polyethylene glycol (PEG)) and polycaprolactone (PLA)[94,95] and natural-derived hydrogels (e.g., alginates, celluloses, polyethylene)[96], respectively.

In addition, 3D scaffolds can be developed by using biological materials ECM-construct derived. For instance, several substrates have been developed employing basement membrane gels or type I collagen gels. These materials are characterized by preservation of ECM molecules that improve cell attachment and differentiation. However, several limitations characterize these biological gels.

Firstly, it is difficult to come across batches of gel characterized by homogenous mechanical properties[97,98]. Secondly, these gels do not resemble natural 3D tissue-microarchitecture and therefore cells encapsulated in the gel randomly self-organise in a non-physiological 3D structure. Lastly, these materials are often non-tissue specific thus affecting the reproduction and maintenance of organ specific metabolic function in case of liver tissue engineering[99].

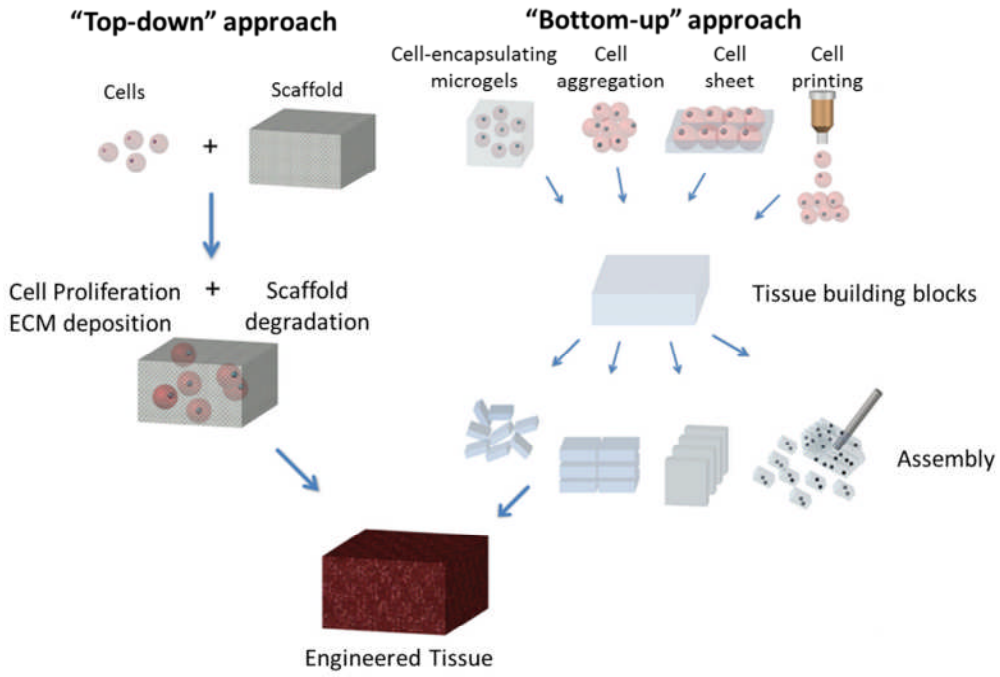

Figure 1.2. Tissue Engineering & Regenerative Medicine combines expertise on the fields of cell biology, material science and tissue engineering aiming to ultimately repair and reproduce defective or missing organs in the body.

1.8. Decellularised 3D scaffolds

As mentioned, the development of biomaterials for functional tissue engineering requires the mimicking tissue-specific ECM and this is possible by employing acellular tissues derived from the decellularisation of tissues and organs. This process involves the complete removal of cellular material from the tissue while maintaining ECM protein composition, topography and mechanical properties of the native tissue [100].

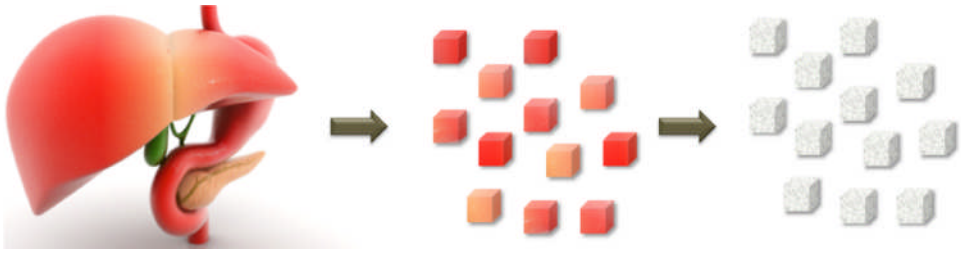

Figure 1.3 Schematic view of the process for obtaining human liver cubes from whole human liver

However, decellularisation protocols needs to be tissue-specific due to the high variability of protein compositions between different types of tissue. This section will review reagents and techniques employed for tissue and organ decellularisation, while highlighting those with more relevance for healthy and diseased liver tissue.

1.8.1 Temperature

The freeze-thaw process effectively causes cell lysis within tissues and organs, but the resulting membranous and intracellular contents remain associated with the 3D scaffold unless removed by successive processing steps.

The protocol is usually characterized by freezing the tissue at – 80°C and then thawing the tissue at 4-37 °C. This method has been demonstrated to be effective for lysing cells in several tissues, including adipose tissue[101], lung[102], tendons[103,104], ligaments[105] and nerve[106]. However, the ECM ultrastructure may be severely damaged by the ice-crystals formed during the freeze-thaw process[107,108].

1.8.2 Hypotonic and Hypertonic Solutions

Hypotonic and hypertonic solutions are primarily used to cause an osmotic shock to the cells without affecting ECM structure and composition. To this aim, perfusion with hypotonic and hypertonic solutions is commonly repeated in series to maximize the osmotic effect[109-111]. In addition, these solutions contribute to wash out cell debris after cell lysis.

1.8.3 Chemical Agents

1.8.3.i Acids and Bases

Acids and bases have a direct effect on protein structure because they modify proteins oxidation state. Their mechanisms of actions lead to alteration of protein folding and therefore this could facilitate the removal of cellular materials during the decellularisation procedure.

This has been proved by De Fillipo *et al*. showing that ammonium hydroxide during the decellularisation protocol contributed to the wash out of cellular debris[112]. Several acids including peracetic acid[113], hydrochloric acid[114], acetic acid[115] and sulphuric acid[116] have also been employed in decellularization protocols leading to an improvement of the decellularisation efficiency. However, many of these acids tend to compromise the quality of the biological scaffolds due to the removal of key molecules such as glycosaminoglycans (GAGs) from the ECM structure[97]. On the other hand, bases are not commonly employed as decellularisation additives. Indeed, bases lead to reduction of the mechanical properties of the tissue mainly due to the cleavage of collagen fibrils[117].

1.8.3ii Non-ionic and Ionic Detergent

The mechanism of action of non-ionic detergents is mediated by the cleavage of lipid-lipid and lipid-protein interactions without interfering with interactions between proteins[118]. The most common non-ionic detergent employed in work so far published is Triton X-100; however its effect on cell removal is still unclear. Indeed, Dahl *et al.* demonstrated that Triton X-100 was not effective at eliminating cellular or nuclear debris from vessels[109], whereas Grauss *et al.* found that Triton X-100 was efficient at removing nuclear material from aortic valves, but ineffective at removing cellular debris[119]. In contrast with these observations, Triton X-100 was shown to be able to effectively decellularise mice livers[120]. Therefore, it is likely that these differences are strictly connected with the type of tissue to be processed thus highlighting the importance of selecting the appropriate cocktail of decellularization reagents to achieve full decellularization. Interestingly, Triton X-100 preserves the integrity of collagens but influences the composition of GAGs.

On the other hand, ionic detergents are effective in removing cellular debris as well as ECM proteins by modifying the interactions between proteins. The two most common ionic detergents employed in the decellularization protocols are Sodium dodecyl sulfate (SDS) and Sodium deoxycholate (SDC). In several tissues tested, SDS removes most of the cellular components and disrupts the nuclear membrane while a small percentage of nuclear materials is left in the tissue[110,121-126]. Unfortunately, this treatment appears to alter the integrity of collagens[110,121-126] while its impact on GAGs distribution is less evident than that reported with the Triton X-100 treatment[127]. Interestingly, due to the fact the SDS is not easily washed out from the tissue, this ionic detergent is often followed by Triton X-100 [128].

SDC is a milder ionic detergent compared to SDS and it also removes cellular components and nuclear membranes[110,121-126]. SDC is generally followed by step employing nucleases in order to improve DNA/RNA extraction [129]

1.8.3.iii Other reagents

Other reagents employed for decellularisation includes zwitterions and chelating agents. These reagents are frequently used together with ionic or non-ionic detergents. Zwitterions are characterised by both ionic and non-ionic features. For instance, the 3-[(3-cholamidopropyl)dimethylammonio]-1-propanesulfonate (CHAPS) is a zwitterion employed in decellularisation procedures. CHAPS and zwitterions can affect the composition of ECM proteins as proved by Petersen *et al.* which showed that the amount of elastin and GAGs was significantly reduced after decellularisation with high concentration of CHAPS[130].

EDTA is a chelating reagent which binds to metal ions[131] and thus contributes to cell detachment from the ECM. Its mechanism of action is mediated by the inhibition of calcium and magnesium ions needed for cell attachment[132].

1.8.4 Enzymatic reagents

Different types of enzymes can be employed as part of decellularisation protocols due to their capability of either disrupting interaction between cell and ECM proteins (e.g trypsin) or removing nucleic acids (e.g nucleases).

Trypsin has been commonly used for detaching adherent cells in 2D monolayer culture. Therefore, this enzyme in association with EDTA has been employed in several decellularisation protocols.

However, trypsin has severe effects on the amount of ECM proteins preserved, leading to the reduction in the amount of elastin, fibronectin, laminin and GAGs[133-135]. In contrast with this, nucleases have little or no effect on the ECM and are often combined with chemical agents in order to maximise cell material removal. However, nucleases are not easily removed from the tissue and therefore the processed tissue may elicit immunological responses after transplantation.

Method	Mode of action	Effects on ECM	Ref.
Physical forces			
Snap freezing	Intracellular ice crystals disrupt cell membrane	ECM can be disrupted or fractured during rapid freezing	101-108,136
Direct mechanical agitation	Can cause cell lysis, but more commonly used to facilitate chemical exposure and cellular material removal	Aggressive agitation can disrupt ECM as the cellular material is removed	109,133,137-142
Sonication	Can cause cell lysis by disrupting cel membrane	Aggressive sanitation can disrupt ECM as the cellular material is removed	143-149
Chemical Agents			
Acids and Bases	Solubilises cytoplasmic components of cells, disrupts nucleic acids, tend to denature proteins	May damage collagen, GAG, and growth factors	112-115 116,117,150
Hypotonic and Hypertonic solutions	Cell lysis by osmotic shock, disrupt DNA-protein interactions	Effectively lyses cells, but does not effectively remove cellular residues	109-111,138
Non-Ionic detergents			
Triton X-100	Disrupts lipid–lipid and lipid–protein interactions, while leaving protein–protein interactions intact	Mixed results; efficiency dependent on tissue, removes GAGs	109,118-120
Ionic detergent			
Sodium dodecyl sulphate (SDS)	Solubilises cytoplasmic cells and nuclear cellular membrane tends to denature proteins	Removes nuclear remnants and cytoplasmic proteins; tends to disrupt native tissue structure, remove GAGs and damage collagen	110,121-126

Sodium deoxycholate (SDC)	Very similar mechanism to SDS	Mixed results with efficacy dependent on tissue thickness, some disruption of ultrastructure and removal of GAG	110,121-126,129,131
Zwitterionic detergents			
CHAPS	Exhibit properties of non-ionic and ionic detergents	Efficient cell removal with ECM disruption similar to that of Triton X-100	130
EDTA	Chelating agents that bind divalent metallic ions, thereby disrupting cell adhesion to ECM	No isolated exposure, typically used with enzymatic methods (e.g., trypsin)	131-135
Enzymes			
Nucleases	Catalyze the hydrolysis of ribonucleotide and deoxyribonucleotide chains	Difficult to remove from the tissue, could invoke an immune response	110,130,140,151,152
Trypsin	Difficult to remove from the tissue, could invoke an immune response	Prolonged exposure can disrupt ECM ultrastructure, removes ECM constituents such as collagen, laminin, fibronectin, elastin, and GAG, slower removal of GAG compared to detergents	133-135

Table 1.1. Decellularisation methods: mode of action and effect on the ECM. Adapted from Crapo et al. 2011 and Gilbert et al. 2006 [131,151].

1.8.5 Techniques to apply decellularisation agents

1.8.5.i Immersion and agitation

The decellularisation of small-scale non-perfusable tissue can be achieved by immersion in decellularisation agents while being subjected to agitation. There are two types of mechanical agitation: indirect and direct.

Sonication is a type of indirect mechanical agitation, in which cell damage is caused by sound waves[143,144,148,149]. However, complete tissue decellularisation

cannot be achieved by employing only the sonication step[144,145] but it needs to be followed by treatments with chemical reagents[146,147].

The direct agitation of tissues immersed in decellularisation agents is achieved by employing an orbital shaker. This procedure was pioneered by Meezan and colleagues in 1975[153], who proposed this methodology for studying the basement membrane microstructure. Subsequently, this methodology has been adapted to decellularise sections of different tissues, including xenogenic liver, by incubating the native tissue with different detergents but the mechanical forces employed (expressed as g-force) have never been precisely defined [109,124,133,137,138,140-142].

1.8.5.ii Whole organ perfusion

The development of biological scaffolds with preserved vascular structure is essential for generating 3D structures suitable for tissue engineering directed at organ transplantation. Therefore, decellularisation reagents have been employed for both antegrade and retrograde perfusion through the main vessels in order to effectively reach the cells and washing out cellular materials. This technique has allowed the development of biological scaffolds with preservation of three-dimensional architecture and vasculature preservation.

The heart has been the first whole organ to be successfully decellularised by retrograde coronary perfusion by Ott and colleagues in 2008. Their pioneering protocol enabled the development of rodent heart ECM scaffold characterised by macroscopic translucent colour and preserved vasculature structure. In addition, they reseeded this scaffold with cardiomyocytes that formed areas with contractile capabilities[154].

Afterwards, several protocols have been employed in order to develop human and non-human whole organs such as lung[130], kidney[155] and liver[45,156].

Together, these studies showed the initial strategies to develop whole organ ECM scaffold which supported cell engraftment and maintenance of tissue-specific function.

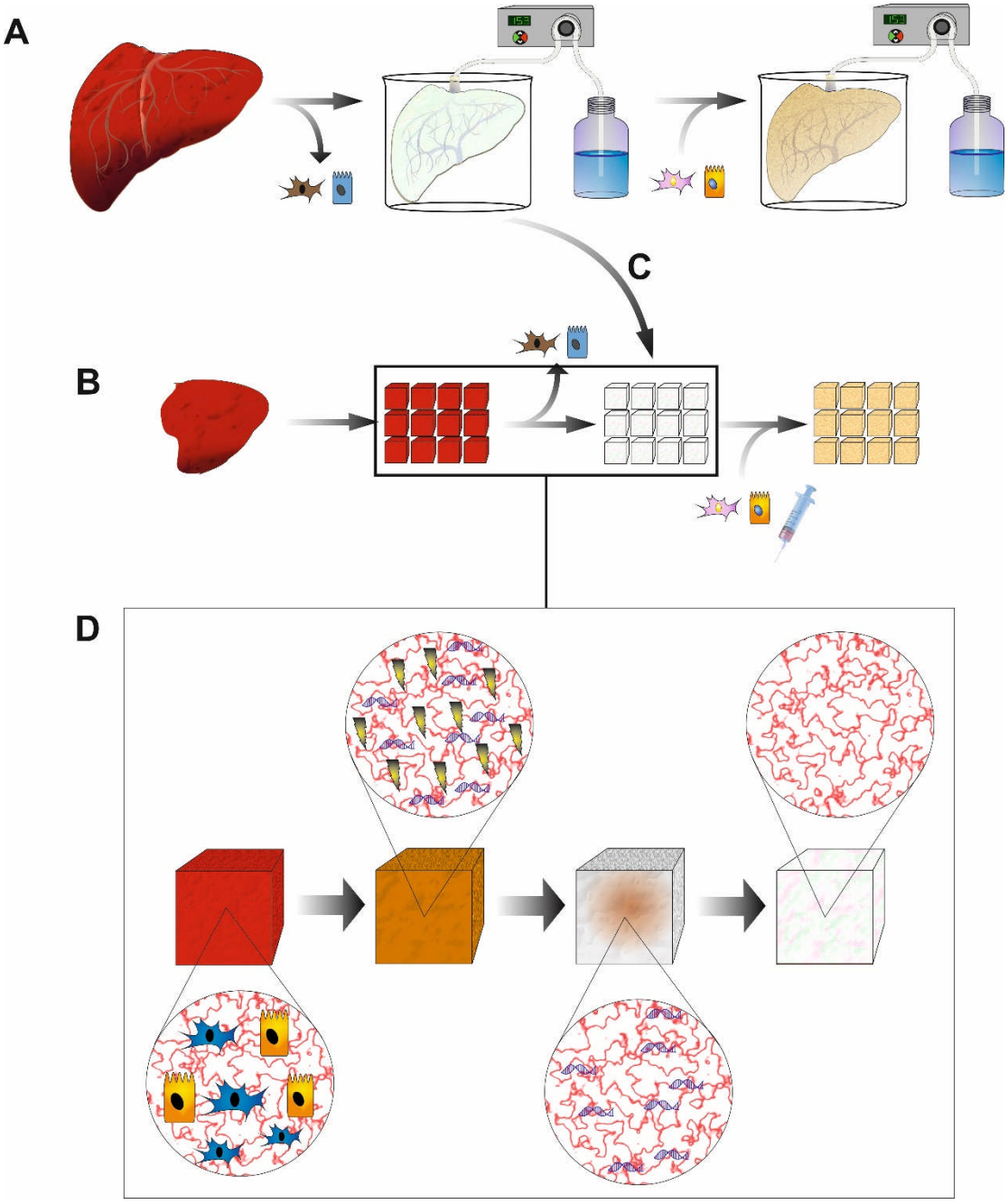

Figure 1.4. This figure shows two approaches for developing liver biological scaffolds: (A) Perfusion-decellularisation, which requires the perfusion of decelularisation reagents through the main hepatic vasculature (e.g vein cava). After the development of whole organ scaffold, these tissues can be dissected into cubes followed by static reseeding (B) or recellularised by whole organ perfusion. (C) Agitation-decellularisation requires the dissection of native livers into cubes followed by immersion in decellularisation reagents and agitation. The decellularisation is a multi-step process allowing the removal of cellular materials, proteins and DNA leading to the development of acellular translucent scaffold (D).

1.9 Aims

As already introduced, the first whole rodent liver scaffold was established in 2011 and only in 2014 a porcine human-size liver scaffold was developed. Although biological scaffolds are characterised by lack of immunogenicity, it is relevant to develop human scaffolds because the 3D microstructure of human liver differs from other mammals and it would be therefore easier to translate into clinical applications in humans. Thus, developing human acellular tissue may have a dramatic impact towards the development of engineered tissue for regenerative medicine and *in vitro* disease modelling. In addition, the development of diseased scaffold may contribute to further understand pathological processes in which ECM proteins play a key role in disease initiation and progression (e.g amyloidosis).

Therefore, the work described in the present thesis has been aimed: (i) to develop an effective protocol for the decellularisation of whole human livers and to characterise the composition, bioactivity and biocompatibility of the resultant hepatic ECM scaffold, (ii) to decellularise both healthy and amyloidotic mice livers in which the key physiological and pathological features are preserved and to assess the feasibility of perfusing the 3D mouse biological scaffold with human amyloidogenic proteins. Lastly (iii), to develop a rapid and robust protocol in order to produce acellular human liver cubes starting from non-perfusable tissue and to characterise the ECM protein composition, architecture, topography and bioactivity of the resultant scaffold.

Chapter 2: Decellularised human liver as a natural 3D-scaffold for liver bioengineering and transplantation

2.1 Introduction

This chapter describes the development and characterisation of healthy whole human liver acellular scaffolds. Some of the data reported in this chapter have been incorporated into a patent (UK patent application n°1409858.6 filed with UCL Business) and have been recently published: **Mazza, G.** et al. Decellularized human liver as a natural 3D-scaffold for liver bioengineering and transplantation[156].

The area of liver tissue engineering and regenerative medicine has been intensively explored during the last decade due to the severe shortage of organs associated with a worldwide increase of deaths due to acute and chronic liver diseases. Indeed, according to the World Health Organisation, the total deaths caused by cirrhosis and liver cancer have increased by 50 million/year since 1990[157]. In the UK, the number of deaths from cirrhosis in those <65 years have increased six times in the last three decades[158].

Liver transplantation is the only effective treatment for patients with end stage liver disease but unfortunately is limited by both high cost and severe shortage of organs[159]. Therefore, several strategies have been developed in order to expand the availability of livers for transplantation such us split liver transplants, living-related partial donor procedures[160] and the increasing use of “marginal” organs such as older donors, steatotic livers, non-heart-beating donors, donors with viral hepatitis, and donors with non-metastatic malignancy[161]. Despite these surgical advancements, it is unlikely that the availability of good liver grafts will ever be sufficient to meet the increasing demand of patients with end stage liver disease.

Therefore, more innovative approaches have been investigated including liver support systems, such as bioartificial livers and hepatocyte transplantation. However, their use in the clinical setting is still at an experimental level and the relative efficacy has still to be proved[162-167].

Thus, there is urgent need of developing novel strategies in order to face the organ-shortage crisis. The most promising approach includes the *de-novo* development of functional hepatic tissue that may be used for transplantation. Engineering a functional hepatic tissue requires the combination of both cells (e.g stem cells or differentiated cells) and 3D-scaffolds. Although, several advancements have been achieved with regards to cell isolation, expansion and manipulation, the main limitation in this field is the development of scaffolds that mimic the complexity of the human ECM network. Indeed, a number of techniques have been employed to develop 3D scaffolds such as electrospinning[168], 3D bio-printing[169] and decellularisation[170]. To date, decellularised tissues and organs are the only scaffolds that resemble ECM composition, architecture, topography and biomechanical properties of biological tissue and therefore seem to be the most suited for liver tissue engineering.

The decellularisation of whole organs was firstly introduced by Ott *et al.* in 2008 with the aim to develop acellular heart from mice. This pioneering work entailed the removal of cellular material while preserving the vascular network, ECM composition and 3D architecture of native tissue. The preservation of those physiological features allowed the functional engraftment of cardiomyocytes with restoration of contractility. The perfusion protocol employed by Ott and colleagues was characterised by retrograde coronary perfusion at constant pressure. Afterwards, Uygun et al. adapted this protocol in order to develop the first whole organ rodent liver scaffold. In this case, investigators used an antegrade perfusion through the portal vein, at constant flow rate, and were able to obtain a translucent acellular tissue within few days. Subsequently, several protocols have been developed in order to obtain non-human liver scaffolds[120,171-173]. The resulting 3D ECM scaffolds have been shown to provide an excellent environment for the *in vitro* growth of multiple liver cell types retaining excellent functionality[174,175]. Notably, in 2010, the repopulation of an acellular rat liver scaffold with 50 million mature rat hepatocytes was achieved by cell perfusion via the portal vein. Importantly, hepatocytes migrated beyond the matrix barrier to reach the decellularised sinusoidal spaces[45]. In 2012, a further step onward was

made with the repopulation of a pig liver scaffold with human foetal hepatocytes and stem cells[176].

The main advancement achieved in the development of liver biological scaffolds has been to scale up the decellularisation protocol for obtaining large animal acellular livers. This is a key condition in order to develop sufficient hepatic mass for restoring liver function upon transplantation in large animals including humans. To achieve this result, several factors were modified including time of organ perfusion with decellularisation reagents and most importantly flow rate and pressure.

However, the decellularisation and repopulation of a human liver ECM scaffold with human derived liver cells has not been so far reported by other researchers.

Notably, the human hepatic ECM displays remarkable differences in terms of protein composition and architecture when compared with non-human livers (e.g porcine) and therefore the ideal condition of human hepatic engineering will be to engraft human cells within human hepatic scaffolds.

Therefore, the next section of this chapter will describe the development and characterisation of whole human liver acellular scaffolds as well as the relative *in vitro* and *in vivo* biocompatibility (Figure 2.1).

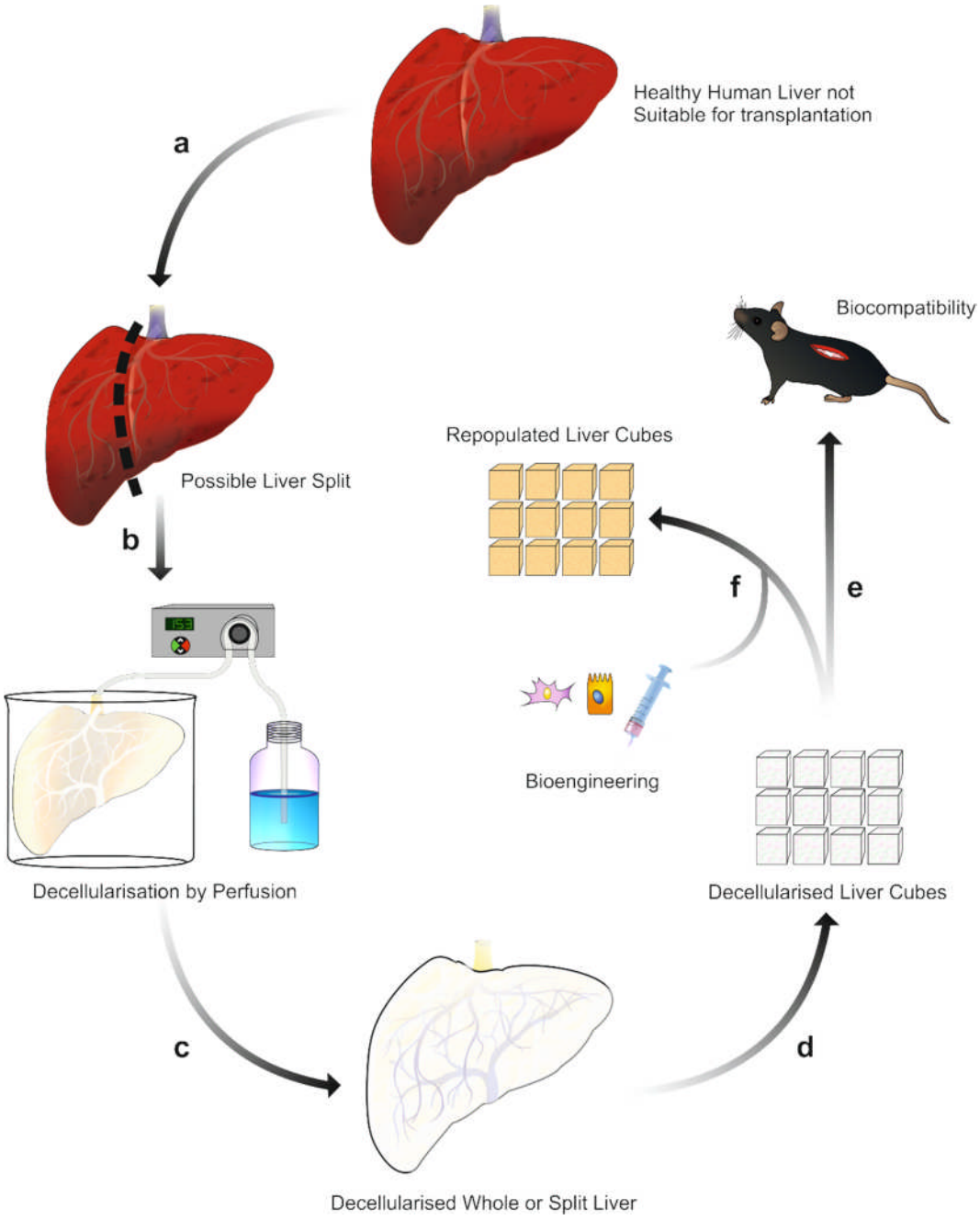

Figure 2.1. Schematic study plan. Human liver unsuitable for transplantation is surgically processed in order to obtain an isolated left lobe or is used as a whole (a-b). Lobes, or whole organs, are cannulated and decellularised by retrograde perfusion (c). Once decellularisation is complete, human liver scaffolds are dissected by scalpel cleavage to obtain liver cubes (d) as a 3D-platform for biocompatibility and bioengineering studies (e,f).

2.2 Methods

2.2.1 Source of human livers

The work described in this thesis was performed on healthy human livers that were harvested for transplantation and then judged unsuitable due to prolonged graft cold ischaemic time, the presence of extra-hepatic malignancy or other important extra-hepatic co-morbidities in donors or recipients. Livers included in this chapter were defined “healthy” because of the absence of any degree of tissue fibrosis and fat accumulation by histological analysis. The study was approved by the UCL Royal Free Biobank Ethical Review Committee (NRES Rec Reference: 11/WA/0077). Informed consent for research was confirmed via the NHSBT ODT organ retrieval pathway, and the project was also approved by the NHSBT Research Governance Committee. Donor livers were processed in accordance with the UCL Royal Free Biobank protocols under the Research Tissue Bank Human Tissue Act licence, prior to use in research. Human livers obtained at the Royal Free London Foundation Trust were coordinated, received and recorded by the UCL Tissue Access for Patient Benefit organisation (TAPb) which links research activities between UCL Royal Free Biobank, the Royal Free Trust and UCL. TAPb has full governance in place for this purpose which has involved NHSBT ODT pathway, the Human Tissue Authority licencing, and the local Trust / UCL Research offices.

2.2.2 Preparation of human livers for the decellularisation procedure

Upon retrieval human livers were maintained in ice. Human livers (n=7) were either surgically processed in order to obtain the liver left lobes (n=6) including segments 1,2,3 and 4 or retained as a whole liver (n=1) with preserved vascular access.

In the case of whole liver preparation, the donor liver was processed exactly as for liver transplantation. Thereafter the upper caval cuff, reaching the atrial rim, was over sewn with a running double row of 3-0 prolene suture. The water tightness of the organ was proofed both by antegrade portal and retrograde hepatic venous perfusion under relative high pressure as produced by a 50 ml bladder syringe with PBS solution.

For segmental liver preparation of left lateral liver (S1+S2+S3+S4), dissection was started at the hilar region with inspection, preparation, division and ligation of the hepatic artery (HA), of the portal vein (PV) and of the bile duct (BD). Segment 4 HA is preserved if originating from the right hepatic artery, forcing the division of the right HA distal to its bifurcation. The right hepatic vein is divided and the middle and left hepatic veins are preserved within the left lobe to be used for further decellularisation. The line of parenchymal division is maintained to the left of the line of Cantlie in order to maintain the left portion of S4. The parenchyma is divided sharply with a knife for (of?) the liver capsule and subsequently with crush-clamp technique, performing meticulous hemo- and bilio-stasis. The parenchymal division is carried to the end, producing a left lateral liver extended to S4 and a right liver as non-functional unit. Finally, the upper caval cuff, reaching the atrial rim is over sewn with a double run of 3-0 prolene suture.

Human livers were then frozen at -80°C for at least 24h. Indeed, tissue freezing represents the initial step leading to the destruction of the various cellular compartments which is key for the process of decellularisation.

2.2.3 Optimization of the various decellularisation protocols of whole human liver

The initial protocol tested was aimed at comparing the efficiency of previously published protocols for animal liver when employed to decellularise human livers. This protocol was characterized by the cannulation of the hepatic portal vein and livers (n=2) were then perfused at constant flow rate (100 ml/min) as previously described for porcine liver[47]. The protocol schedule was characterized by alternating deionized water and Sodium Deoxycholate (SDC) up to 6 weeks. Afterwards, an alternative protocol was adopted in which both hepatic portal vein and hepatic artery were cannulated. Livers (n=2) were perfused with the same solutions as described above up to 6 weeks by employing different flow rates for the vein and the artery (100ml/min and 25ml/min, respectively).

Lastly, a third protocol was investigated in which retrograde perfusion (n=3) was adopted followed by two phases of flow rate: a) a steeply increasing flow rate to

compensate reduced resistance and b) the stabilization of the flow rate as the decellularisation proceeds (Figure 2.2).

In order to estimate the starting flow rate, the following formula was adopted: 0.2-0.3 ml/min/g of liver. The increasing flow rate over the time is described in Figure 2.2.

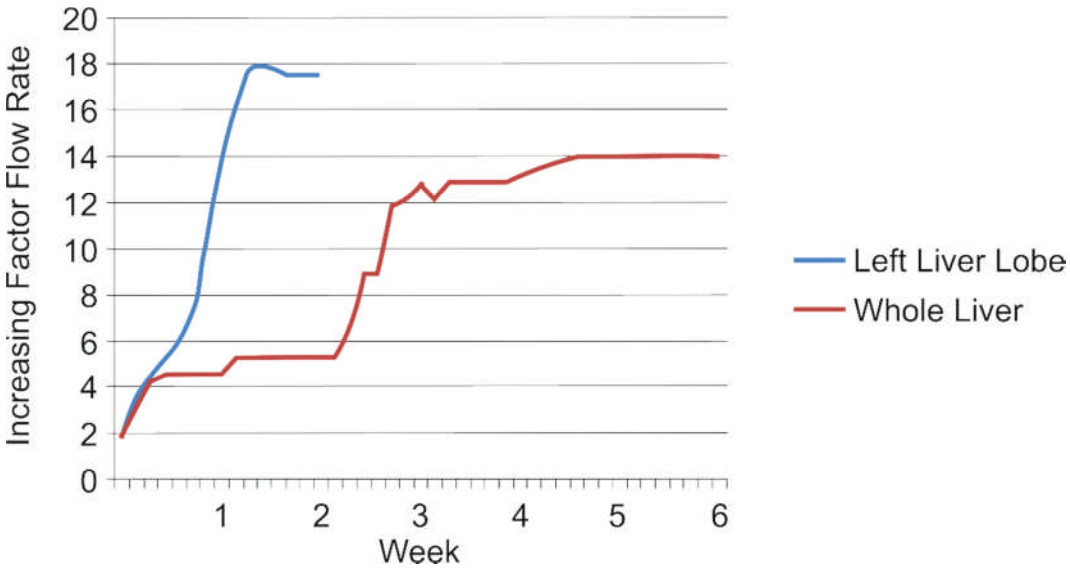

Figure 2.2. Flow rate. The graph shows the increasing flow rate over time. The decellularisation of a human liver left lobe (blue line) was achieved in 2 weeks, while the decellularisation of a whole human liver (red line) was completed in 6 weeks.

An example of perfusion regime adopted for the decellularisation of a liver left lobe is shown in Table 2.1. The decellularisation of the whole liver was performed by repeating the procedure as shown in Table 2.1 three times (the freezing/thawing step was performed just once).

DAY -1
Thawing the liver in PBS 1x at 4ºC overnight (o.n.)
DAY 0
Left vein cava cannulation
Cleaning tubes with:
4% EtOH (15-30 min)
PBS (15 min)
Starting retrograde liver perfusion:
100 ml/min Recycle MILLIQ 2,5l (30 min)
Change solution after 10 min
Change solution after 20 min
150 ml/min Recycle MILLIQ 2,5l (90 min)

Change solution after 30 min
Change solution after 60 min
200 ml/min 0.025% TRYPSIN/EDTA (1h)
250 ml/min 0.025% TRYPSIN/EDTA (2h)
WASH : 250 ml/min MILLIQ
Change solution after 15 min
Change solution after 15 min
Change solution after 15 min
250 ml/min 0.025% TRYPSIN/EDTA
DAY 1
WASH: 300 ml/min MILLIQ
Change solution after 5 min
Change solution after 10 min
Change solution after 15 min
Change solution after 30 min
350 ml/min 0.01% SDS (2h)
Change solution after 1h
WASH: 350 ml/min MILLIQ (15 min)
350 ml/min 0.1% SDS (4h)
After 2h WASH: 350 ml/min MILLIQ (5 min)
Change fresh 0.1% SDS for other 2 h
WASH: 375 ml/min MILLIQ (30 min)
Change solution after 5 min
Change solution after 10 min
Change solution after 10 min
Change solution after 5 min
400 ml/min 1% SDS
After 1.5h wash: 400 ml/min MILLIQ 5 min
Change fresh 1% SDS 400 ml/mi (14h o.n)
DAY 2
WASH: 425 ml/min MILLIQ (1h)
Change solution after 15 min
Change solution after 15 min
Change solution after 30 min
425 ml/min 0.025% TRYPSIN/EDTA (5h)
WASH: 450 ml/min MILLIQ (15 min)
450ml/min 1% SDS (16h o.n)
DAY 3
WASH: 475 ml/min MILLIQ (1h)
Change solution after 30 min
500 ml/min 3% TRITON X 100
After 5.5 h WASH: 500 ml/min MILLIQ (15 min)
Change fresh 3% TRITON X 100 525 ml/min (18h o.n.)
DAY 4

WASH: 550 ml/min MILLIQ (30 min)
Change solution after 15 min
Change solution after 15 min and Increase at 575 ml/min
600 ml/min 3% TRITON X 100
After 6h increase at 650 ml/min (17.5h o.n.)
DAY 5
WASH: 675 ml/min MILLIQ (30 min)
700 ml/min 3% TRITON X 100
After 1.5h increase at 750 ml/min
After 4.5h increase at 800 ml/min (13.5h o.n.)
DAY 6
Increase at 850 ml/min
After 3h increase at 1l/min
after 4 h WASH: MILLIQ 1.2l/min (1h)
Fresh 3% TRITON X 100 1.2l/min (18h)
DAY 7
WASH: 1.3l/min MILLIQ (2h)
1.3l/min 0.02% TRYPSIN/EDTA (7h)
After 4h increase at 1.35 l/min
WASH: 1.4l/min MILLIQ (18h o.n.)
DAY 8
Fresh MILLIQ 1.5l/min (3.5h)
After 1.5h increase at 1.55l/min
1.7l/min 1% SDS (16.5h o.n.)
DAY 9
WASH: 1.75l/min MILLIQ (3h.)
Change solution after 1h & increase at 1.755
Change solution after 1h
1.85l/min 1% SDS (4h)
After 2.5h increase at 1.9l/min
WASH: 1.7l/min MILLIQ (1.5h)
1.75l/min 1% SDS (15.5h o.n. *355 ml/min pump*)
DAY 10
WASH: 1.75l/min MILLIQ (1.5h)
1.8l/min 1% SDS (5h)
WASH: 1.8l/min MILLIQ (1.5h)
1.8l/min 1% SDS (15h o.n.)
DAY 11
WASH: 1.8l/min MILLIQ (1h)
Change solution after 5 min
Change solution after 15 min

Change solution after 30 min
1.75l/min 1% SDS (6.5h)
WASH: 1.75l/min MILLIQ (30 min)
Change solution after 5 min
Change solution after 5 min
Change solution after 5 min
Change solution after 15 min
1.75l/min 1% SDS (15h,45min o.n.)
DAY 12
WASH: 1.75l/min MILLIQ (75 min)
Change solution after 5 min
Change solution after 10 min
Change solution after 60 min
1.75l/min 1% SDS (5h)
WASH: 1.75l/min MILLIQ (1h)
Change solution after 10 min
Change solution after 50 min
1.75l/min 1% SDS (17h o.n.)
DAY 13
WASH: 1.75l/min MILLIQ (30 min.)
Change solution after 5 min
Change solution after 10 min
Change solution after 15 min
1.75l/min PBS/AA 5% (1h)
1.75l/min TX100 3% (22h,15min o. n.)
Change solution after 1h
Change solution after 6h
DAY 14
WASH: 1.75l/min MILLIQ (1.5h)
Change solution after 5 min
Change solution after 10 min
Change solution after 30 min
Change solution after 30 min
Change solution after 15 min
1.75l/min PBS (1h)
1.75l/min PBS/AA 5% (2h)
WASH: 1.75l/min MILLIQ (1.15h)
Whole organ sterilization:
1.75l/min 0.1%PAA + 4% ETOH (1h)
1.75l/min PBS (1h)

Table 2.1. Perfusion protocol. The table shows the different step employed for the decellularisation of human liver left lobe. The decellularisation of the whole human liver was achieved by repeating three times the procedure whown in the table.

After decellularisation, the acellular tissue was dissected in order to assess the homogeneity of the procedure by removing all the segments as well as all vessels and pedicles. In addition, 125mm^3 scaffold fragments (5mmx5mmx5mm) were dissected by scalpel cleavage for liver bioengineering *in vitro* and *in vivo* transplantation in mice.

2.2.4 Histology and immunostaining analysis

Samples were fixed for at least 24 hours in 10% neutral buffered formalin solution (pH 7.4) at RT. Tissue was embedded in paraffin and sectioned at 4 μm. Prior to staining, sections were dewaxed in xylene and rehydrated using graded industrial denatured alcohol (IDA).

Histochemical stainings: tissue sections were stained with Harris's Haematoxylin and Eosin (H&E) (Leica, Germany), Picro-Sirius Red (SR) (Hopkin & Williams) (BDH Chemicals Ltd, Cellpath Ltd) and Miller's Elastic staining with a Picro-Sirius red counter stain (VWR, Leica, Raymond A Lamb).

Immunocytochemistry: sections stained with Collagen I, III, IV, fibronectin and laminin were incubated in 0.5% Trypsin (MP Biomedical) / 0.5% Chymotrypsin (Sigma) / 1% Calcium Chloride (BDH) in Tris buffered saline pH 7.6 (TBS) for 30 minutes at 37 °C. Sections stained with alpha-smooth muscle actin (α-SMA) were microwaved (640W) for 20 minutes in 1L of Tris-EDTA buffer (10mM Tris-base/1mM EDTA solution, pH9.0) and sections for CD3 were pressure cooked for 3 minutes in sodium citrate buffer (10mM Sodium Citrate, pH 6.0). Slides were then soaked in TBS with 0.04% Tween-20 (Sigma) for 5 minutes, blocked in peroxidase blocking solution (Novocastra) for 5 minutes, washed in TBS for 5 minutes and then incubated for 1 hour in the following primary antibodies; collagen I (Rabbit pAb to coll1 (ab34710), diluted 1:200; Abcam), collagen III (Rabbit pAB to coll3 (ab7778), diluted 1:500; Abcam), collagen IV (mouse mAb to coll4 (M0785), diluted 1:25; Dako), fibronectin (mouse mAb to fibronectin (MAB1937), diluted 1:100; Millipore), laminin (mouse mAb to laminin α5-chain (MAB1924), diluted 1:200; Millipore), alpha-Smooth Muscle Actin (mouse mAb to SMA, (M0851/1A4), diluted 1:500; Dako) and CD3 (rabbit pAb to CD3, (AO452), diluted 1:200; Dako). The slides were then placed for 25 minutes in NovolinkTM post primary (Novocastra), 25 minutes in NovolinkTM polymer

solution (Novocastra) and developed with NovolinkTM 3,3' di-amino-benzidine (Novocastra) with a 5 minute wash in TBS with 0.04% Tween-20 between each step. Slides were counterstained with Mayer's Haematoxylin (Sigma) for 3 minutes. All sections were dehydrated in graded IDA, cleared in xylene and were mounted with DPX (Leica biosystems); cover slipped and observed using a Zeiss Axioskop 40. Images were captured with an Axiocam IcC5 using Zeiss Axiovision (verison 4.8.2). All images were analysed and enhanced using Fiji v1.49d (ImageJ Jenkins server).

2.2.5 DNA quantification

To assess total DNA content within native tissue and acellular matrices, the DNeasy Blood and Tissue kit was used according to the manufacturer's manual (Qiagen). Briefly, specimens were digested with Proteinase K overnight. DNA samples were purified using buffers provided by the company and measured spectrophotometrically (Nanodrop, Thermo Scientific, US). Optical densities at 260 nm and 280 nm were used to estimate the purity and yield of nucleic acids.

2.2.6 Collagen quantification

The collagen content of native tissue and decellularised tissue was quantified using the total collagen assay kit according to the manufacturer's manual (QuickZyme Biosciences, The Netherlands). Briefly, samples were hydrolysed in 6M HCl at 95°C for 20 hours, the hydrolysates were mixed with a chromogen solution staining the hydroxyproline residues and color was developed at 60°C for 1 hour. The absorbance for each sample was determined at 555 nm using a FLUOstar Omega microplate reader (BMG labtech, Germany) and the collagen quantity was calculated by usage of a standard curve of pure collagen hydrolysates.

2.2.7 Elastin quantification

The elastin content of native and decellularised tissue was quantified using the FASTIN elastin assay (Biocolor, UK) according to the manufacturer's

instructions. Briefly, the samples were homogenized, and elastin was solubilised in 0.25 M oxalic acid. Two consecutive incubations were performed at 95°C to ensure complete extraction of elastin. Extracts were incubated with 5,10,15,20-tetraphenyl-21H,23H-porphine tetrasulfonate (TPPS) dye, and absorbance was determined at 513 nm spectrophotometrically FLUOstar Omega microplate reader (BMG labtech, Germany). Elastin concentrations from a standard curve were used to calculate the elastin content of the tissue.

2.2.8 Scanning Electron Microscopy (SEM)

Samples were fixed in 2.5% glutaraldehyde in 0.1 M phosphate buffer and left for 24 hours at 4°C. Following washing with 0.1 M phosphate buffer, samples were cut into segments of approximately 1 cm length and cryoprotected in 25% sucrose, 10% glycerol in 0.05 M PBS (pH 7.4) for 2 hours, then fast frozen in Nitrogen slush and fractured at approximately -160°C. Next, samples were placed back into the cryoprotectant at room temperature and allowed to thaw. After washing in 0.1 M phosphate buffer (pH 7.4), the material was fixed in 1% OsO4 / 0.1 M phosphate buffer (pH 7.3) at 3°C for 1½ hours and washed again in 0.1 M phosphate buffer (pH 7.4). After rinsing with dH_2O, specimens were dehydrated in a graded ethanol-water series to 100% ethanol, critical point dried using CO_2 and finally mounted on aluminum stubs using sticky carbon taps. The fractured material was mounted to present fractured surfaces across the parenchyma to the beam and coated with a thin layer of Au/Pd (approximately 2nm thick) using a Gatan ion beam coater. Images were recorded with a 7401 FEG scanning electron microscope (Jeol, USA)

2.2.9 Xenotransplantation in immunocompetent mice

All animal experiments were approved by the Home Office under the UK Animals and Scientific Procedures Act 1986 and in accordance with the guidelines of the Comparative Biology Unit, Biological Services University College London (UCL) under Project license 70/7100.

For biocompatibility studies, twelve male C57BL/6J mice, aged 3-4 weeks, were used. Human liver acellular scaffolds were surgically implanted either

subcutaneously (n=6) or into the omentum (n=6). Briefly, following shaving the operating area, the skin was cleaned with 10% povidone iodine (Videne, Ecolab, Leeds, UK) and 20% chlorhexidine gluconate (Hydrex pink, Ecolab, Leeds, UK). Isoflurane (2% with 98% oxygen) was used to induce anaesthesia. For subcutaneous implantation, a small incision (5mm) was made between the shoulder blades and a subcutaneous tunnel was made by blunt dissection. The human liver scaffold was inserted into the subcutaneous tunnel and the wound was closed with absorbable 4-0 vicryl sutures. When applying an omental implantation, a small midline abdominal incision was made and the human liver cubic scaffold was folded within the omentum and secured in place by 6-0 vicryl sutures. The abdomen was closed in two layers. After 7 and 21 days, mice were euthanized and the implants along with the surrounding tissues were harvested and fixed in 10% formalin for histological and immunohistochemical evaluation.

2.2.10 Cell Culture

The LX2 cell line is a well-established human hepatic stellate cell line that was generated by a spontaneous immortalization in low serum conditions (kindly provided by Professor Scott Friedman)[30]. Cells are cultured in Iscove's Modified DMEM supplemented with 2 mM/L glutamine, 0.1 mM/L non-essential amino acids, 1.0 mM/L sodium pyruvate and 20% Foetal Bovine Serum (FBS). HepG2 and Sk-Hep-1 cells (ATCC® HTB-52™) are derived from a human hepatoblastoma and a human hepatocellular carcinoma, respectively. Both cell types were purchased from ATCC (VA, USA) and cultured in Eagle's Minimum Essential medium (EMEM), supplemented with Glutamax, 0.1 mM/L non-essential amino acids, 1.0 mM/L sodium pyruvate and 10% FBS. All cells were cultured under standard conditions in a humidified incubator under 5% CO_2 and at 37°C. Every 3 days the complete culture medium was changed and sub-confluent cells were trypsinized and passaged at a split ratio 1:3. For cell passaging, culture medium was aspirated and cells were washed twice with Hank´s Balanced Salt Solution (HBSS) and detached using 0.25% trypsin. The enzymatic activity was stopped by adding complete culture media to the cells. Next, the cell suspension was centrifuged at 1500 rpm for 5 minutes before calculating the cell

concentration by using a disposable hemocytometer (C-Chip® DHC-N01, Digital Bio™).

2.2.11 Sterilization of decellularised tissue.

As mentioned above, the whole liver was sterilized by perfusion with both PBS-AA and PAA-EtOH (Table 2.1). The dissected cubes were further sterilized before *in vitro* cell seeding by employing two different methodologies. All the liver cubes were processed in sterile environment before proceeding with the steps described below.

Firstly, the acellular liver tissue was immersed in PBS-AA and agitated for 45 minutes followed by a washing step in sterile PBS up to 15 minutes. Secondly, the decellularised tissue was immersed in PAA-EtOH and agitated for 45 minutes followed by a washing step in sterile PBS up to 15 minutes.

2.2.12 Repopulation and culture of engineered human liver

Sterilized human liver cubic scaffolds were kept overnight in complete medium [day -1]. To start repopulation (day 0) cell cultures were trypsinized and cells were re-suspended in a final concentration of 2 million cells per 50 µl ($2x10^6$/50µL) per scaffold (n≥12 per cell line). Cells were drawn up in a 0.5 ml insulin syringe and released drop by drop to finally cover the decellularised tissue. The tissue was turned upside down during the reseeding procedure by employing sterile tweezers. Seeded scaffolds were kept for 2 hours in a humidified environment at 37 °C with 5% CO_2 allowing cell attachment followed by addition of complete culture medium [day 0]. The culture medium was changed at day 1 and afterwards every 3 days. At days 7, 14 and 21 following seeding, the scaffolds were placed in 10% formaldehyde and assessed by histology and immunohistochemistry or fixed in 2.5% glutaraldehyde for SEM analysis.

2.2.13 Statistical analysis.

Results were expressed as mean±s.d. All data were analysed with ANOVA or Student's t-test. Two-tailed p values less than 0.05 were considered statistically significant.

2.3 Results

2.3.1 Decellularisation of human segmental lobes and whole liver

The initial two protocols employed were derived from Barakat et al and were related to the decellularization of large scale liver[47]. The antegrade protocols were ineffective in generating acellular translucent tissues. Indeed, after six weeks perfusion the livers appeared macroscopically brownish meaning that these protocols were unable to remove efficiently cellular materials (figure 2.3, 2.4). Of note, the liver appeared yellowish between segments 2-3 after the perfusion period (figure 2.3 right panel) thus indicating that the perfusion flow and the decellularisation reagents were not homogenously distributed within the tissue by employing portal vein perfusion.

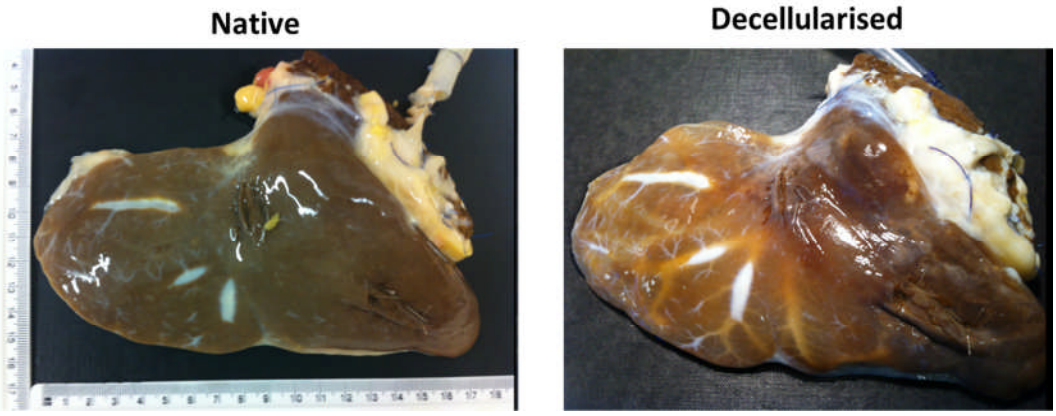

Figure 2.3. Macroscopic appearance of human liver left lobe after 6 weeks portal vein perfusion.

Thus, two routes of perfusion were adopted by cannulating both PV and HA. Despite the inefficiency of this protocol to decellularise the liver left lobe at the macroscopic level, the perfusion of the tissue seemed improved compared with the previously described protocol because of the absence of patchy-area (figure 2.4 right panel). Moreover, the liver appeared softer by employing both protocols thus suggesting a lack of pressure within the whole organ.

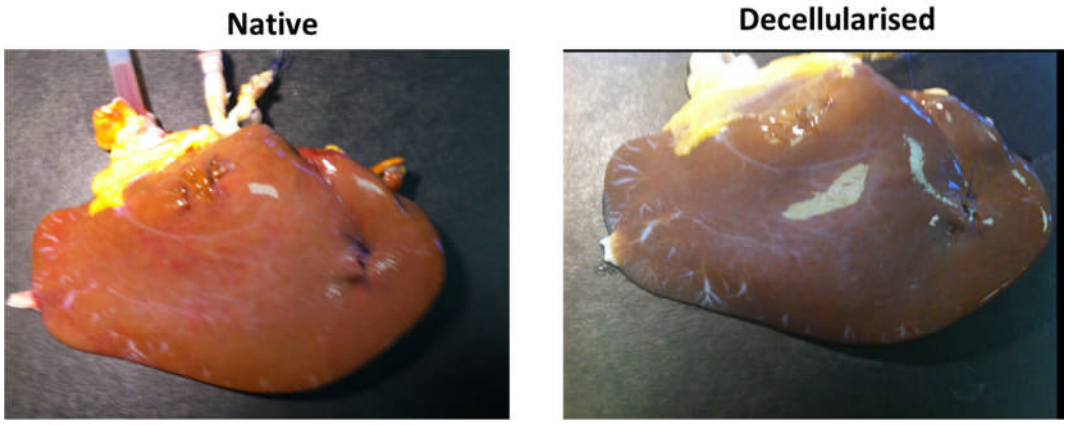

Figure 2.4. Macroscopic appearance of human liver left lobe after 6 weeks portal vein and hepatic artery perfusion.

Therefore, because of these two limitations observed: i) lack of pressure and ii) lack of homogenous perfusion, a novel protocol was adopted involving retrograde perfusion through the hepatic venous system followed by two steps perfusion rate. In addition, the new decellularisation protocol included the usage of proteases such us trypsine and both ionic and non-ionic detergents in order to maximize the decellularisation efficiency.

After 2 weeks perfusion, the liver left lobes appeared macroscopically decellularised (figure 2.5). In addition, an extended version of this protocol was efficient in decellularising a whole human liver after 6 weeks perfusion (Figure 2.6).

Notably, during and following the decellularisation of the whole liver or left liver lobes the tissue became gradually translucent indicating the dissolution of cells (Figure 2.5, 2.6) with the vascular network being visualized at the macroscopic level (figure 2.5 left panel).

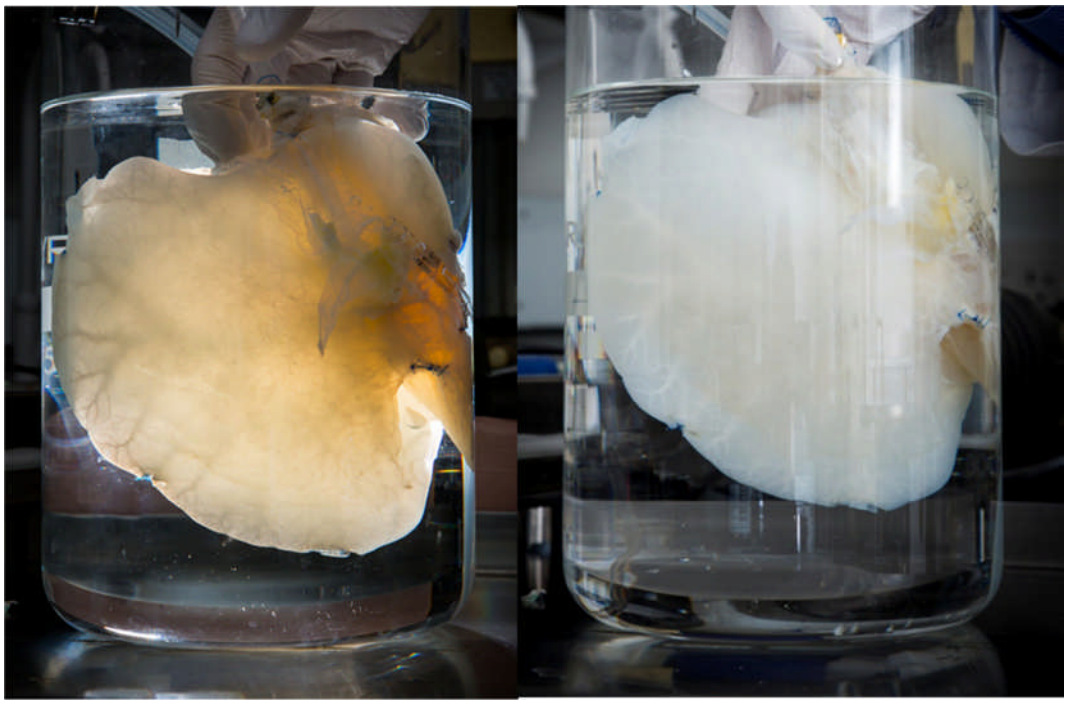

Figure 2.5. Macroscopic appearance of a decellularised left lobe showing preservation of the vascular tree (left panel) and translucent colour (right panel).

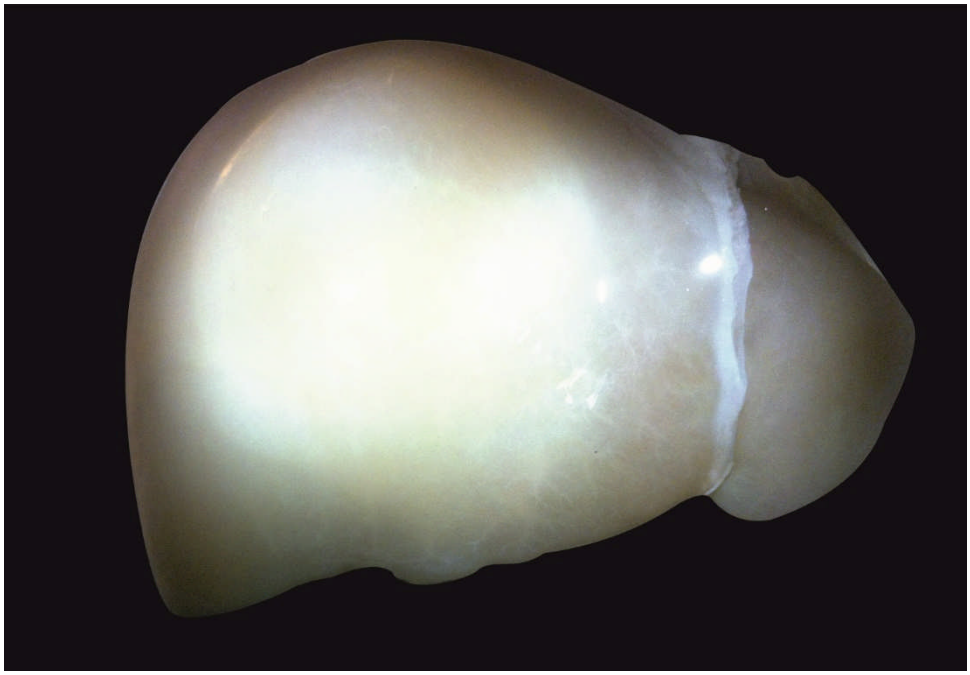

Figure 2.6. Macroscopic appearance of a decellularised whole human liver.

2.3.2 Histological characterisation and quantitative assessment of the human decellularised liver

After decellularisation, the one section derived from each decellularisation procedure was dissected by scalpel cleavage and was analysed by histological

staining to further investigate the homogeneity of the decellularisation procedure. Notably, Haematoxylin and Eosin (H&E) staining showed nuclei removal in all four sections (figure 2.7). In addition, the general liver tissue architecture was preserved as shown by Sirius red (SR) staining for collagen filaments and Van Gieson (EVG) staining for Elastin (figure 2.7) in liver segments 1-3.

Regardless, the general architecture of segment 4 appeared to be less organized (figure 2.7) compared to the other segments and this is probably due to the liver split procedure performed before the decellularisation process. Thus, the future aim is to obtain 3 decellularised segments by dissecting segment 4 after decellularisation for future application in organ recellularisation and transplantation.

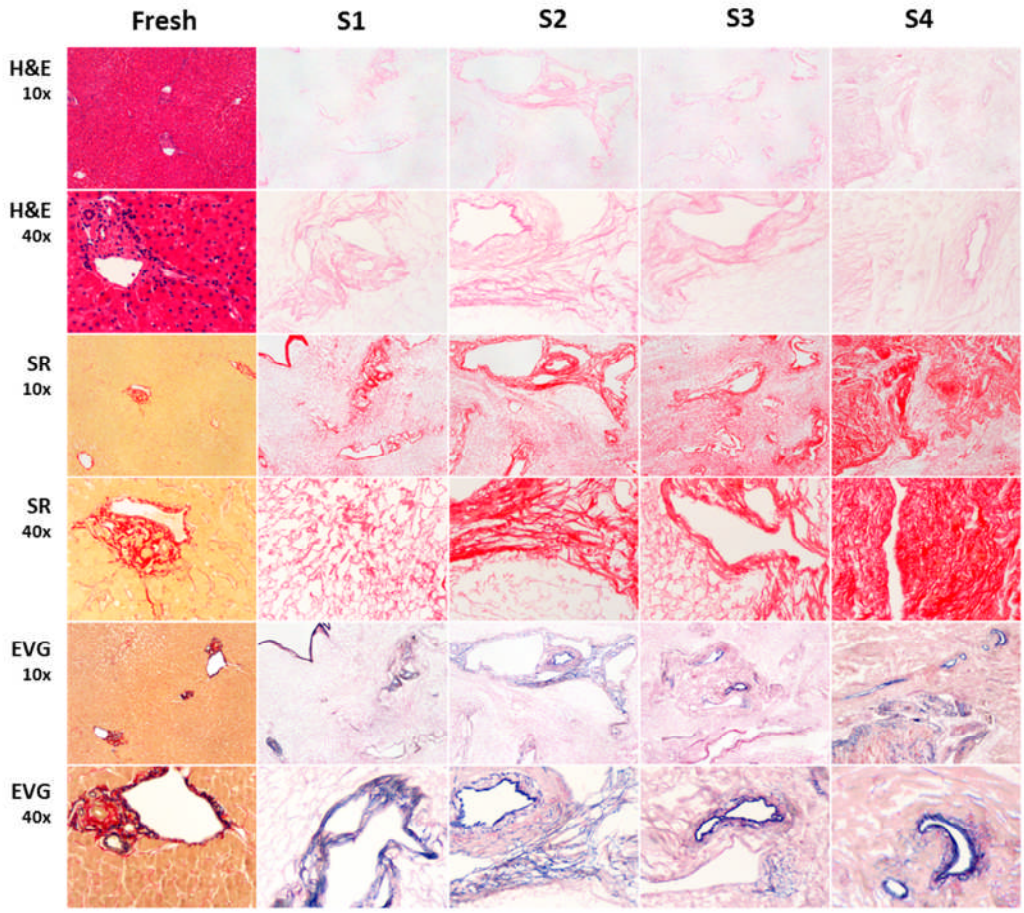

Figure 2.7. Histological comparison of fresh liver tissue and the decellularised human liver left lobe segments (S1, S2, S3 and S4). H&E staining showed removal of cells after decellularisation and SR and EVG (Elastic Van Gieson) stainings show collagen (red) and elastin (blue) preservation, respectively.

A key condition to translate the whole human liver acellular scaffold technology for whole organ recellularisation and transplantation is the preservation of the

vascular tree. Therefore, the vascular (PV and HA) and biliary structure were dissected and analysed by employing histology. As shown in figure 2.8, H&E staining confirmed nuclei removal in all the processed vascular and biliary structures indicating that the retrograde system was efficient in delivering the decellularisation reagents into the portal vein, hepatic artery and bile duct. Furthermore, SR and EVG staining showed preservation of collagen and elastin filaments in those tissues demonstrating that although the cellular/nuclear material was removed it was possible to preserve key structural features of the vein, artery and bile duct.

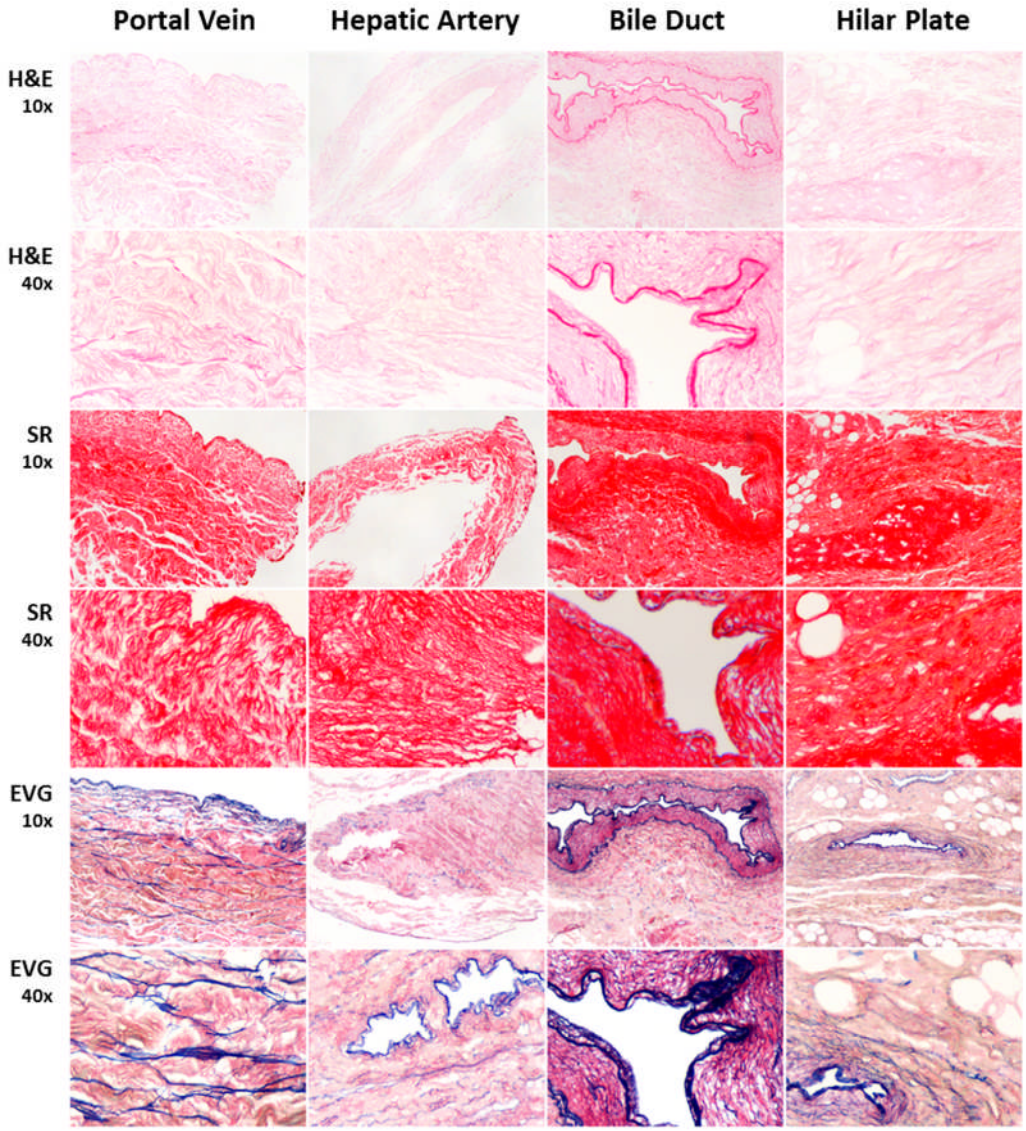

Figure 2.8. Histological sections of the decellularised vascular (portal vein, hepatic artery and hilar plate) and biliar tree. H&E shows absence of cells in the decellularised tissues. SR and EVG stainings show collagen (red) and elastin (blue) preservation, respectively.

Moreover, the removal of DNA in the ECM scaffold was confirmed by DNeasy Blood and Tissue kit (Figure 2.9A) confirming that the total amount of DNA left in the tissue was below 50ng/mg of tissue which is considered the acceptable threshold for biological scaffold transplantation[151]. In addition, the total collagen content was quantified and as already reported in other perfusion-decellularisation protocols[173,177,178], collagen content relative to wet weight was increased ($p<0.01$; Figure 2.9B), whereas elastin was decreased ($p<0.01$) in the decellularised tissue (DL) when compared with fresh liver (FL) tissue (Figure 2.9C).

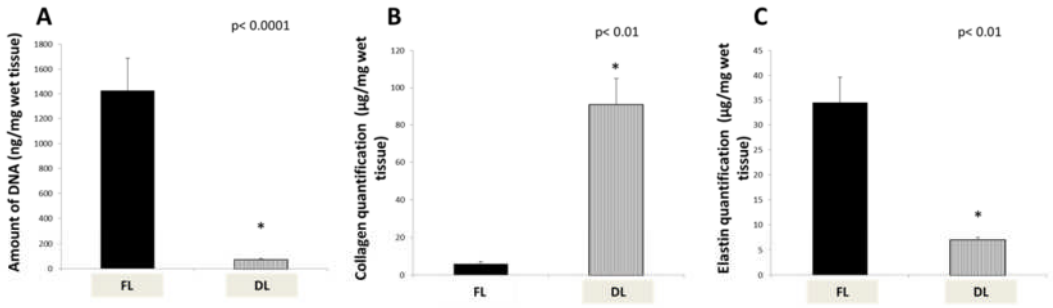

Figure 2.9. Quantification of DNA and ECM proteins in both fresh liver (FL) and decellularised liver (DL). The total amount of DNA(A) is significantly reduced after decellularisation. The collagen content (B) increases while the elastin amount (C) is reduced after decellularisation.

2.3.3 Immunohistochemical characterisation of the decellularised liver

After histologically confirming the preservation of collagen and elastin filaments, a more detailed characterization of the expression and distribution of the ECM proteins was obtained by immunohistochemistry.

This analysis showed that the expression and distribution of key ECM components, namely collagen type I (Figure 2.10c,d), collagen type III (Figure 2.10g,h), fibronectin (Figure 2.10o,p) and collagen IV (Figure 2.10k,l) were conserved when compared to the fresh liver. Importantly, the arrangement of each ECM component within the acellular liver confirmed the preservation of the architectural organisation of the original liver tissue (FL).

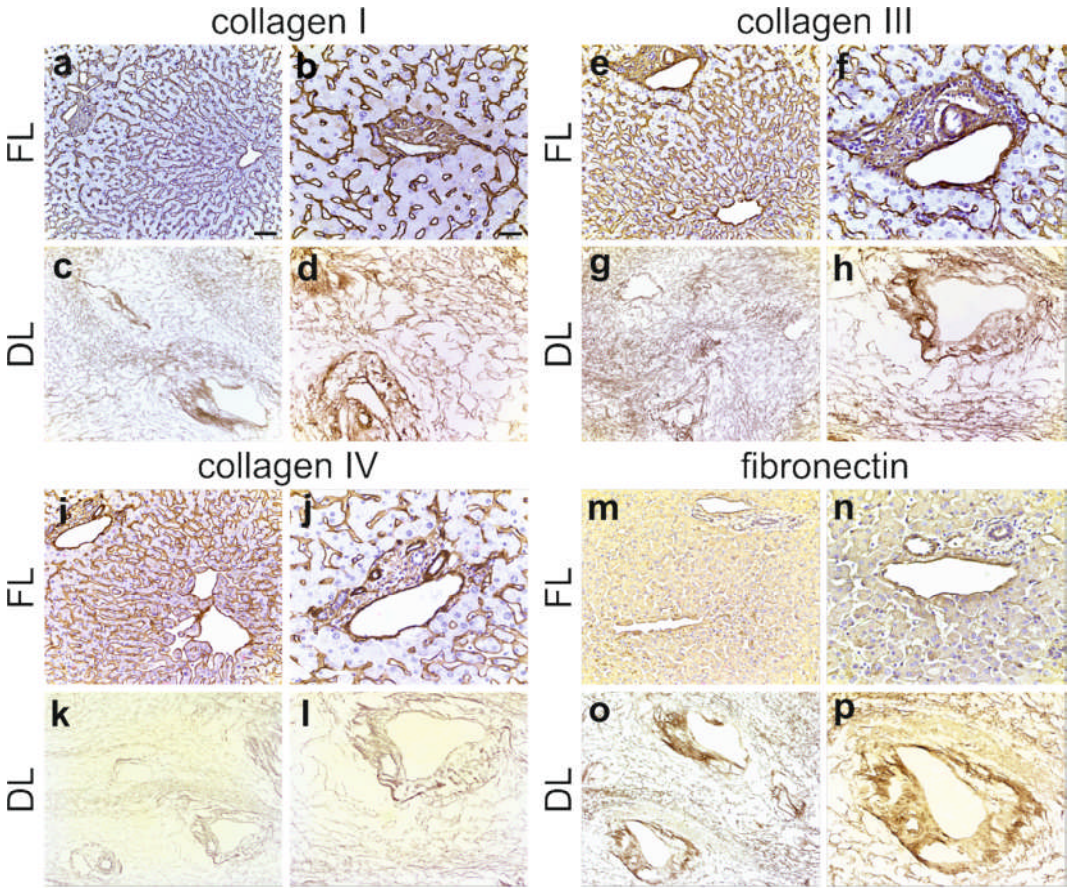

Figure 2.10. Expression and distribution of ECM proteins. Collagen I, III and IV staining in FL is seen as fine strands in the parenchymal space as well as around the blood vessels (a,b; e,f; ij). Collagen I and III distribution was preserved following decellularisation as demonstrated by a staining in both sinusoids and portal tracts in DL (c,d; g,h;). Collagen IV (k,l) and fibronectin (o,p) staining showed a conserved meshwork in sinusoids and biliary ducts after decellularisation. Scale bar for 20x magnification (left panel): 100 μm and 40x (right panel): 50 μm.

2.3.4 Characterization of the hepatic micro-architecture after decellularisation

The preservation of the ECM 3D-architecture and micro-structure is a key condition for the development of acellular scaffolds. Thus, scanning electron microscopy (SEM) was performed in order to evaluate the 3D hepatic micro-architecture after decellularisation.

Initially, the overall hepatic micro-architecture was assessed at low magnification resolution. Importantly, the portal tract and the area of the liver lobule were preserved (figure 2.11). Next, the hepatic lobule was analysed at higher magnification and this confirmed preservation of the hepatic honey-comb like

structure (figure 2.12-14). Interestingly, the ECM-hepatic network was characterised by thin layers of structural filaments with preserved organisation.
Furthermore, the hepatocyte area was assessed by scanning the tissue at higher magnification. Notably, the hepatocyte-free space was recognised at this magnification and it was composed by a refined network of ECM proteins surrounding the hepatocyte pocket (figure 2.15).
Lastly, we investigated the microstructure of decellularised intra-hepatic vessels. The intra-hepatic artery was recognised due to the muscle-like fibres with the preservation of the inner luminal layer (figure 2.16).

Overall, these observations confirmed that the decellularisation procedure preserved the 3D hepatic microanatomy while removing cellular materials.

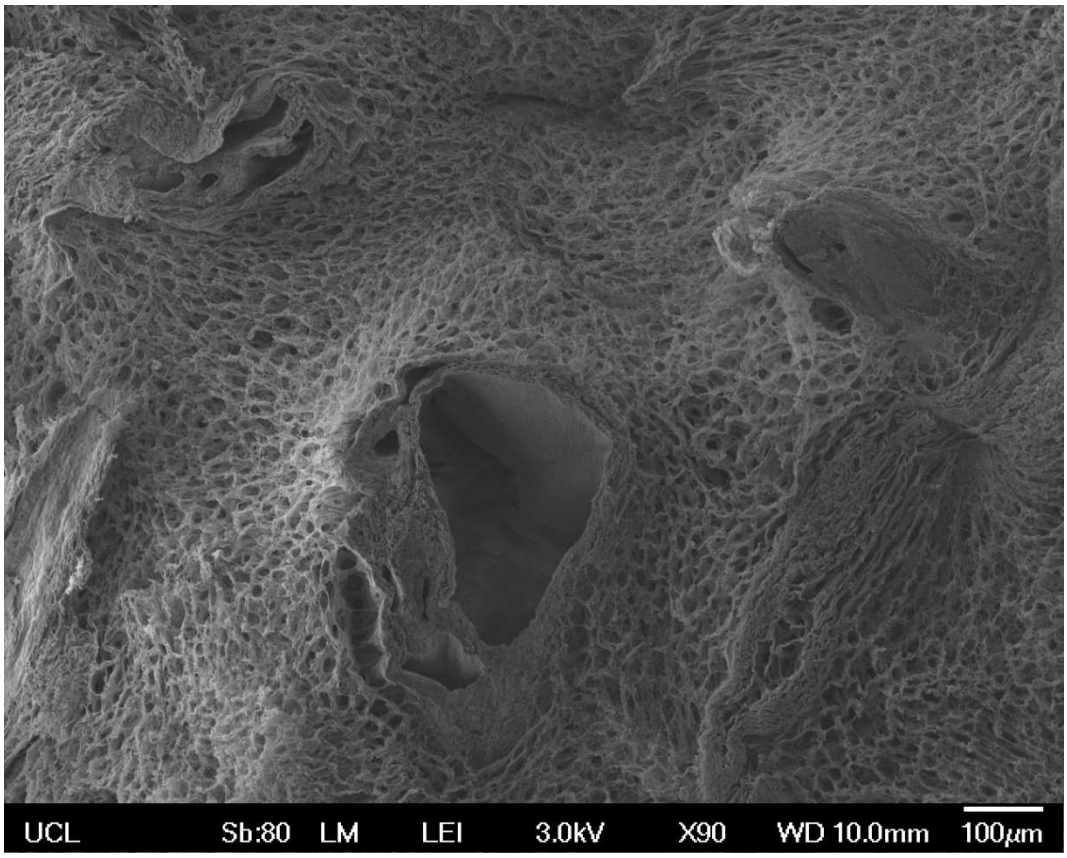

Figure 2.11. Ultrastructural characaterisation of decellularised liver. Low magnification (90x) SEM image including a portal tract surrounded by a typical lobular structure.

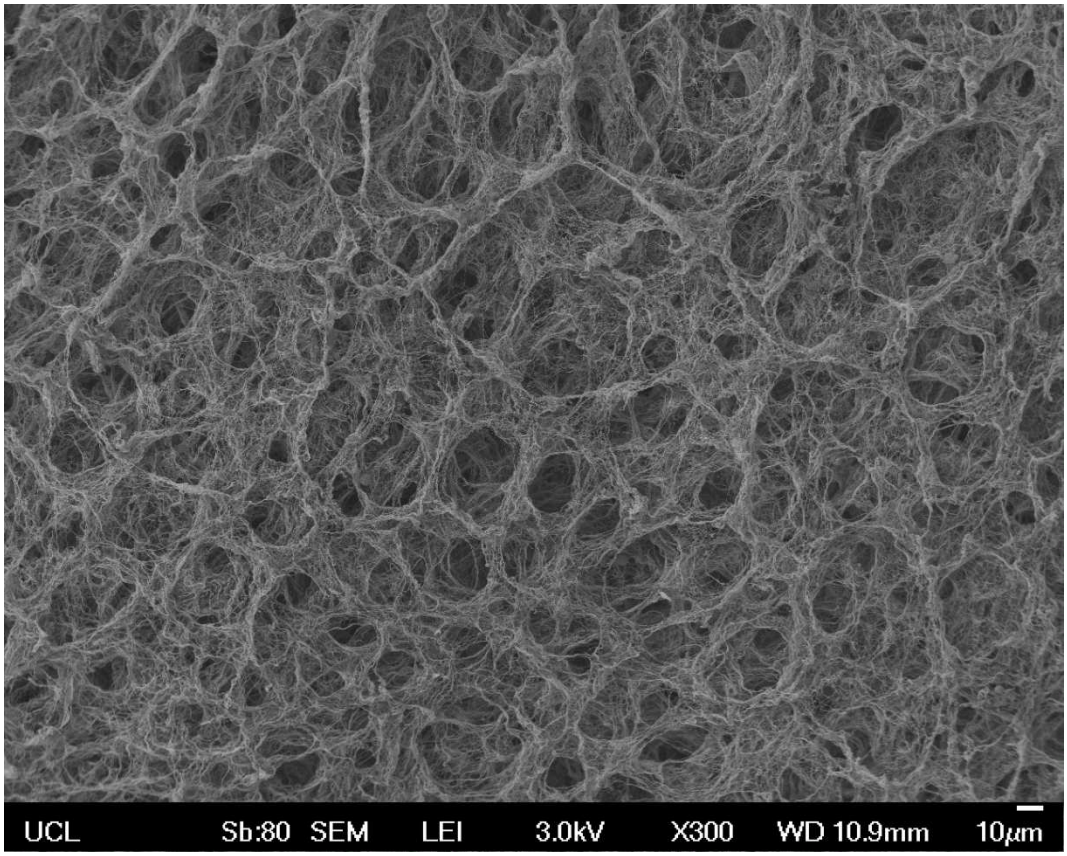

Figure 2.12. Ultrastructural characaterisation of decellularised liver. SEM image (300x) confirming scaffold acellularity and clearly defining spaces once occupied by hepatocytes (i.e. hepatocyte-free spaces).

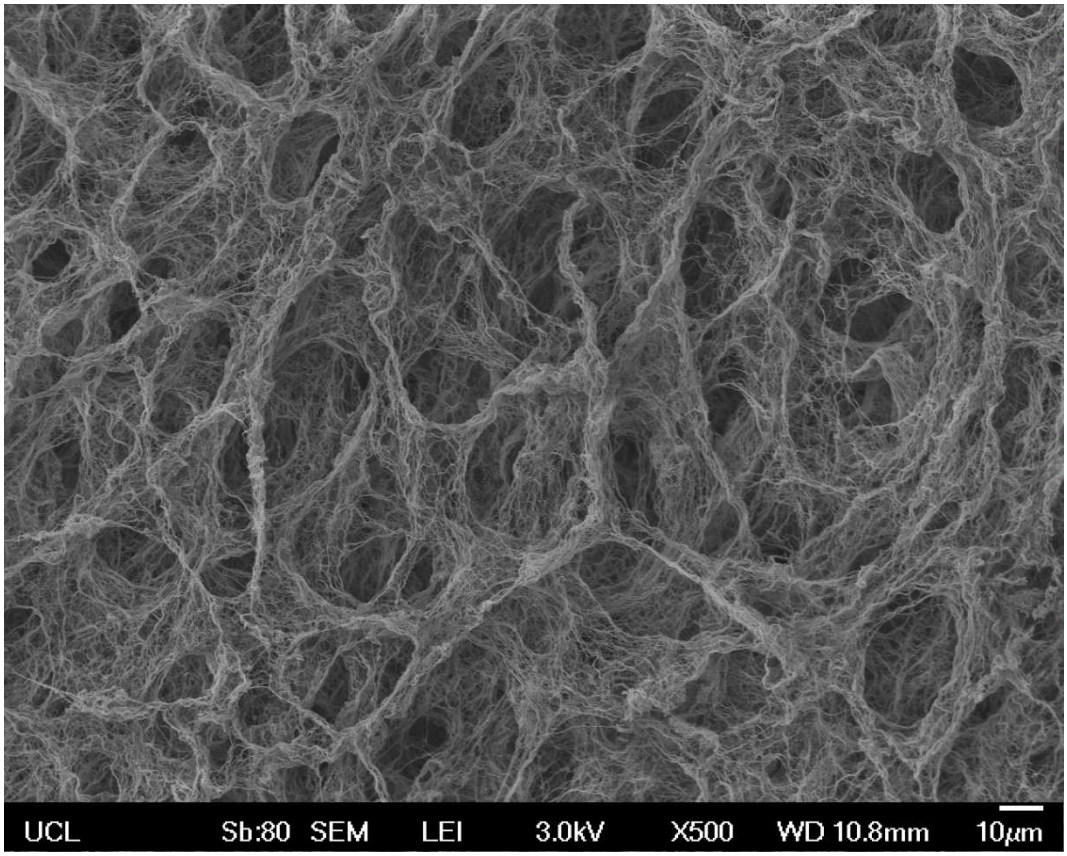

Figure 2.13. Ultrastructural characaterisation of decellularised liver. SEM image (500x) defining ECM filaments network within the liver lobule.

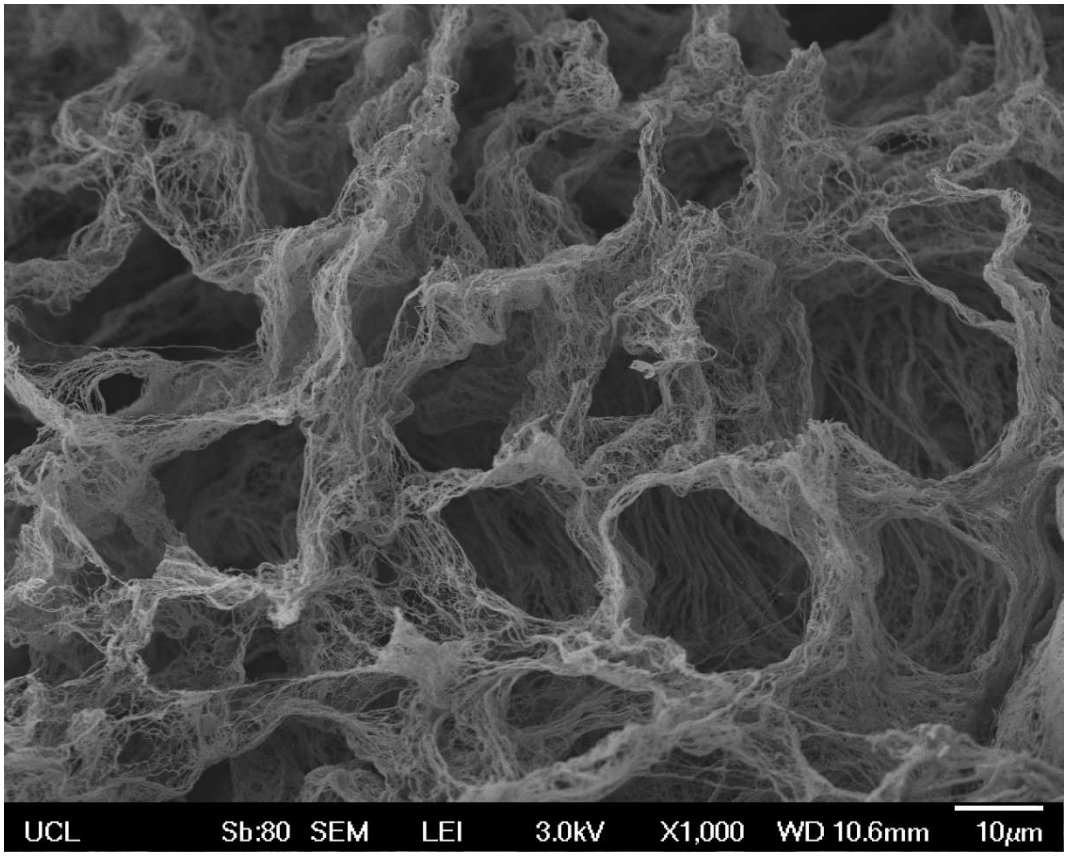

Figure 2.14. Ultrastructural characaterisation of decellularised liver. SEM image (1000x) showing different hepatocytes-free space.

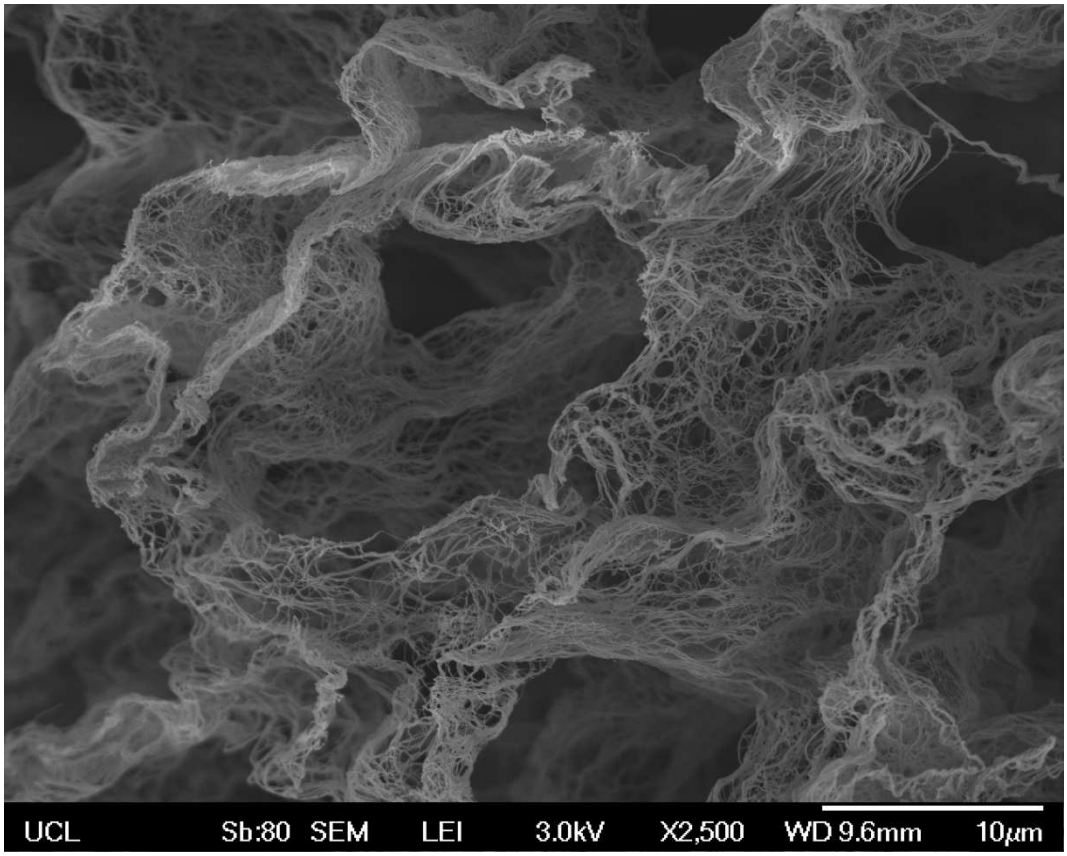

Figure 2.15. Ultrastructural characaterisation of decellularised liver. High magnification (2500x) SEM image demonstrating a preserved three-dimensional meshwork of connective tissue fibres structuring the hepatocyte-free spaces.

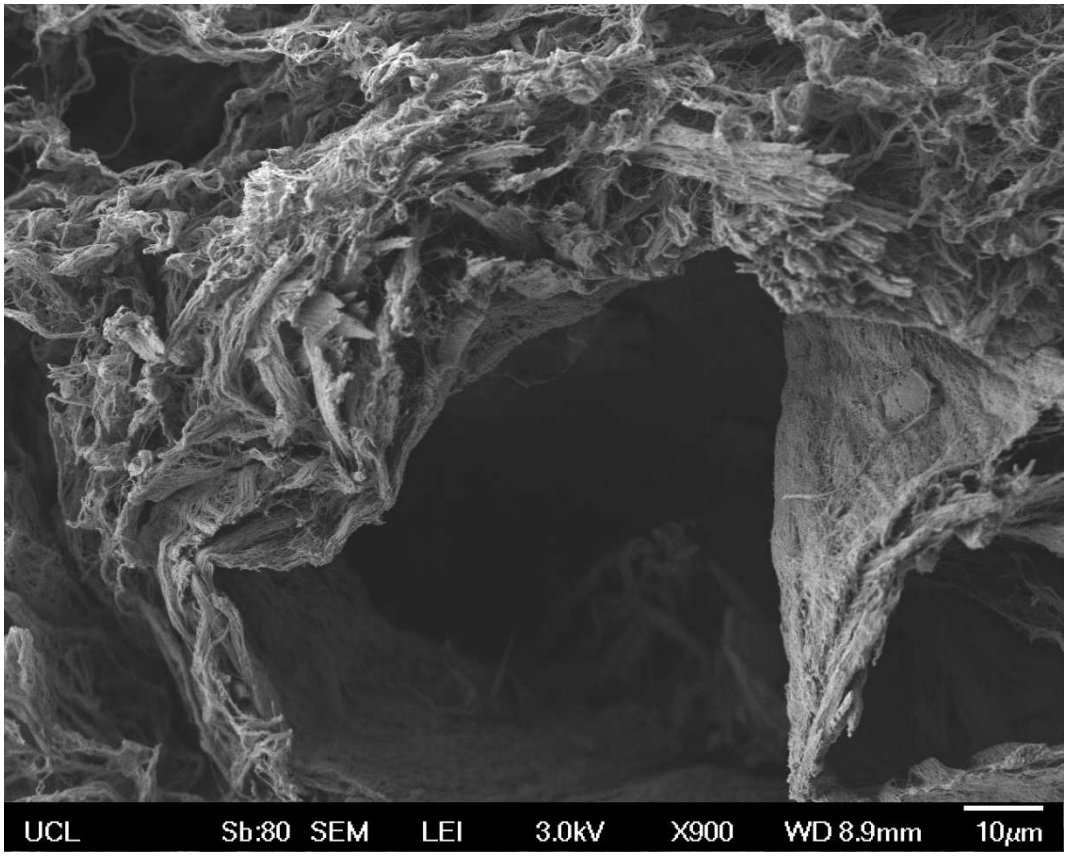

Figure 2.16. Ultrastructural characaterisation of decellularised liver. SEM images (900x) demonstrating preservation of an intra-hepatic artery surrounded by muscle fibres with preserved inner luminal wall.

2.3.5 Interspecies bio-compatibility of decellularized human liver ECM scaffolds

After confirming the acellularity of the human liver scaffold, we next assessed the *in vivo* biocompatibility in a xenotransplantation model. Thus, the decellularised human liver was dissected into 125mm^3 cubes and implanted into immunocompetent mice.

These tissues were implanted either subcutaneously (n=6) or into the omentum (n=6), and evaluated at 7 and 21 days post-implantation.

Clinical behaviour of animals and local signs of inflammation were carefully checked. Both subcutaneous and omental implanted acellular tissues were assessed macroscopically, histologically and immunohistochemically for the presence of inflammatory response, foreign body reaction and neo-angiogenesis.

During the period of observation, mice showed normal behaviour, without local signs of inflammation, implant exposure, extrusion or death. Macroscopic examination at the time of enucleation showed no signs of inflammation around the implants, such as redness and swelling, or adverse tissue reactions around the implants, such as destruction of normal structures, at both subcutaneous and omental sites (Figures 2.17 and 2.18, panels a,e, respectively).

Histological analysis showed absence of a foreign body reaction indicated by the absence of giant cells or granulomata within any of the samples. Polymorphonuclear cells and lymphocytes were observed at 7 days post-implantation, indicating a mild inflammatory response surrounding the implantation sites. Inflammatory cells were mostly seen in the tissue around the implants (Figures 2.17 and 2.18, panels b,c). By contrast, at 21 days post-implantation, reduced or no inflammatory infiltrate was observed around the implants (Figures 2.17 and 2.18, panels f,g).

Immunohistochemistry for α-SMA revealed that alpha-SMA-negative, spindle-like cells had infiltrated the implants after 21 days post-implantation (Figures 2.17 and 2.18, panel h). On the other hand, positivity for alpha-SMA indicated the presence of abundant neo-vessels (mostly arterioles), initially close to the interface host tissue/human scaffold (7 days, Figures 2.17 and 2.18, panel d) and subsequently deeper within the scaffold (21 days, Figures 2.17 and 2.18, panel h), thus providing evidence for neovascularisation of the implant.

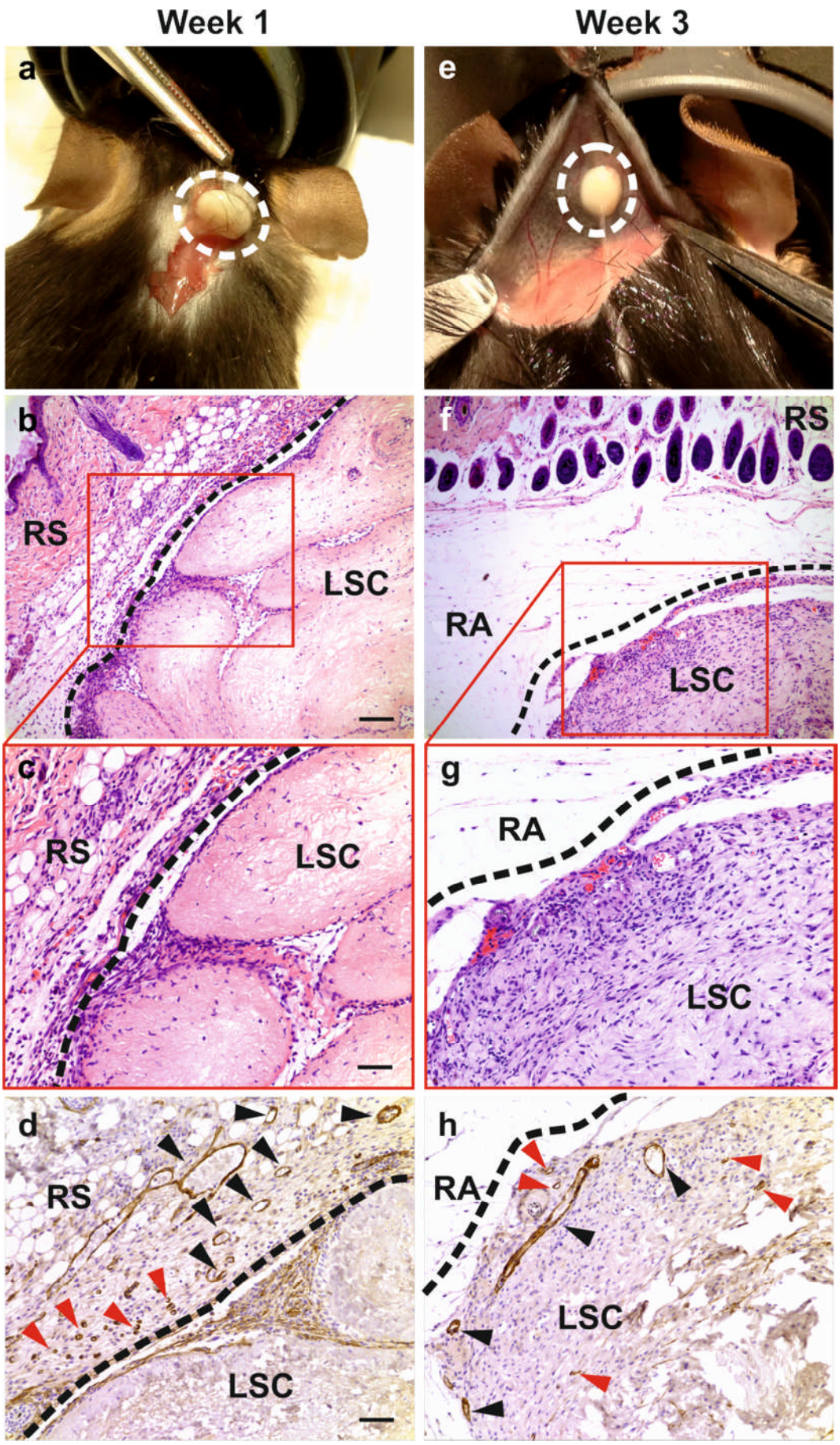
Week 1
Week 3
a
e
b
RS
LSC
f
RS
RA
LSC
c
RS
LSC
g
RA
LSC
d
RS
LSC
h
RA
LSC

Figure 2.17. Subcutaneous implantation of liver cubic scaffolds in immunocompetent mice. Human liver cubic scaffolds were implanted subcutaneously (n=6) and evaluated at 7 and 21 days post-implantation. Polymorphonuclear cells and lymphocytes were observed at 7 days post-implantation, indicating a mild inflammatory response. Inflammatory cells were mostly seen in the tissue around the implants (b,c). By contrast, at 21 days post-implantation, little or no inflammatory infiltrate was observed around the implants (panels f,g). Immunohistochemistry for alpha-SMA showed SMA-negative, spindle-like cells, (most likely fibroblasts), had infiltrated the implants after 21 days post-implantation (h) and revealed the presence of abundant neo-vessels (mostly arterioles) initially close to the interface host tissue/human scaffold (7 days, d, arrows) and subsequently deeper within the scaffold (21 days, h, arrows) indicating neovascularisation of the implant. Scale bars: for 10x (b,f), 20x (c,d,g,h) magnification: 100 μm.

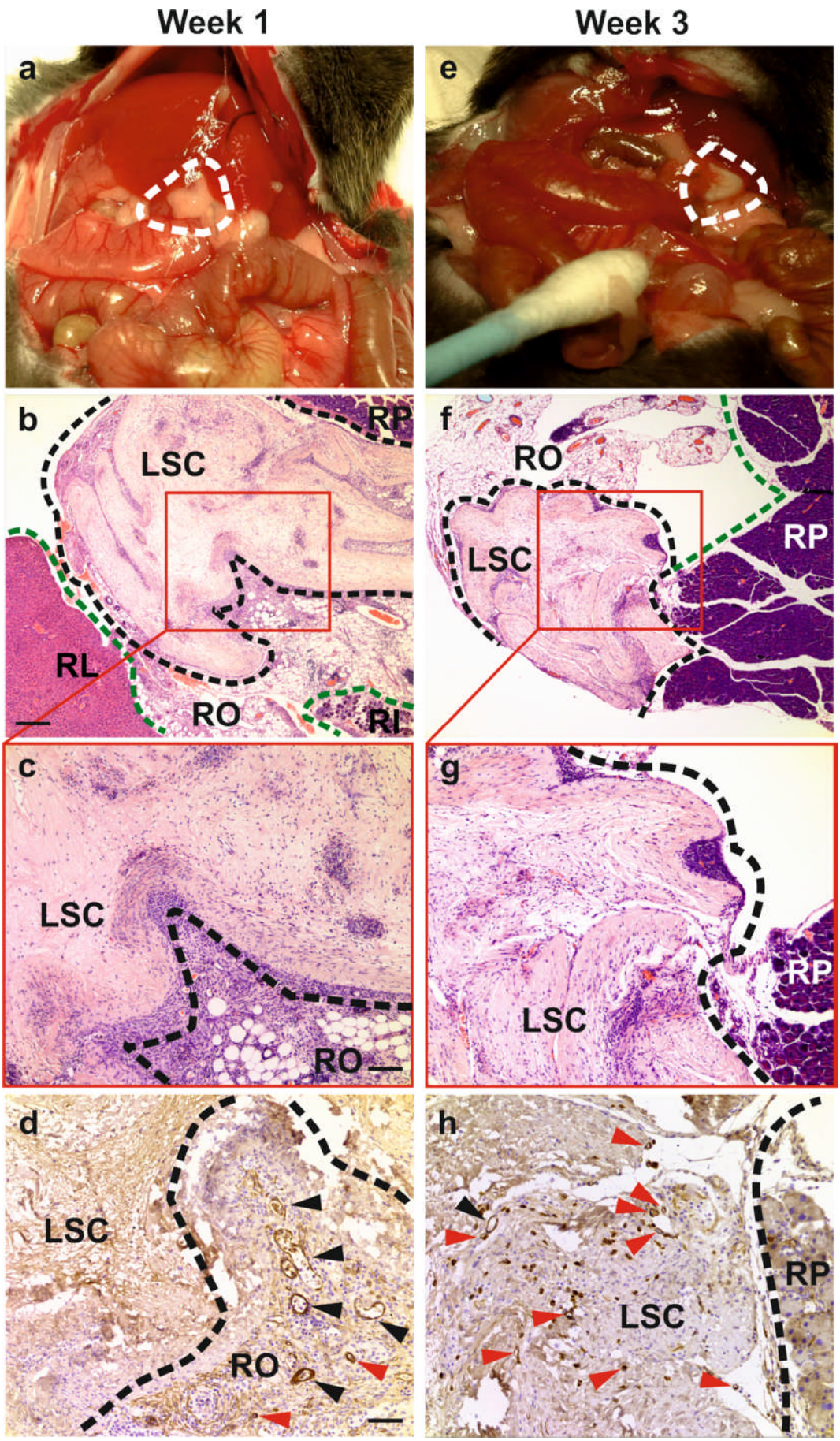
Week 1
Week 3
a
e
b
RP
LSC
RL
RO
RL
f
RO
LSC
RP
c
LSC
RO
g
RP
LSC
d
LSC
RO
h
RP
LSC

Figure 2.18. Liver cubic scaffolds implantation into the omentum of immunocompetent mice. Human liver cubic scaffolds were implanted into the omentum (n=6), and evaluated at 7 and 21 days post-implantation. As early as seven days after implantation, the implanted scaffold engrafted within the surrounding host abdominal structures: recipient liver (RL), recipient intestine (RI) and recipient pancreas (RP). Polymorphonuclear cells and lymphocytes were observed at 7 days post-implantation, indicating a mild inflammatory response. Inflammatory cells were mostly seen in the tissue around the implants (b,c). By contrast, at 21 days post-implantation, little or no inflammatory infiltrate was observed around the implants (panels f,g). Immunohistochemistry for alpha-SMA showed SMA-negative, spindle-like cells, (most likely fibroblasts), had infiltrated the implants after 21 days post-implantation (h) and revealed the presence of abundant neo-vessels (mostly arterioles) initially close to the interface host tissue/human scaffold (7 days, d, arrows) and subsequently deeper within the scaffold (21 days, h, arrows) indicating neovascularisation of the implants. Scale bars: for 4x (b,f), 10x (c,g) and 20x (d,h) magnification: 100 μm.

2.3.6 Re-population of decellularized human liver ECM scaffolds with human liver cell types

The *in vitro* biocompatibility was performed by reseeding the decellularised human liver cubes with LX2 (a human hepatic stellate cell line), HepG2 (epithelial cells derived from hepatoblastoma) or Sk-Hep-1 (endothelial cells, derived from highly invasive human adenocarcinoma) human cell types (Figure 2.19, 2.20 and 2.21).

Engineered tissues were evaluated after 7, 14 and 21 days of *in vitro* culture.

H&E staining showed that LX2 progressively engrafted into the acellular tissues over 21 days (Figure 2.19 A) with a marked presence of proliferative cells (Figure 2.19 B). In addition, the number of cells increased significantly (Figure 2.19 C) between 7, 14 and 21 days of culture ($p<0.05$ and $p<0.001$ at 14 days and 21 days, respectively). SEM analysis (Figure 2.19 D) further confirmed that LX2 cells migrated within the decellularised liver showing different morphologies: from a flattened fibroblast-like cell phenotype, likely migratory, to a round-up shape probably indicating mitosis.

Human hepatoblastoma cell lines (HepG2) successfully engrafted into the acellular livers and migrated through the scaffold during the reseeding time (Figure 2.20 A). Repopulation with HepG2 cells was also characterized by Ki67

positivity indicating cells proliferation (Figure 2.20 B). Accordingly, there was a marked increase in cell number between 7, 14 and 21 days (Figure 7h; $p<0.05$ and $p<0.004$ at 14 days and 21 days, respectively). SEM indicated that HepG2 cells were homogenously distributed into the decellularised liver parenchyma and exhibited an epithelioid phenotype (Figure 2.20 D).

Metastatic Sk-Hep-1 cells were able to repopulate the liver scaffolds (Figure 2.21 A) showing a high proliferation rate (Figure 2.21 B) and the total number of cells was remarkably increased between 7, 14 and 21 days (Figure 7l; $p<0.003$ and $p<0.008$ at 14 and 21 days, respectively). In addition, SEM analysis showed that these cells were able to migrate/invade within different layers of the engineered liver scaffold showing a mesenchymal-like phenotype (Figure 2.21 D).

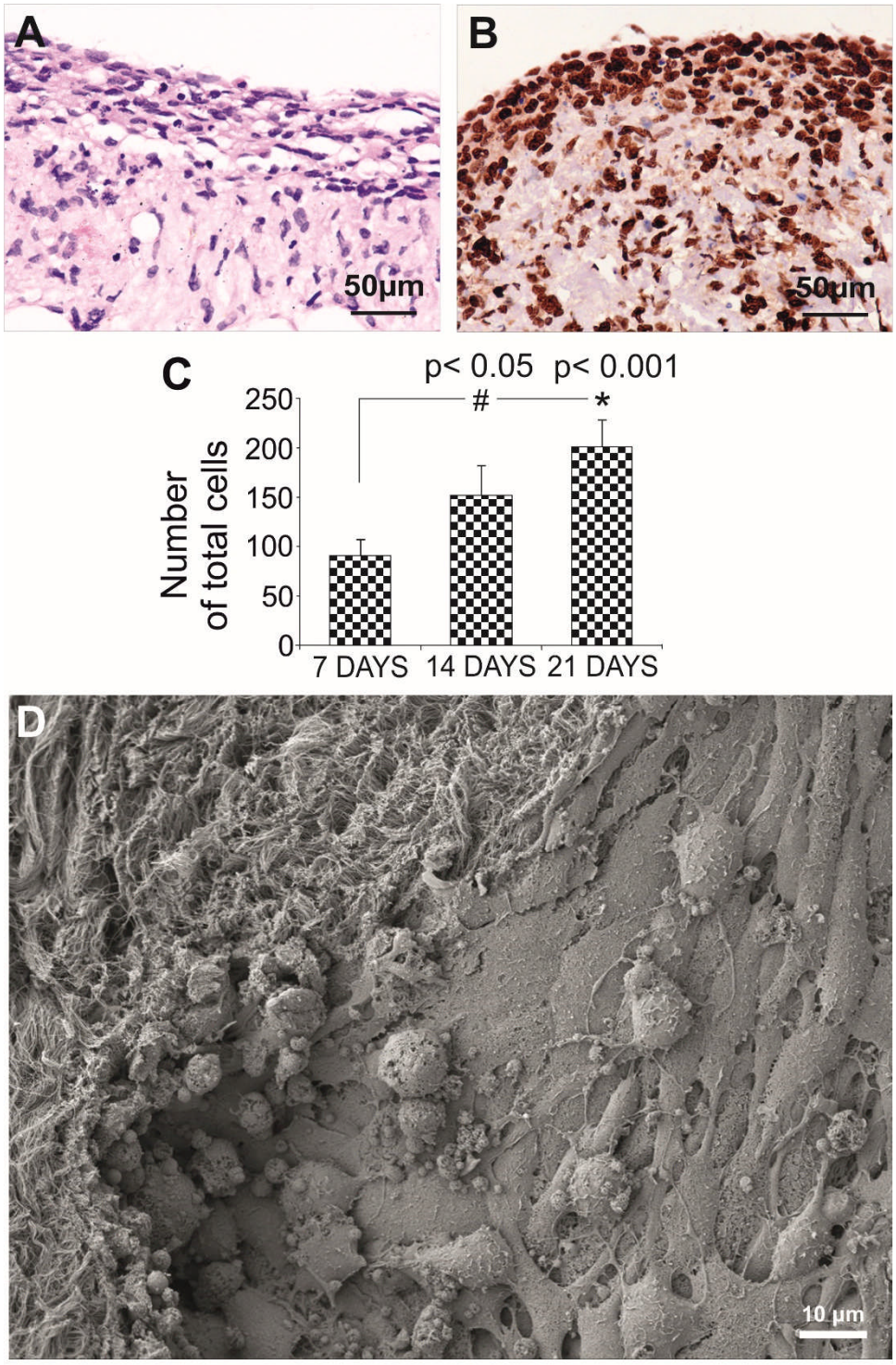

Figure 2.19. Recellularization of human liver with LX2. H&E (A) and KI67 (B) showed cell engraftment and proliferation after 21 days of bioengineering. The total cell count increased significantly between 7 and 14-21 days(C). Scale bar 40X magnification: 50µm. SEM (D) showed that cells migrated within the decellularised sinusoidal space acquiring both fibroblast-like and rounded shape morphology.

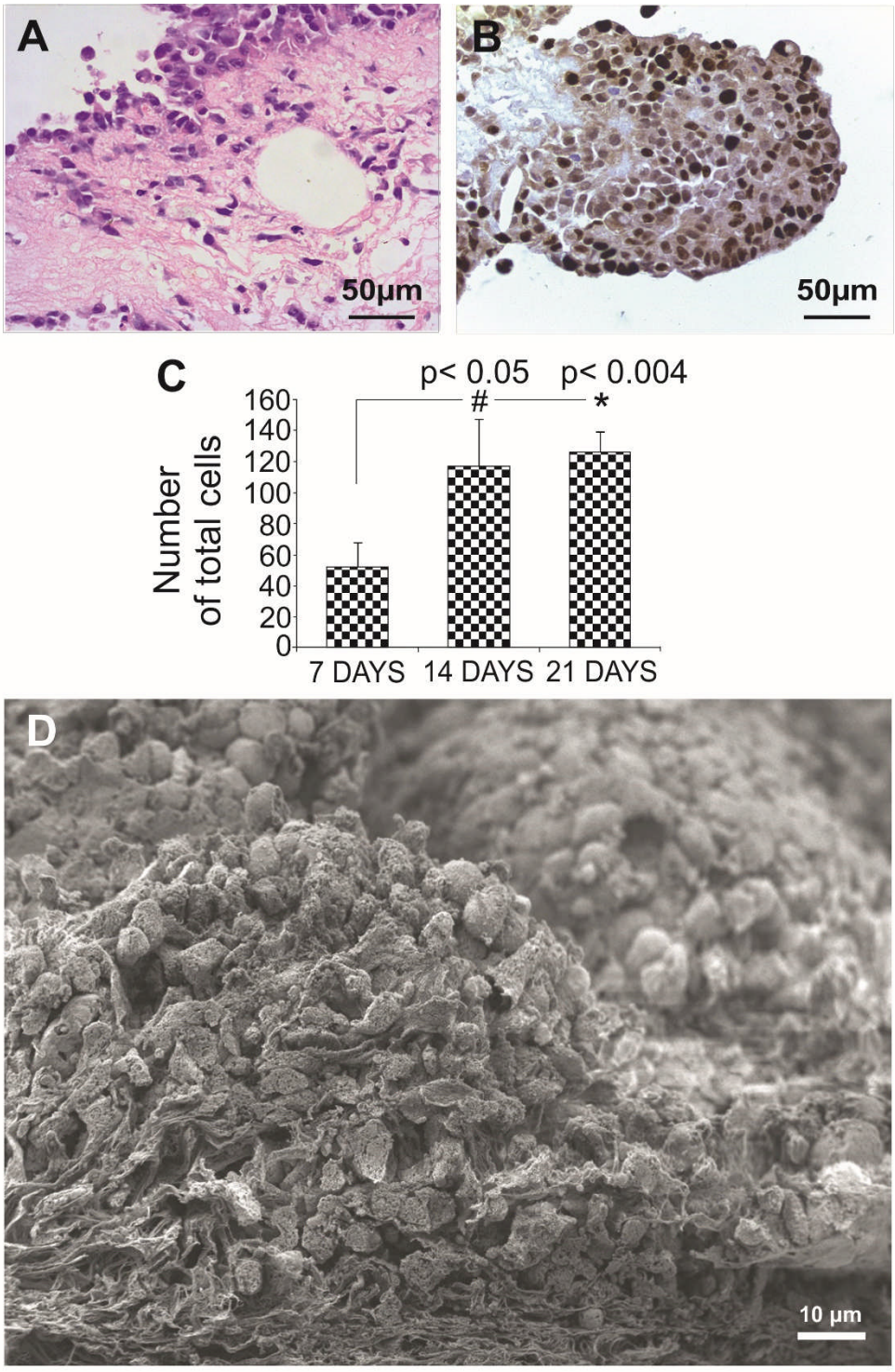

Figure 2.20. Recellularization of human liver with HepG2. H&E (A) and KI67 (B) showed cell engraftment and proliferation after 21 days of bioengineering. The total cell count increased significantly between 7 and 14-21 days(C). Scale bar 40X magnification: 50µm. SEM (D) showed that cells were spread through the parenchymal of the decellularised tissue acquiring rounded shape morphology.

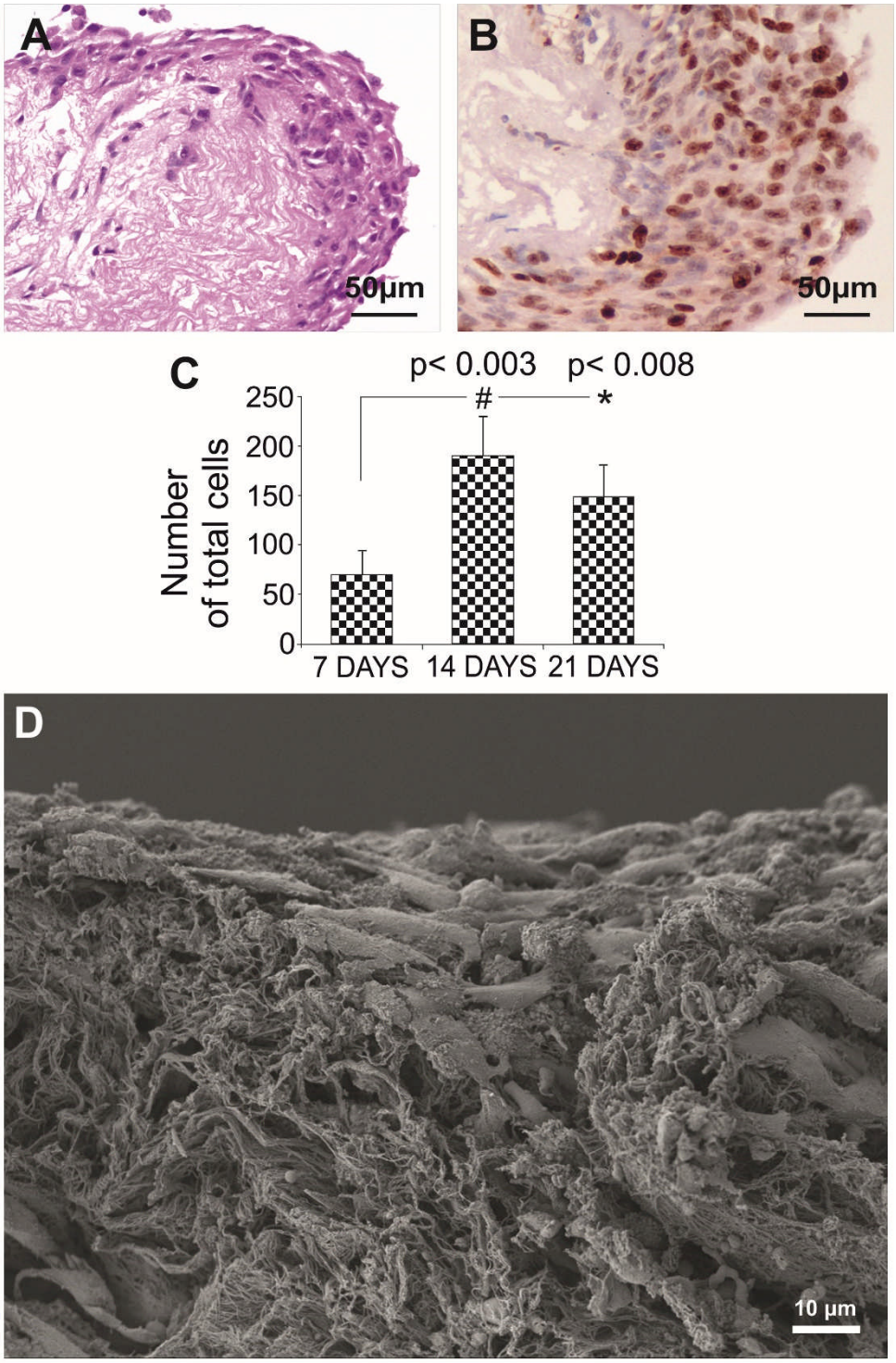

Figure 2.21. Recellularization of human liver with SK-Hep. H&E (A) and KI67 (B) showed cell engraftment and proliferation after 21 days of bioengineering. The total cell count increased significantly between 7 and 14 days(C). Scale bar 40X magnification: 50µm. SEM (D) showed that cells invaded the parenchymal of the decellularised tissue acquiring fibroblast-like shape morphology.

Discussion

The experiments and results presented in this chapter demonstrated the feasibility of obtaining acellular whole human livers starting from unsuitable organs for transplantation.

The work herein described was recently published[156] and so far this is the first report describing the decellularisation of whole human liver and human liver left lobe.

Paul Lin *et al.* firstly showed decellularisation of porcine hepatic tissue in 2004. After decellularisation, the tissue was lyophilised in order to develop ECM gel-discs in combination with repopulating with primary rat hepatocytes. Interestingly, these cells were characterised by a significant higher production of albumin and urea when compared to either monolayers or collagen sandwich cultures[124].

After this pioneering work, different reports have demonstrated the successful decellularisation of xenogenic livers including rat, rabbit or pig livers[120,171-173].

However, the main challenge was to scale up the decellularisation methodology in order to obtain human-size liver biological scaffold. Recently, Baptista *et al.* have effectively decellularised porcine livers and these scaffolds were repopulated with human foetal hepatocytes and foetal hepatic stellate cells for up to 13 days. The engineered humanised liver showed active metabolism and albumin synthesis[46].

However, the microanatomy of porcine liver is characterised by defined lobules with connective tissue, which is absent in healthy human liver but present in fibrotic liver[179]. Therefore, porcine liver scaffold may not represent the ideal ECM for human liver tissue engineering. Indeed, it is not known whether these differences in ultrastructure could cause complications once an engineered porcine liver scaffold is transplanted in humans. For instance, it is possible that portal hypertension or intravascular problems within the portal circulation would develop if a porcine graft implant is connected with the human portal vascular system.

Hence, due the high number of organs not suitable for transplantation as well as key ultrastructural and architectural specific features of human liver, it would be

ideal to improve the usage of these organs for tissue engineering and regenerative medicine.

A major limiting factor to decellularise whole human liver as well as liver left lobes was the inability of previously published protocols for generating human-size liver scaffold to be effective in removing cellular materials from human livers. Indeed, the initial designed protocol required antegrade perfusion and constant flow rate as previously described[180]. However, after 6 weeks perfusion the liver was not affected by the procedure. Afterwards, we adopted a more complex system by perfusing the liver left lobe at constant flow rate through both portal vein and hepatic artery. Despite this modification, the liver appeared macroscopically brownish indicating lack of efficiency of the decellularisation protocol. Thus, a more elaborate novel methodology was established aimed at improving the perfusion of the whole organ by adopting retrograde perfusion as well as a two steps perfusion rate in order to maintain the appropriate pressure during the whole decellularisation procedure.
The retrograde perfusion concept was firstly introduced by the pioneering work of Ott and colleagues which firstly showed the feasibility of obtaining whole organ biological scaffold[154].

The novel procedure demonstrated to be successful in removing cellular materials while preserving the 3D-architecture and ECM protein composition. Indeed, collagen I, IV and fibronectin were maintained after decellularisation and were homogenously distributed within the acellular liver tissue. In addition, the preservation of the 3D architecture was confirmed by scanning electron microscopy where portal tract, liver lobule as well as the hepatocyte-free space were identified.

A key feature of biological scaffold is the immunomodulatory effect upon transplantation[181]. The *in vivo* biocompatibility was assessed in a xenotransplantation model by implanting fragments of the acellular human liver either subcutaneously or intra-abdominally into immunocompetent mice. Notably, the decellularised tissues did not induce foreign body formation and the immune response was reduced after 3 weeks of transplantation.

Lastly, the *in vitro* biocompatibility was evaluated by reseeding decellularised human liver cubic fragments with different types of human liver cell lines including human hepatic stellate cells LX2[182], hepatoblastoma cell HepG2[183] and metastatic adenocarcinoma cell SK-Hep1[184].
Notably, all three cell types engrafted and migrated into the acellular liver while maintaining the proliferative phenotype. Therefore, these experiments demonstrated that the decellularised liver retains the key features needed to induce homing and proliferation of human hepatic cells.

Overall the results described in this chapter offer a novel 3D biological platform to be further developed in the area of whole organ engineering by employing unsuitable human organs for transplantation.

Chapter 3: Exploring the relationship between amyloidosis and 3D hepatic ECM

3.1 Introduction

This chapter addresses the development of liver biological scaffolds from both healthy and amyloidotic transgenic mice in order to explore the intimate interaction between amyloid deposit and hepatic-ECM. In addition, this chapter includes the description of an *ex vivo* experimental model for the study of the seeding effect of amyloidogenic proteins. This work is included in the present thesis as an example of the application of the scaffold technology to the study of an important human disease such as amyloidosis where the relationship between amyloid deposits and the 3D ECM structure of the tissue is still obscure.

Some of the data included in this chapter were recently published: **Mazza, G.** et al. Amyloid persistence in decellularized liver: biochemical and histopatological characterization[185].

Amyloidosis is a protein misfolding disorder in which a protein or peptides lose their solubility and self-aggregate into fibrillar polymers that precipitate in the extracellular matrix[186]. The disease can be systemic when several organs are simultaneously involved, or localized when a single organ is affected. Many cases of systemic amyloidosis are characterized by a certain level of tissue specificity of amyloid deposition; in these cases the amyloid deposition is prominent in a specific organ such as the liver, the heart, the spleen or the nerves, and this determines the specific clinical manifestations and prognosis.

Despite much progress in the study of amyloid fibrillogenesis *in vitro*, the formation of amyloid fibrils *in vivo* is poorly understood. Comprehensive elucidation of the processes operating under physiological and pathophysiological conditions is now critical for understanding the natural history of amyloidosis, its

response to available treatments and, crucially, the development of new and more effective therapies.

Interestingly, clinical and experimental evidence suggested that some components of the extracellular matrix (ECM), and in particular glycosaminoglycans may play a crucial role in favouring the conversion of proteins into cross-beta fibrillar structure and determining the tissue tropism of amyloid deposits by locally accelerating the protein aggregation [187].

However, the precise analysis of the interaction between amyloid and the hepatic ECM *in vivo* or *ex vivo* material has been limited by for the very high complexity of any tissue in which cells are fully or partially conserved.

Therefore, we decided to employ the process of tissue decellularisation in conditions suitable for the best conservation of the ECM network in order to reduce the structural complexity of the affected organ. The feasibility of this idea was supported by the pioneering work performed in 1986 by Bonsib and Plattner [188]. Their research was aimed at improving the microscopic visualization of amyloid and glomeruli basement membranes through the decellularisation of small kidney biopsies. However, the decellularisation of an entire amyloidotic organ had not previously been demonstrated. Similarly, the use of an entire liver 3D scaffold to study the deposition of amyloidotic proteins has never been previously proposed.

As already mentioned in this thesis, successful creation of biological scaffolds for whole organ engineering has been achieved by decellularisation of organs derived from different tissues and species[189-192]. This process maintains the natural 3D architecture, ultrastructure of the ECM as well as the patency of the vascular network[193].

The decellularisation procedure can be tailored based on the complexity of the tissue as well as the size. Therefore, cellular materials can be removed by employing mild procedures for small-size tissue, such us mouse liver in order to

better preserve the biochemical composition, the bioactivity and the physical properties of the ECM [194].

Therefore, the next section of this chapter will describe the development and characterisation of liver biological scaffolds from healthy and transgenic amyloidotic mice. Moreover, the application of the whole organ mouse liver scaffold will be tested in order to investigate human protein fibrillogenesis into 3D-ECM scaffolds.

3.2 Methods

3.2.1 Transgenic mice

Amyloidosis was induced in transgenic mice, which were homozygous for both the rTALap1 and SAA transgenes, when treated with doxycycline. Briefly, AEF was injected into animals receiving 2 mg/ml doxycyclinein in their drinking water for 10 days after AEF administration. This protocol consistently results in extremely large amyloid loads [195].

3.2.2 Harvest of organs for decellularization

Mice were killed by CO_2 inhalation. The abdomen was sterilized with 70% ethanol and a U-shaped incision was performed to expose the abdominopelvic cavity. The abdominal inferior vena cava (IVC) and portal vein (PV) were identified and the PV was cannulated with a 24G cannula (Beckton-Dickinson), which was secured in place with a 3-0 silk suture (Ethicon, UK). The abdominal IVC was sectioned and 200 U of heparin injected into the portal vein. The diaphragm was used as a holding point to release the whole liver from the supporting tissue. The whole procedure was carried out with special caution not to damage the Glisson's capsule.

3.2.3 Decellularization procedure

Mice livers were connected to a peristaltic pump (Masterflex) via the cannulated PV and perfused with deionized water for 36 h at 4 °C. Livers were then transferred to room temperature and were perfused with 4% (w/v) sodium deoxycholate (SDC) (Sigma, UK) for 6 h followed by perfusion of 500 kU/ml of DNase-I from bovine pancreas (Sigma, UK) in 1 M sodium chloride (NaCl) for 3 h. The flow rate was kept at 4.5 ml/min for the water infusion and 6.5 ml/min for SDC and DNase steps. Following the end of the decellularization cycle (deionised water-SDC-DNAse) the livers were perfused with PBS with 1% antibiotic/antimycotic (Sigma, UK) for 30 minutes and stored in the same buffer at 4 °C. The whole procedure was carried out with special caution not to remove or damage the PV cannula.

3.2.4 Histology and Immunohistochemistry

Samples were fixed for at least 24 h in 10% neutral buffered formalin solution (pH 7.4) at room temperature. Tissue was embedded in wax and sectioned at 4 µm. Sections were dewaxed in xylene and rehydrated using graded industrial denatured alcohol (IDA) before staining with Harris's haematoxylin and eosin (H&E) (Leica, Germany), or Picro-Sirius Red (SR) (Hopkin & Williams) (BDH Chemicals Ltd) or Miller's Elastic with a SR counter stain (VWR, Leica, Raymond A Lamb).

For AA immunohistochemistry, 2 µm sections were de-waxed, rehydrated, and endogenous peroxidase blocked with 0.6 % hydrogen peroxidase. Sections were then washed in PBS, and non-specific antibody binding was blocked by incubation in 2.5 % v/v heat inactivated normal horse serum (Vector Labs, Burlingame, CA) for 30 min at room temperature. After washing, slides were incubated with anti-mouse SAA antibody Ab AF2948 (R&D Systems, Abingdon, UK) diluted in Dako Antibody Diluent (1/100) overnight at 4 °C. Slides were then incubated with IMMpress anti-goat polymer (Vector Labs, Burlingame, CA)

for 30 min at room temperature, washed, and incubated for 10 min with DAB/Metal (Thermo) diluted (1:10) in stable H_2O_2 substrate buffer. After terminating the reaction by washing, slides were counterstained with Myers hematoxylin for 30 s. Congo red staining was performed by the method of Puchtler et al (1985) [196]; viewing under high intensity cross polarized light revealed the pathognomonic green birefringence of Congo red stained amyloid.

3.2.5 DNA quantification

Total DNA content within native tissue and acellular matrices was measured using the DNeasy Blood and Tissue kit according to the manufacturer's manual (Qiagen). Briefly, specimens were digested with Proteinase K overnight, and DNA was purified on a spin column; purity and yield of purified DNA were assessed with spectrophotometric measurements at 260 and 280 nm.

3.2.6 Scanning Electron Microscopy (SEM)

Samples were fixed in 2.5% v/v glutaraldehyde in 0.1 M phosphate buffer and left for 24 h at 4 °C. Following washing with 0.1 M phosphate buffer, samples were cut into segments of approximately 1 cm length and cryoprotected in 25% sucrose, 10% glycerol in 0.05 M PBS (pH 7.4) for 2 h, then fast frozen in nitrogen slush and fractured. Samples were then placed back into the cryoprotectant at room temperature and allowed to thaw. After washing in 0.1 M phosphate buffer (pH 7.4), the material was fixed in 1 % OsO4/0.1 M phosphate buffer (pH 7.3) at 3°C for 1.5 h and washed again in 0.1 M phosphate buffer (pH 7.4). After rinsing with water, specimens were dehydrated in a graded ethanol-water series to 100 % ethanol, critical point dried using CO_2 and finally mounted on aluminum stubs using sticky carbon taps. The fractured material was mounted to present fractured surfaces across the parenchyma to the beam and coated with a thin layer of Au/Pd

(approximately 2 nm thick) using a Gatan ion beam coater. Images were recorded with a 7401 FEG scanning electron microscope (Jeol, USA).

3.2.7 Protein composition of AA-mL$_{dec}$ and AA-mL homogenates

Crude homogenates of livers from amyloidotic SAA transgenic mice [195], i.e. AA-*m*L$_{dec}$ or AA-*m*L, were prepared according to the AEF extraction procedure from liver, through a simple homogenization of tissue in physiologic buffer (PBS) followed by a single water extraction that provides a suspension containing amyloid fibrils[197]. Total protein content in homogenates was measured using Pierce BCA protein assay kit (Thermo Scientific) and 2 µgs of total protein were analyzed using homogenous 15% PAGE under denaturing and reducing conditions for further proteomics and immuno-enzymatic analyses. For proteomic characterization, gel bands stained with colloidal Coomassie Blue were trypsin digested before analysis of the extracted peptide mixtures by MALDI-MS (AUTOFLEX III Smartbeam Bruker). Peptide calibration mixture (Bruker Daltonics) in the range between 1000 and 3500 Da was used as external standard.

Immunoblot analysis following 15 % reducing SDS-PAGE was performed with primary goat polyclonal anti-mouse SAA1 antibody (0.2 µg/ml, R&D Systems) and secondary polyclonal anti-goat IgG peroxidase conjugate (0.65 x 10^{-3} µg/ml, Dako, Denmark).

3.2.8 Amyloid enhancing factor activity in AA-mL$_{dec}$

Two groups of five wild-type female C57BL/6 mice (Biological Services Unit, UCL) aged 12-15 weeks and weighing 23 to 26 g received an injection of 0.2 ml of AA-*m*L$_{dec}$ or AA-*m*L homogenates , followed by repeated subcutaneous injections of 10% w/v casein in 0.01 M carbonate buffer. Casein was given for 5 days per week from day 1 to 14. To evaluate amyloid load, a single intravenous tracer dose of ^{125}I-labeled serum amyloid P component (SAP) [198] was administered on day 23. Whole body retention of ^{125}I was assessed after 24 and

48h, and histological grading of Congo red stained formalin-fixed, wax-embedded tissues was performed [199,200].

3.2.9 Amyloidogenic Protein Perfusion

Healthy decellularised mice livers were perfused with human wild type (WT) β 2m protein resuspended in PBS or with the amyloidogenic variant D76N resuspended in PBS (0.25 mg/ml) for up to 72h at room temperature (RT). The mice liver scaffolds were washed with PBS for 30 minutes before perfusing the tissue with β 2m WT/D76M. To further characterize the protein structure after its interaction with ECM proteins, the outflow solution was collected at different time points (1h, 12h, 24h, 36h, 48h, 72h) and left at -20 ^{O}C. After 72h of perfusion, livers were rinsed with PBS for 30 min in order to remove proteins not specifically associated with the ECM and subsequently fixed in 10% formalin.

3.2.10 Electrophoresis under denaturing and reducing conditions

Samples were collected at 1, 12, 24, 48 and 72 hours respectively during liver perfusion with recombinant human wild type or D76N β2-microglobulin (0.24 mg/ml in phosphate-buffered saline, PBS, pH 7.4) followed by extensive rinse with PBS. 10 µl aliquots of each sample were analyzed by SDS-PAGE under reducing conditions using gradient 8-18% Excelgel™ precast gel (polycrylamide gel 245x110x0.5 mm, GE Healthcare). At the same time 10µl of starting material and rinses at 15 and 30 min respectively were analyzed alongside with 5µl of low molecular weight markers (GE Healthcare) containing bovine α-lactalbumin (14.4 kDa), soybean trypsin inhibitor (20.1 kDa), bovine carbonic anhydrase (30 kDa), chicken ovalbumin (45kDa), bovine serum albumin (66 kDa) and rabbit phosphorylase b (97kDa). The run was carried with operating voltage 600V, current 50mA and power 30W respectively for 1.5 hour. The gel was then stained with a solution of 0.2% Coomassie Brilliant Blue (Sigma-Aldrich) in 45% methanol-10% acetic acid and destained with a solution of methanol-acetic acid having the same concentration as above.

3.2.11 Mass spectrometric analysis

Mass spectrometric analysis was carried out on a Micromass Quattro II triple quadrupole mass spectrometer in the positive electrospray ionisation (ESI) mode. After removal of salts using micro gel filtration columns (Bio-Gel P6-DG, Bio-Rad) samples were vacuum dried and dissolved at a concentration of approximately 10-50pmol/µl in acetonitrile/water/formic acid (90:10:0;1 v/v/v) and introduced into the ion source through an infusion pump at 8µl/min. The main operating parameters were as follows: capillary voltage 3.2 kV; cone voltage 35V; HV lens 0.5kV; Low Mass Resolution 14.6; High Mass Resolution 14.9; scan speed 750u/s; acquisition time 1-5min. The instrument was calibrated from 700-1800 Da using horse heart myoglobin. Under these conditions proteins form adducts with multiple protons (M+Hn)n+ and generate a series of ions related by the function (M+nH+)/n, where M is the average molecular mass of the protein and n is the individual ion charge. Spectra were analysed using Masslynx software (v4) to generate a transformed spectrum showing the calculated molecular mass of the proteins.

3.2.12 Ethical approval

The study was ethically reviewed and approved by the UCL Royal Free Campus Ethics and Welfare Committee and the UK Home Office, and complied fully with European Directive 86/609/EEC.

3.3 Results

3.3.1 Perfusion-decellularization of normal and amyloidotic mice livers

The initial step was to evaluate the efficiency of mild (1 cycle) or prolonged (2 cycles) decellularisation protocols in removing cellular materials while preserving key ECM molecules of the native tissue. The decellularization protocol was characterised by the sequential perfusion of deionised water, sodium deoxycholate, and DNAse through the hepatic portal vein.

As shown in figure 3.1, following the initial step of the deionised water, the livers changed its natural red/brown colours into a paled feature and then turned transparent after treatment with sodium deoxycholate. Notably, vessels of different sizes were macroscopically recognised in the internal structure. After the DNase step, the main branches from the portal vein became more visible within the organ and all vessels became more defined, while the organ became more transparent.

Macroscopically there were no differences observed between cycle 1 and cycle 2.

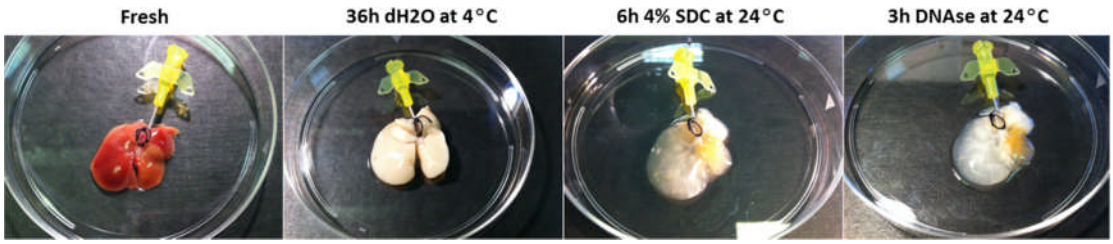

Figure 3.1. Macroscopic appearance of mouse liver during the process of decellularisation. Following dH2O addition, the livers became blanched, with SDC addition resulting in the livers becoming transparent. Following the DNase step, all vessels became more defined, while the organ became more transparent.

Histological staining and DNA quantification were performed in order to assess the efficiency of the decellularisation protocol. Cells removal was successfully achieved in both protocols as showed by H&E staining (figure 3.2). These findings were supported by DNA quantification (figure 3.3) showing removal of more than 80% of native DNA.

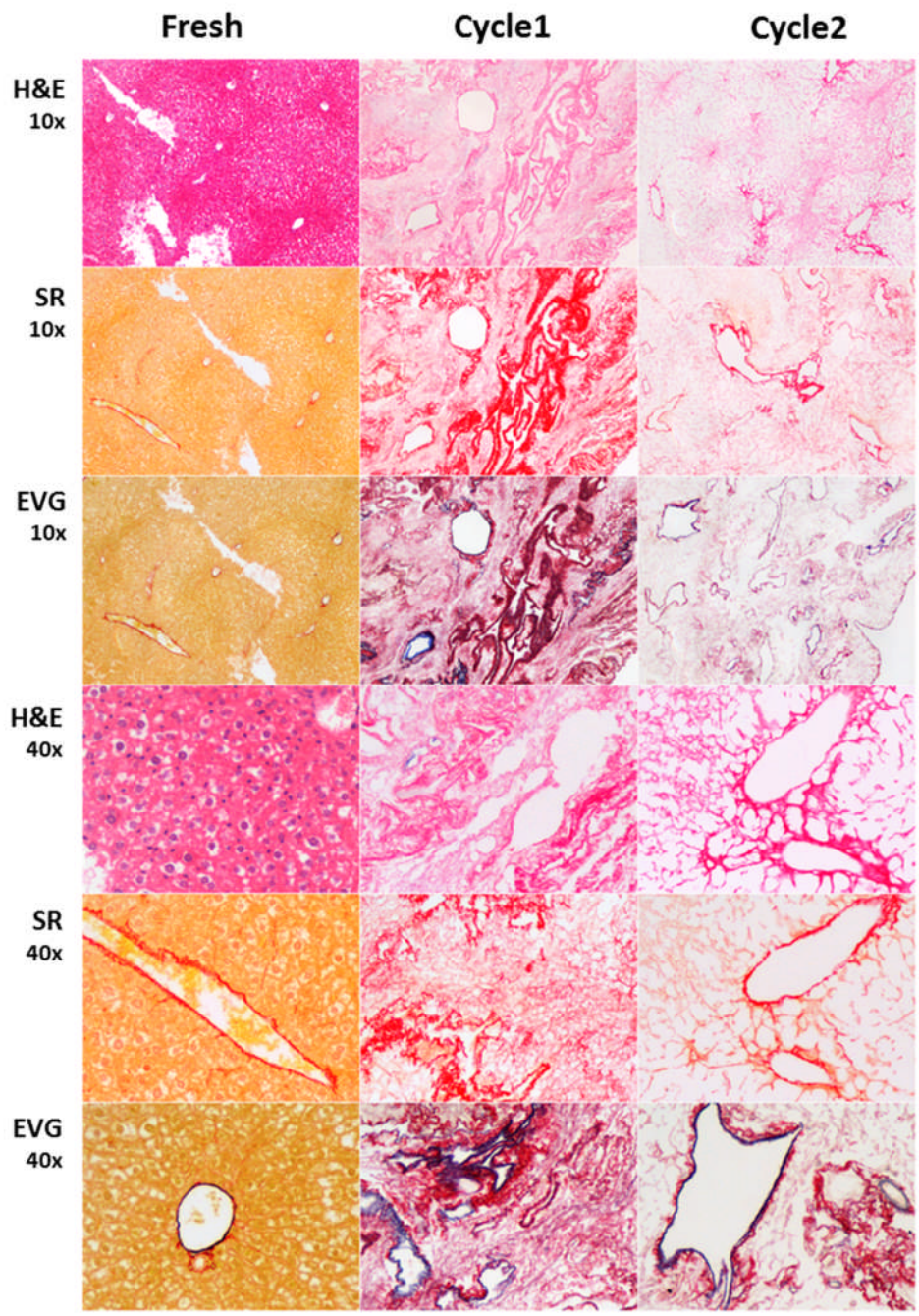

Figure 3.2. Histological characterisation of decellularised mouse liver tissues (1 cycle vs 2 cycles) in comparison with native tissue showing nuclei removal (H&E), collagen (SR) and elastin (EVG) preservation at both 1 and 2 cycle of decellularisation.

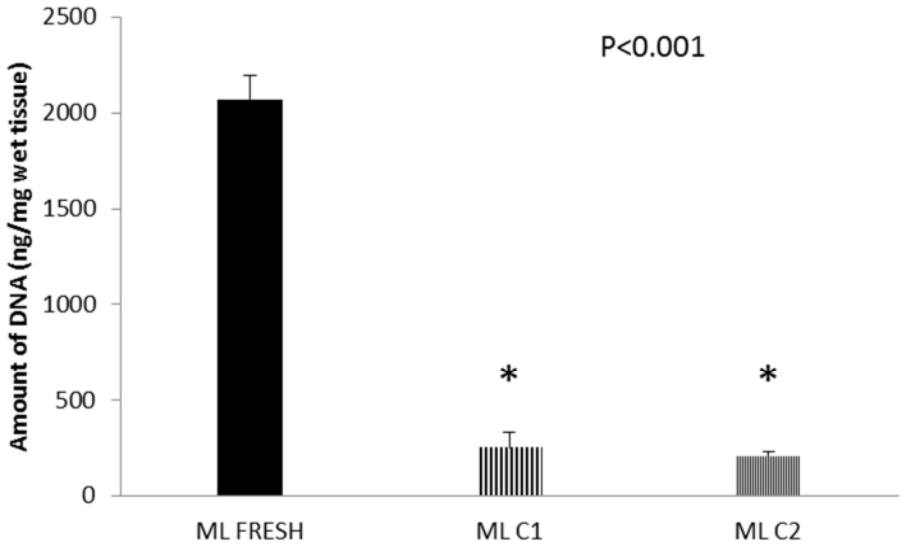

Figure 3.3. DNA quantification comparison between fresh healthy mouse liver and two cycles of decellularisation. The figure shows significant reduction of total DNA in both cases (<80%).

Next, the expression and distribution of proteoglycans was evaluated by Alcian Blue staining. As shown in figure 3.4, the amount of proteoglycans appeared reduced after 2 cycles of decellularisation. Therefore, because of the key role of proteoglycans in establishing interaction with amyloid proteins we decided to employ 1 cycle decellularisation protocol for further experiments.

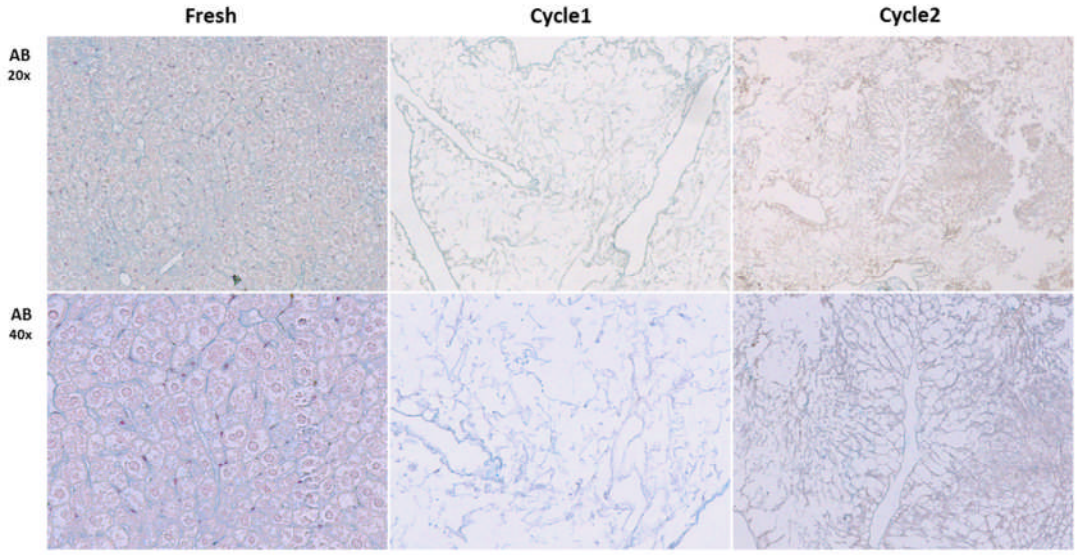

Figure 3.4. Alcian blue comparison between fresh healthy mouse liver and two cycles of decellularisation. The figure shows preservation of proteoglycans after 1 cycle of decellularisation.

After identifying the optimal protocol for developing whole liver mouse scaffold, we tested the capability of this protocol to decellularise transgenic mice livers overexpressing AA amyloid proteins.

As shown in figure 3.5 the macroscopic appearance after 46h perfusion (1 cycle) showed differences between decellularized healthy livers (H-*m*L_{dec}) and decellularized amyloidotic livers (AA-*m*L_{dec}). Indeed, the diseased-scaffold retained a dense-yellowish colour although the healthy scaffold turned translucent after the procedure.

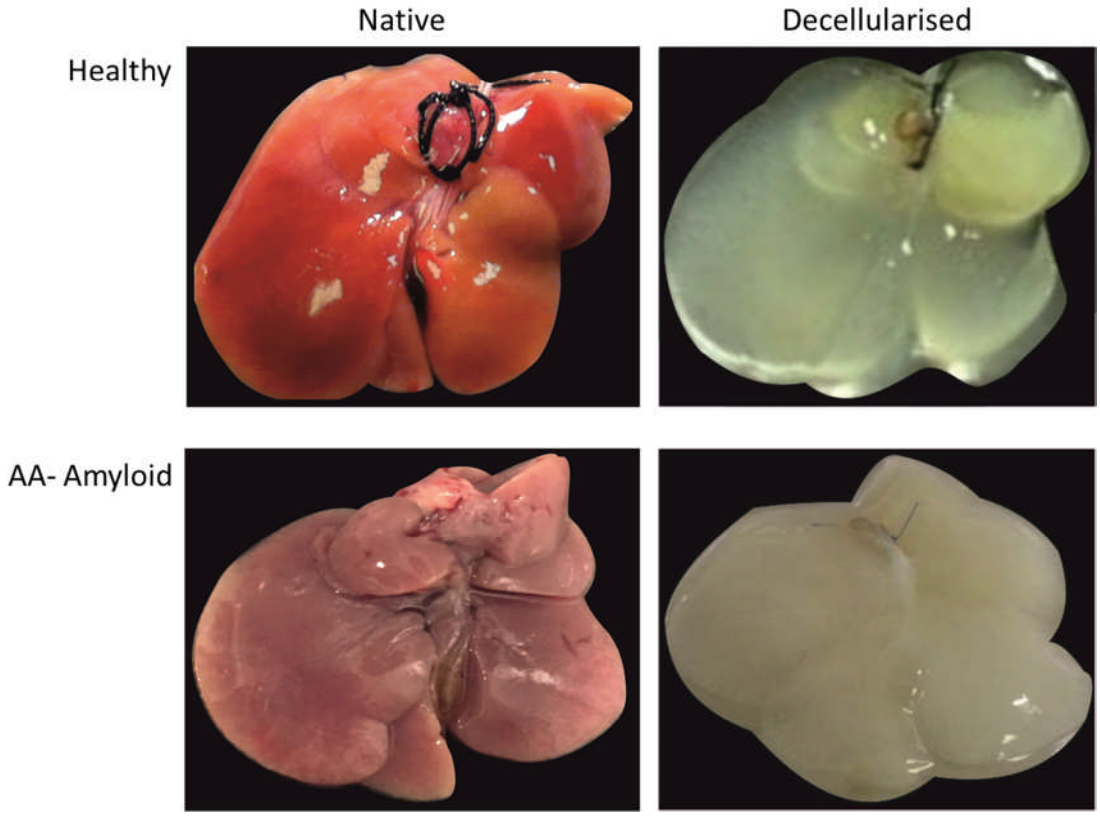

Figure 3.5. Macroscopic appearance of healthy and amyloid mice livers before and after decellularisation.

Thus, resultant scaffolds were characterised by histology and DNA quantification. H&E staining confirmed nuclei removal in both tissues (figure 3.6) while few nuclei were recognised in the diseased-scaffold. These findings were also supported by DNA quantification showing significant reduction in the total amount of DNA after decellularisation when scaffolds were compared with native tissues (figure 3.7). However, there were no significant differences in DNA content between healthy and amyloidotic decellularised livers (figure 3.8).

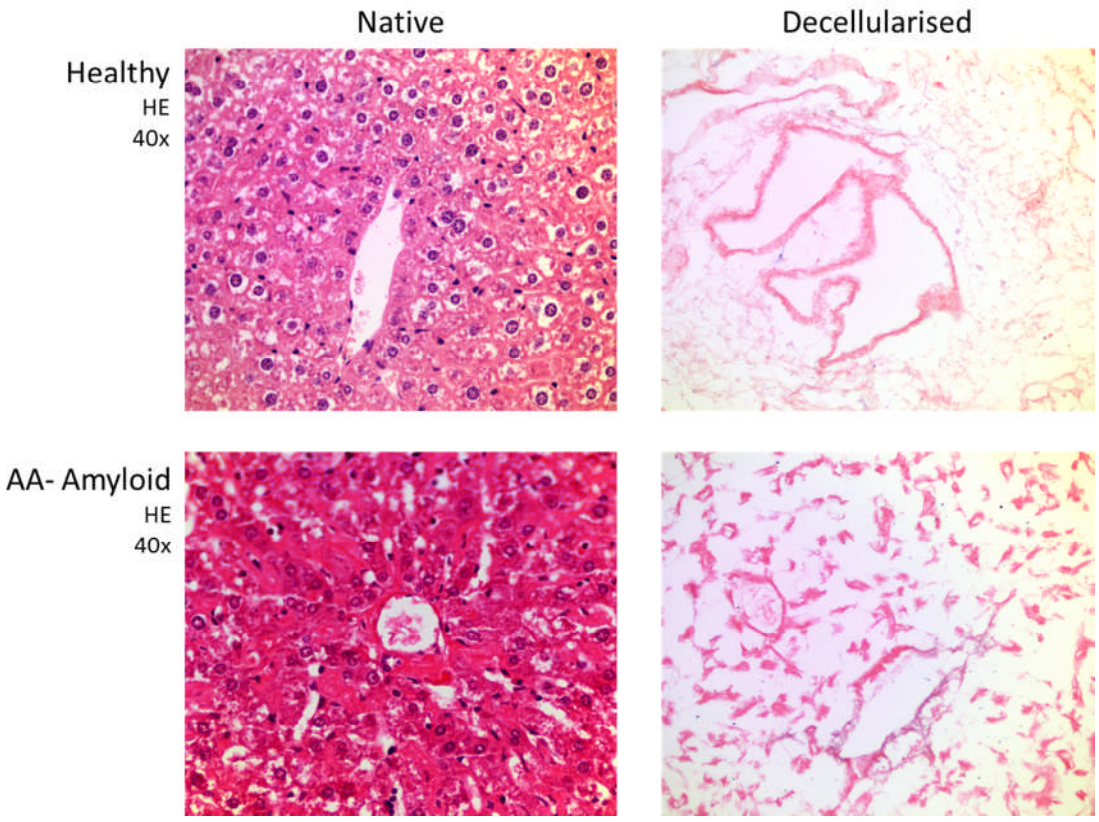

Figure 3.6. H&E comparison between healthy and AA livers before and after decellularisation. The figure shows showing nuceli removal (purple staining) after decellularisation in both tissues.

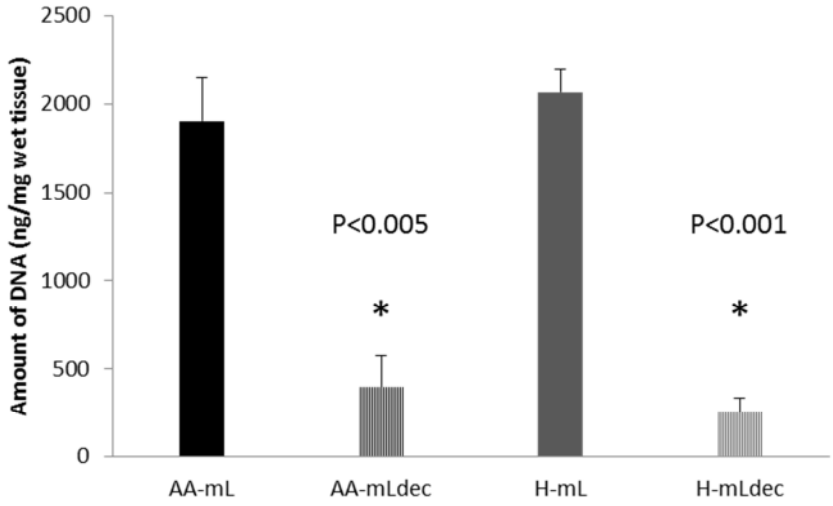

Figure 3.7. DNA quantification comparison between healthy and AA livers before and after decellularisation. The figure shows significant reduction in the total amount of DNA after decellularisation.

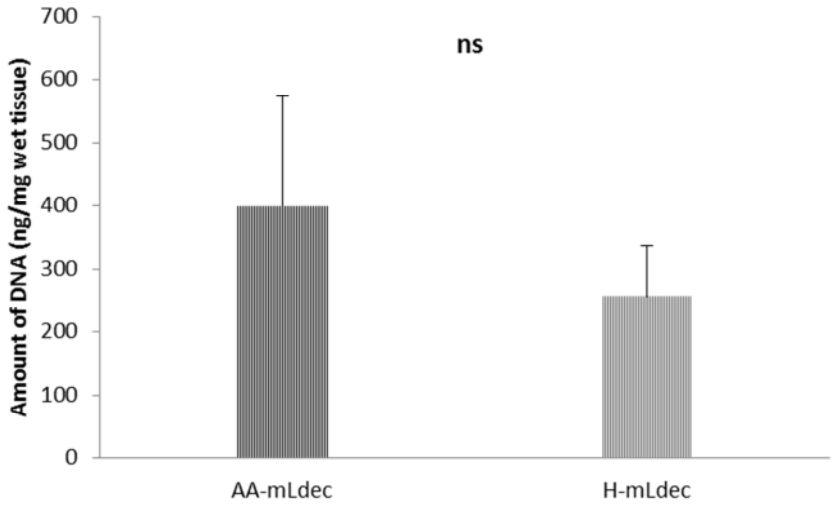

Figure 3.8. DNA quantification comparison between healthy and AA liver scaffolds. The figure shows no statistical differences in total DNA content between the two decellularised tissues.

Next, the preservation of the hepatic tissue architecture was evaluated by SR and EVG staining. As shown in figure 3.9 collagen filaments were maintained after decellularisation in both tissues. These filaments were mainly found into hepatic sinusoids and microvasculature while this latter was enriched by elastin filaments (figure 3.10).

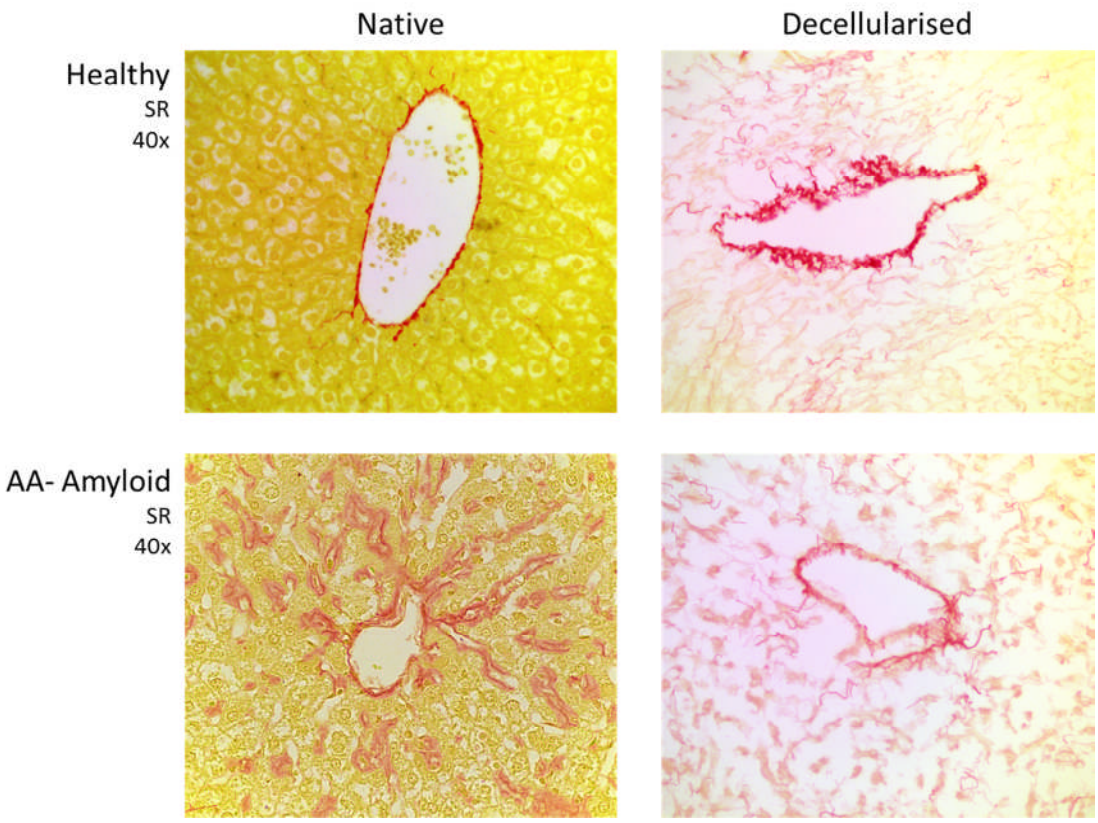

Figure 3.9. SR comparison between healthy and AA livers before and after decellulariastion. The figure shows preservation of collagen filaments after decellularisation in both healthy and amyloid tissues.

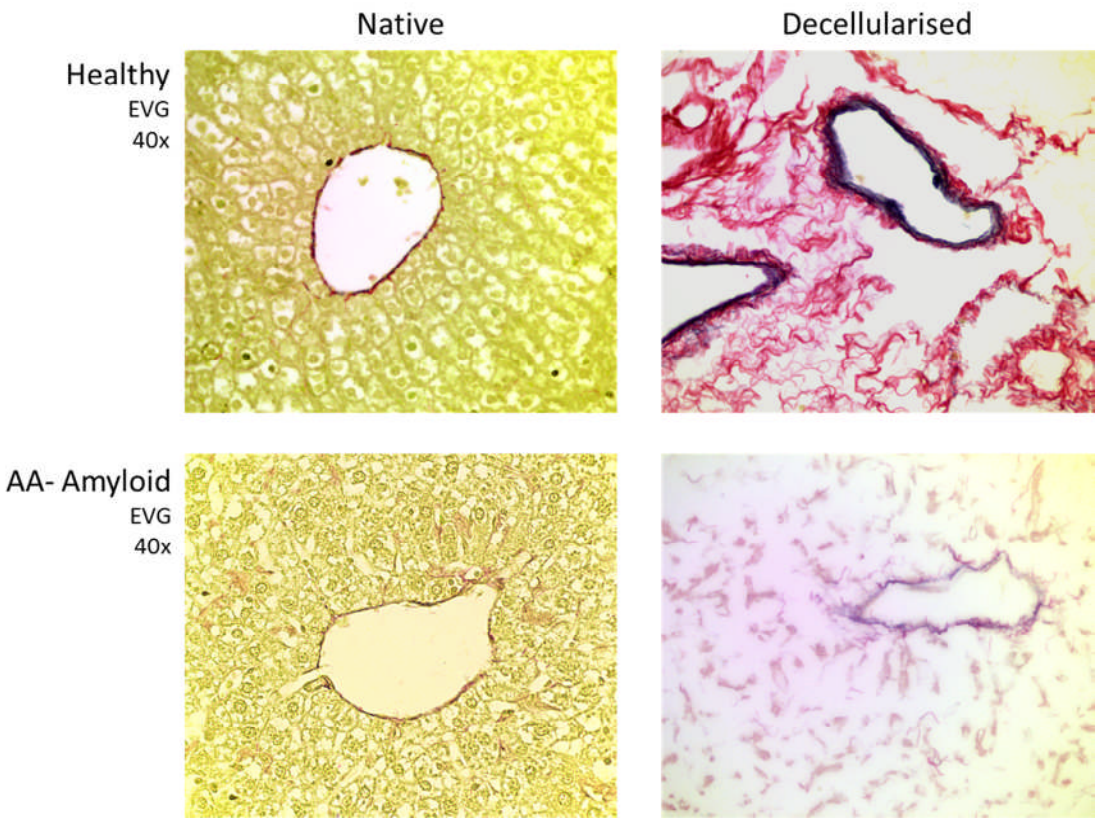

Figure 3.10. EVG comparison between healthy and AA livers before and after decellularisation. The figure shows preservation of elastin filaments (blue staining) after decellularisation in both healthy and amyloid tissues.

3.3.2 Amyloid is retained in the decellularized liver scaffold

The data described so far demonstrated the feasibility of developing whole mice liver scaffolds from both healthy and transgenic AA mice. Subsequently, sections from native and decellularised tissues were immunostained with SAA antibodies in order to investigate the impact of the decellularisation procedure on amyloid deposits. As shown in figure 3.11, decellularised amyloidotic tissues (AA-mLdec) were strongly positive when compared to sections of native amyloidotic livers (AA-mL) indicating an overemphatization of amyloid deposits after cell dissolution. As expected, decellularised healthy liver showed no positivity to the staining.

In addition, the specificity of the staining was assessed by performing immunohistochemistry without the primary antibody. As shown in figure 3.12

there was no cross-reactivity with the secondary antibody indicating specificity of the primary antibody to SAA.

Overall these data confirm the preservation of amyloid deposit after decellularisation and that amyloid was diffused within the acellular tissue as well as within the portal tracts and central veins.

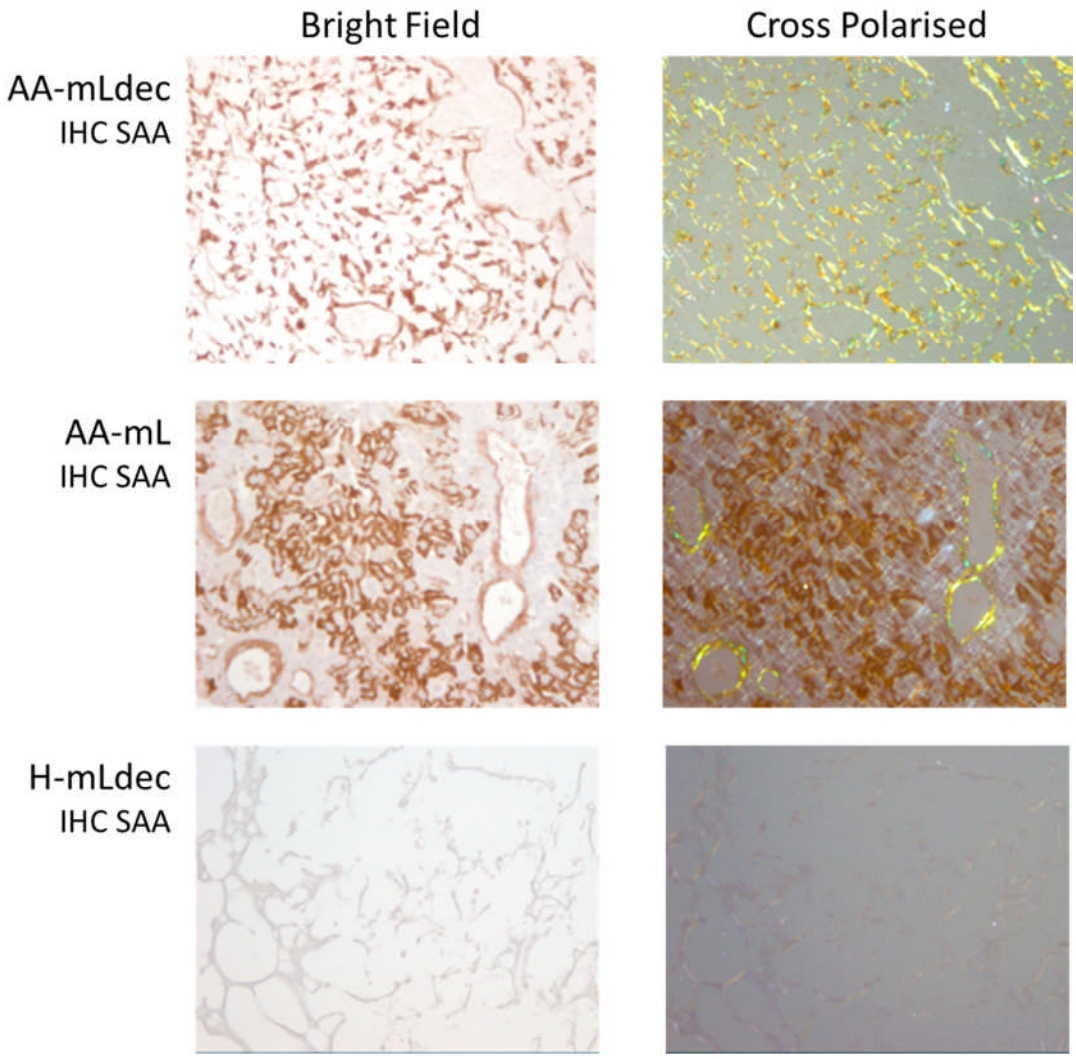

Figure 3.11. Immunohistochemistry for SAA with Congo Red, and viewed under bright field illumination (left panel) and with crossed polarised light (right panel) showing strong positivity through the whole parenchyma in decellularised amyloidotic mice (AA-mLdec), positivity within the portal tract of native amyloidotic mice (AA-mL) and absence of staining in decellularised healthy mouse (H-mLdec).

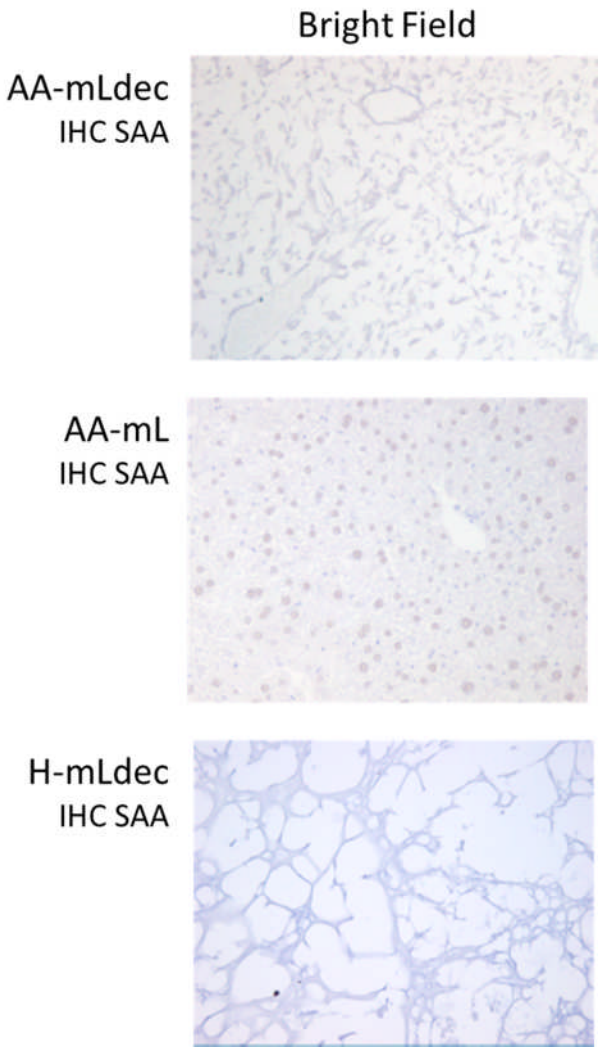

Figure 3.12. Immunohistochemistry control for all the three different conditions without primary antibody.

3.3.3 Ultrastructural characterization of decellularized mouse liver

The pioneering work of Bonsib and Plattner indicated that the resolution of the microscopic visualization of natural extracellular amyloid deposit can be increased by removing cellular materials from the native tissue[188] .

Therefore, scanning electron microscopy was employed to analyse the impact of the decellularisation procedure on the hepatic ultrastructure in both healthy and amyloidotic tissues (figure 3.13 and 3.14, respectively).

As shown in figure 3.13, there were no marked differences in terms of 3D architecture between healthy (H-mL) and amyloidotic native tissues (AA-mL). However, after decellularisation it was possible to appreciate key features of the

ECM ultrastructure. Indeed, the ECM filaments surrounding the hepatocytes-free space were highly organised in the decellularised healthy liver (figure 3.14, left panel). In contrast, the decellularised amyloidotic liver was characterised by a disorganised ECM network and most importantly the fibres associated to the acellular scaffold appeared thicker and enveloped by a spongy-like structure (figure 3.14, right panel) which was not present in the decellularised healthy liver.

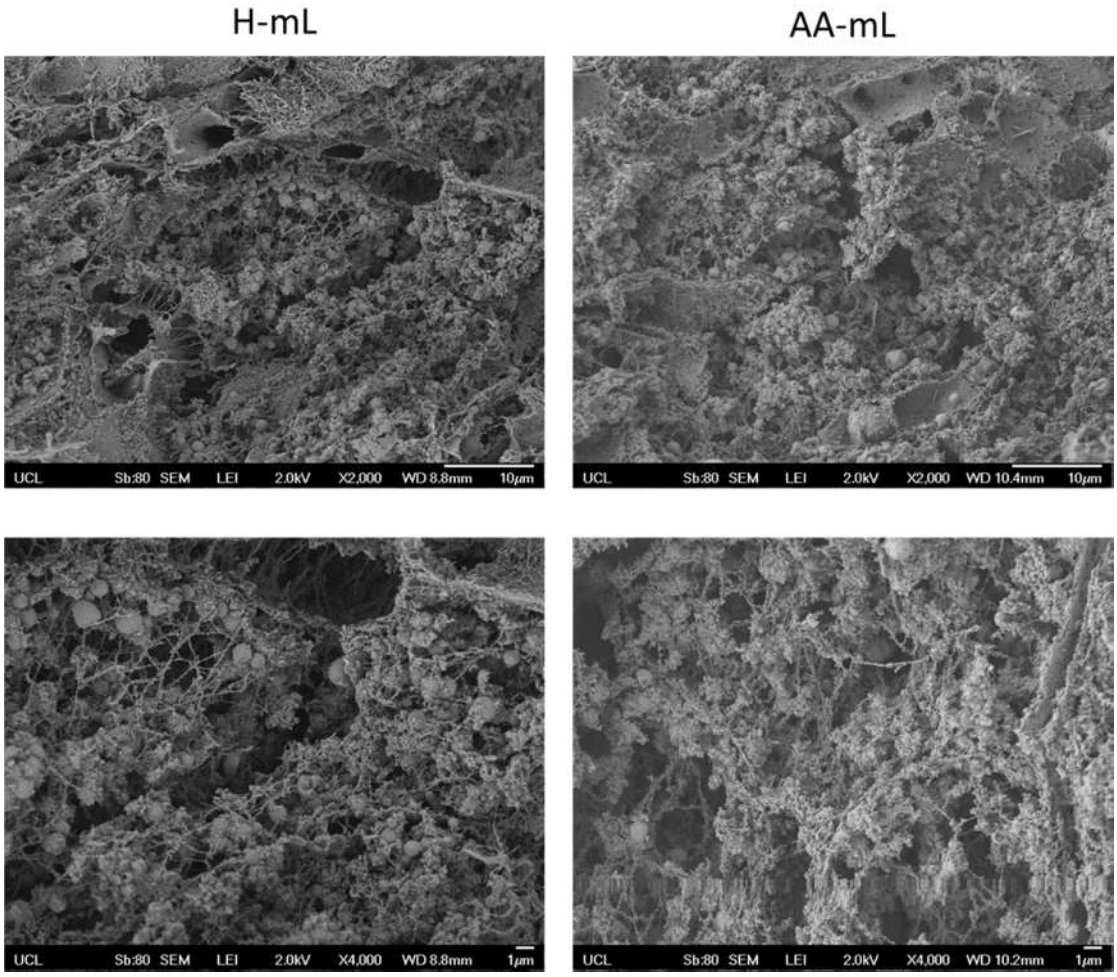

Figure 3.13. SEM images of native tissues from healthy and amyloidotic tissues (left and right panel, respectively) at two different maginification, 2000x (top panel) and 4000x (bottom panel).

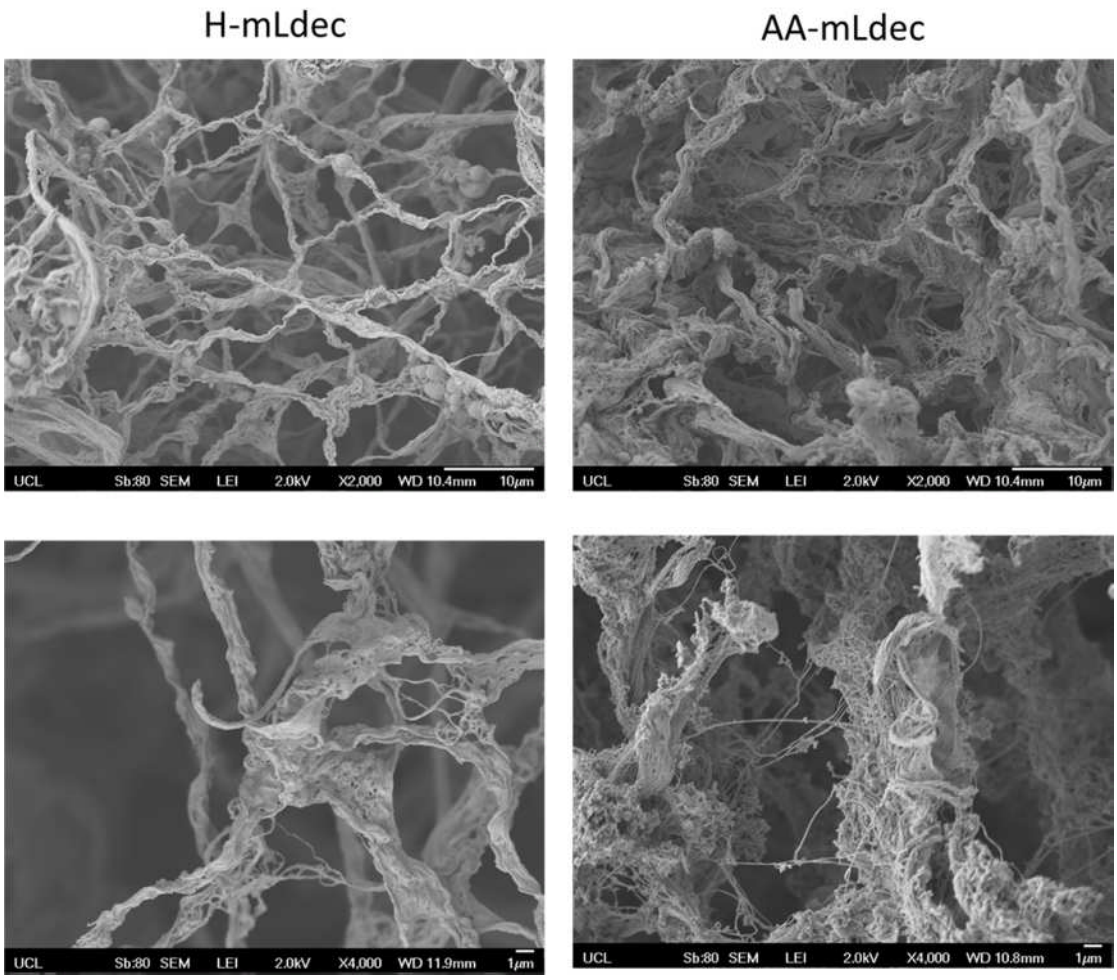

Figure 3.14. SEM images of decellularised tissues from healthy and amyloidotic tissues (left and right panel, respectively) at two different maginification, 2000x (top panel) and 4000x (bottom panel).

3.3.4 SAA fragments are the main components in AA-mL$_{dec}$

After confirming the preservation of amyloid deposit following the decellularisation process, we further investigated the structure and biological function of the amyloid deposit.

In order to assess the amino acid composition of the amyloidogenic proteins, homogenates samples from amyloidotic decellularised (AA-mLdec) and native (AA-mL) livers were run into 15% SDS-PAGE and stained by colloidal Coomassie blue. Interestingly, the double band corresponding to amyloid A protein (AA) [201] was detected only in the decellularised sample (figure 3.15). Next, the two main bands were *in situ* digested with trypsin and analysed by

MALDI-MS. This evaluation confirmed that both extracted peptides contained the 1-70 amino-terminal truncated portion of murine SAA_2 protein (Figure 3.16).

Lastly, homogenates from AA-mL (i) and AA-mLdec (ii) were analysed by western blot. As shown in figure 3.17, the detection of SAA2 fragments and full-length protein was detected in both homogenates.

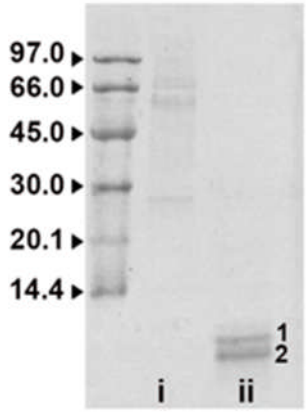

Figure 3.15. SDS-PAGE of homogenates from both AA-mL (i) and AA-mL (ii) in which a total of 2 µg of homogenates were separated in SDS 15% under reducing conditions. 1 and 2 indicates bands subjected to mass mapping analysis.

Position	Sequence	MH^+ (bands 1-2)
1-18	GFFSFIGEAFQGAGDMWR	2022.92
19-24	AYTDMK	728.33
25-39	EAGWK	590.29
34-38	YFHAR	693.35
39-46	GNYDAAQR	894.41
47-56	GPGGVWAAEK	971.49
62-70	ESFQEFFGR	1146.52

Figure 3.16. MALDI-MS of the double bands isolated from the SDS-PAGE gel. Tryptic peptides obtained by digestion of SDS-PAGE bands were analysed by MALDI-MS. MH^+ monoisotopic values are reported for each peptide.

3.3.5 Amyloid enhancing activity is preserved in AA-mL$_{dec}$

The amyloid enhancing factor (AEF) activity is a standard *in vivo* analysis in order to confirm the persistence of the supersecondary structure of amyloid fibrils and is a prerequisite to evaluate the capacity of natural amyloid to accelerate the fibrillar conversion of amyloidogenic protein precursors. Indeed, one injection of AA amyloid tissue in association with repeated casein administration accelerates amyloid deposition[197,202].

Therefore, we assessed the AEF activities of both AA-mL and AA-mLdec followed by casein administration (figure 3.18). As shown in figure 3.19, there were no differences in ^{125}I-labeled serum amyloid P component (^{125}I-SAP) retention and congo red staining of both spleen and liver (figure 3.20) [14,15].

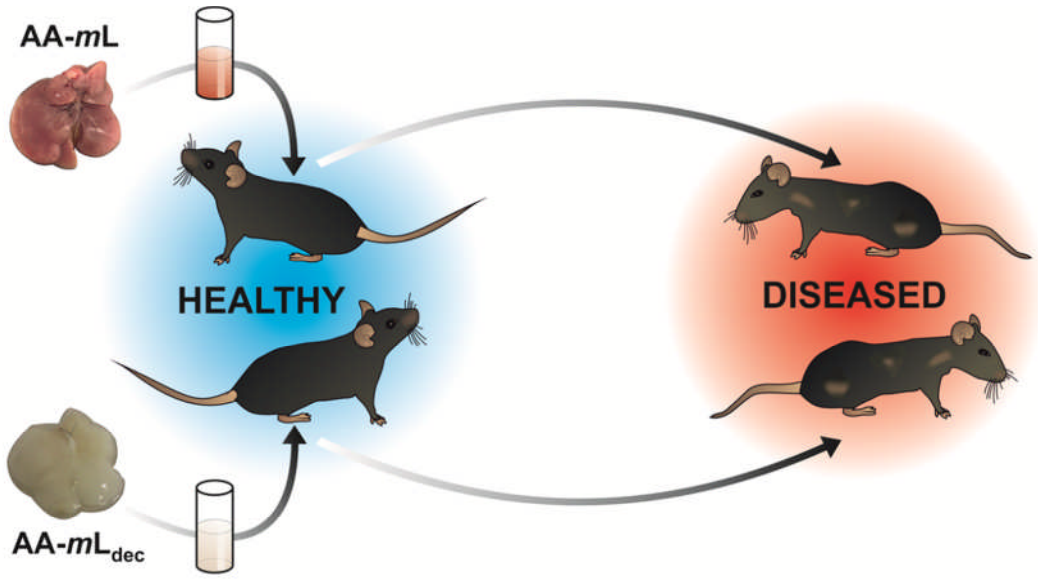

Figure 3.17. Schematic view of the amyloid enhancing factor (AEF) procedure.

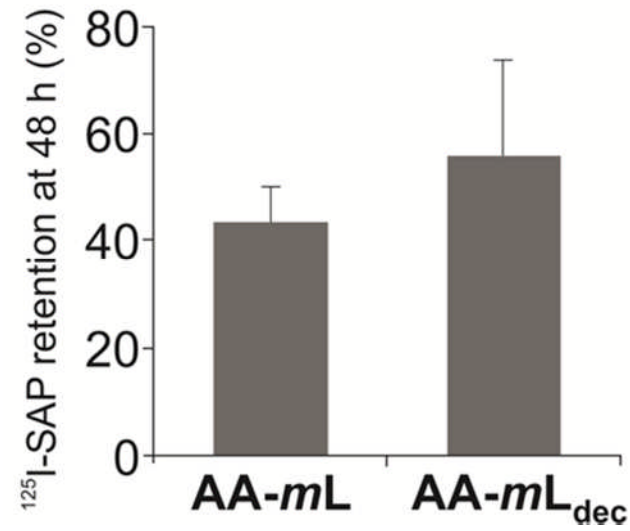

Figure 3.18. 125I-SAP retention at 48 hours. The figure shows no differences between native and decellularised amyloidotic livers.

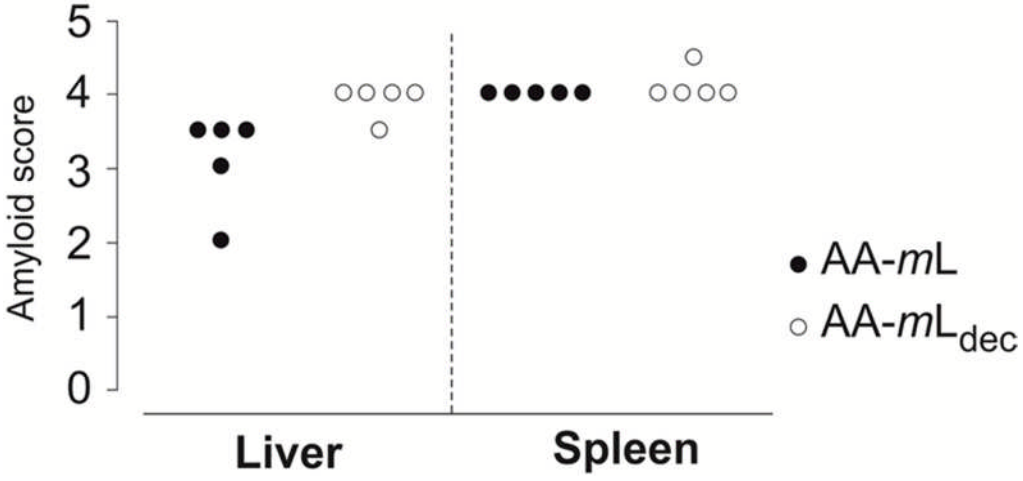

Figure 3.19. Amyloid score in vivo. The figure shows no differences between native and decellularised amyloidotic livers.

3.3.6 Interaction with liver ECM scaffold induces amyloidogenesis of D76N

Lastly, we explored the feasibility of developing a whole organ perfusion system for evaluating the 3D interaction between amyloid proteins (wild type β2m and pathological variant D76N) and hepatic ECM scaffold derived from healthy mouse liver.

The outflow collected from the perfused livers was analyzed by 15% acrylamide SDS-PAGE in order to define the protein structure after interacting with liver ECM scaffold. As shown in figure 3.21 the wild type β 2m protein still maintained its globular structure after 48h perfusion. Interestingly, the pathological variant D76N modify its globular structure generating several protein fragments after interacting with the bioactive liver ECM scaffold. The data generated by the 15% acrylamide SDS-PAGE were confirmed by employing ESI-MS (figure 3.22). In fact, based on the proteomic data, the outflow collected from the liver ECM scaffold perfused with the pathological protein variant contains a higher number of protein fragments when compared with the wild type.

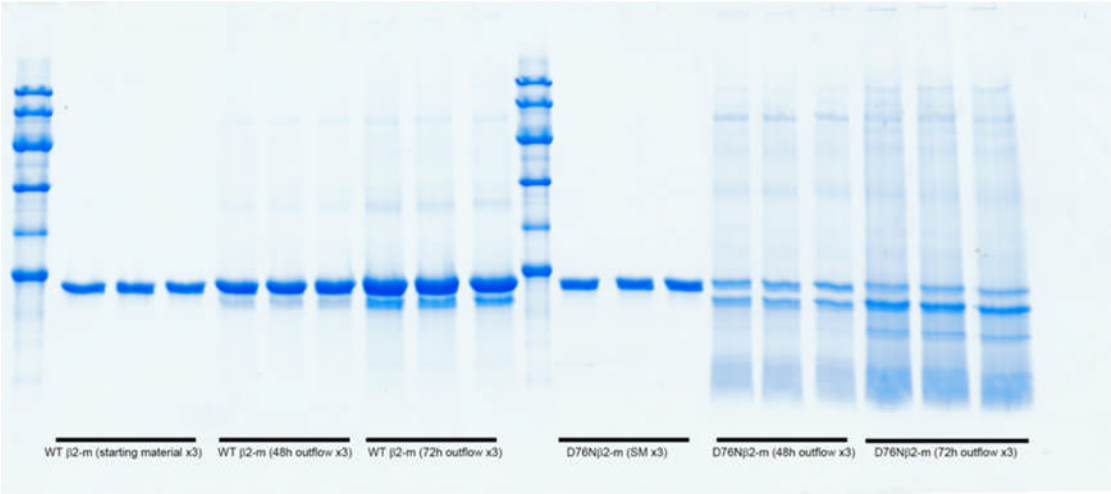

Figure 3.20. 15% SDS PAGE of perfusate from both WT and D76N. The figure indicates the presence of protein fragments in the perfusate from D76N.

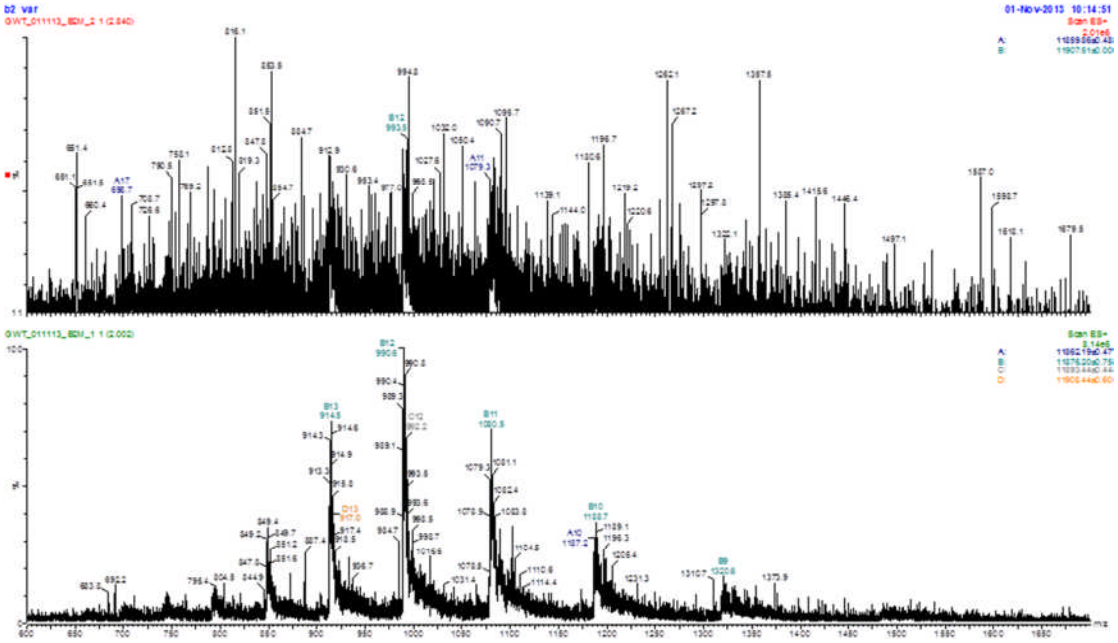

Figure 3.21. ESI-MS of perfusate from both D76N and WT (top and bottom, respectively) confirming the presence of protein fragmentation after perfusion with D76N.

After 72h of protein-perfusion, the livers were rinsed in PBS to remove all the proteins which were not stabilized to the ECM. Thus, the livers were analyzed by immunohistochemistry for the presence of human β 2m aggregates. Notably, the liver perfused with the D76N protein variant contained protein aggregates that were not present in the liver perfused with the wild type (figure 3.23). Therefore, the variant protein which causes amyloidosis in vivo reveals an inherent predisposition to aggregates after interacting with liver ECM scaffold.

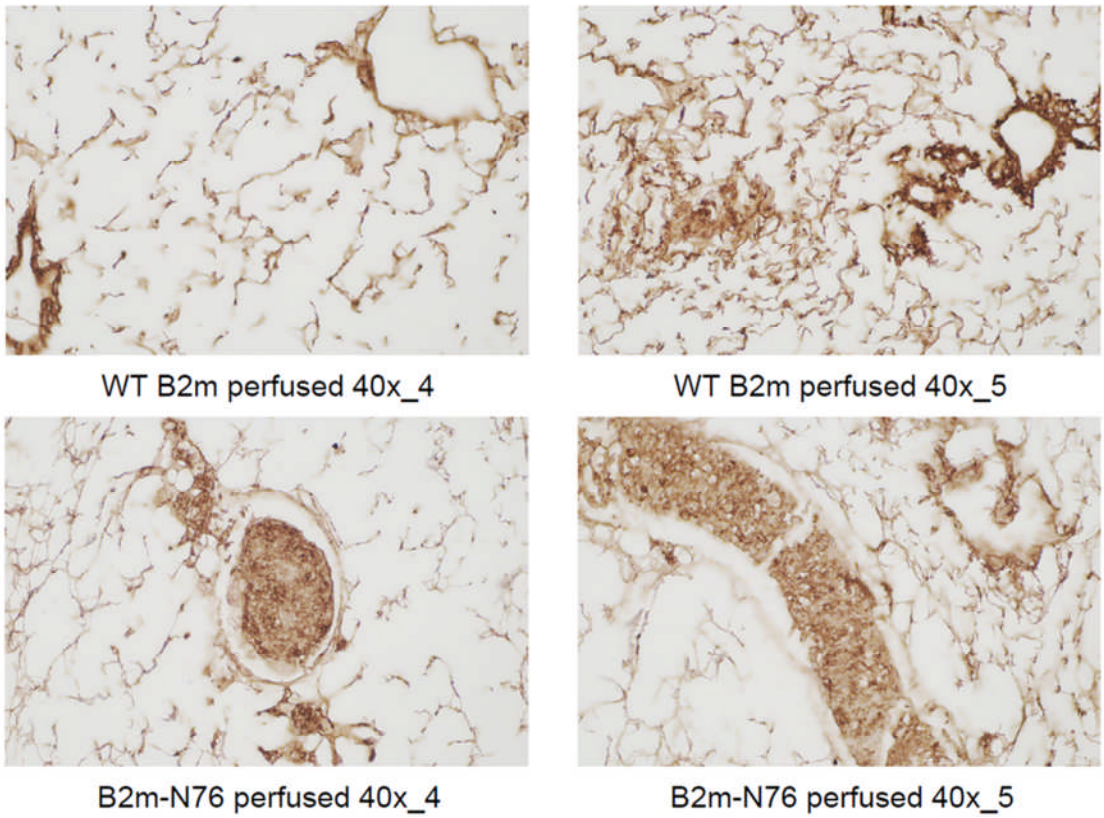

Figure 3.22. Immunohistochemistry for beta-2m of livers perfused with either WT protein or amyloid variant D76N (top and bottom, respectively). The figure shows protein-like aggregates in thei main vasculature structure of livers perfused with amyloid variant D76N.

3.4 Discussion

The results described in the first part of this chapter showed the possibility of decellularising amyloid liver while maintaining the diseased-associated features such amyloid deposit. Therefore, we showed that the structure and biological function of amyloid deposit were preserved after decellularisation.
The experimental model and preliminary results reported in the last part of this chapter emphasised the feasibility of developing a whole organ perfusion model in which amyloid proteins can be perfused through the natural vascular system of 3D-ECM scaffolds.

Interestingly, the process of cell removal highlighted key features of the hepatic ultrastructure that were not detected in the native tissue. This concept was firstly introduced by Bonsib and Plattner et al. in 1986 [188,203]. However, their findings revealed a globular structure covering the surface of ECM filaments suggesting that those structures were amyloid fibrils. Our data confirm that analysis of the 3D microstructure may be improved by removing cellular materials from the organ. However, the resultant scaffold generated through our protocol is characterised by spongy-like structure that affect the physiological arrangements of ECM network, mainly composed by fine filaments.
The differences between our protocol and previously published work can be explained by different methodologies employed for achieving tissue or organ decellularisation. Indeed, our decellularisation protocol was characterised by perfusion through the main vascular tree of mild decellularisation agents including SDC[194,204]. Thus, we propose that our mild protocol enables the identification of key ultrastructural features that were identified just after decellularisation of amyloid tissue. These findings were supported by protein analysis of tissue homogenates from both native and decellularised amyloid tissues revealing the presence of SAA fragments. Furthermore, homogenates from amyloidotic decellularised livers maintains their amyloid enhancing factor activity after injection in mice. Therefore, this confirmed that the decellularisation process preserves amyloid deposits while revealing key ultrastructural features without

altering the functional property of natural fibrils to prime amyloid growth and propagation.

These ultrastructural features emerging from SCAN microscopy suggest that biomechanical properties of amyloid tissue may be altered such as organ elasticity and fluid permeability of the extracellular space and thus explaining the increased hepatic tissue stiffness of patients with amyloidosis[205].

In addition, our mild decellularisation procedure maintained key ECM molecules involved in amyloid fibrillogenesis such as the abundant presence of glycosaminoglycans stained by Alcian Blue[206].

For this reason, we propose that the whole organ scaffold may be employed for the study of the interaction between amyloid and ECM proteins. Our preliminary results showed the feasibility of perfusing whole mouse liver scaffold with human wild type and pathogenic β2-m variant. It is worth noting that the β2-m variant and not the wild type after several passages into the liver scaffold revealed several proteolytic cleavages. The early cleavage occurred in the N-terminal strand of the protein that is known to become highly flexible in the early phases of amyloid conversion[207]. Therefore the decellularized scaffold not only maintains a native like 3D structure, but also some proteolytic enzymes are still fully active. We hypothesize that intrinsically unstable globular amyloidogenic proteins such as this b2-m variant (Asp76-Asn)[208,209] can become partially unfolded once exposed to the shear forces present in the perfused liver scaffold. The hydrophobic surface of ubiquitous fibrous proteins of ECM (i.e. collagen and elastin) provides a prominent contribution to the generation of the shear forces for the unfolding of globular proteins[207] and the proteins became highly susceptible to proteolytic cleavage[210] as well as to self aggregation. The tissue scaffolds obtained using the methodology herein proposed can become a unique tool for recapitulating in a biomimetic system the effect of biomechanical forces into two crucial pathogenetic steps of amyloidogenesis of globular proteins: selective proteolytic cleavage and self aggregation.

Chapter 4: Three dimensional human liver acellular scaffolds with preserved architecture and physiochemical properties for functional tissue engineering

4.1 Introduction

This chapter addresses the development of small scale human liver biological scaffolds in order to develop a natural material for *in vitro* hepatic tissue engineering. Data reported in this chapter have been incorporated into a patent (UK patent application n° 1513461.2 filed with UCL Business).

The development and functionalisation of biomaterials have been actively pursued to enable more effective applications of tissue engineering. In particular, the development of 3D-biological scaffolds, based on a natural extracellular matrix (ECM) protein structure, has been shown to provide a more physiological platform for cell engraftment and function[45,155]. Functionalised 3D biomaterials allow the study of cell/tissue biology in the presence of biochemical and biomechanical stimulants within the physiological spatio-temporal context[174,211]. In addition, the understanding of human physiological and pathophysiological conditions could be improved by employing appropriate 3D-ECM microenvironments reflecting the complexity of normal and diseased tissues [185,212-215].

The main challenge in liver tissue engineering is to recapitulate the complexity of human liver. The hepatic ECM is a complex network of macromolecules that not only provides cells with an extracellular scaffold but also plays an important role in the regulation of cellular functions[216,217]. Although biochemical signals are fundamental in the regulation of cell behaviour, including differentiation and motility, this is also markedly influenced by the surrounding mechanical environment, including structural topography and tissue stiffness[218-221]. Therefore, biomaterials should be able to reproduce the essential features of the physiological extracellular scaffold including tissue-specific ECM protein composition, 3D-microarchitecture, stiffness and pro-angiogenic properties in order to support cellular growth and maintenance of cell phenotypes.

As extensively detailed in the previous chapters of this thesis, decellularization is a process that removes cellular and immunogenic materials from tissues and organs while maintaining the mechanical and bioactive properties of the tissue[222]. This allows the optimal recellularization with organ-specific cell types leading to the development of engineered tissues and organs. Accordingly, major advances in the decellularization-recellularization technology have been achieved for the development of whole engineered organs due to their attractive application in the area of whole organ transplantation[45,155,223-226].

Despite the progress achieved in the development of whole organ scaffolds, no advancement has been reported for the decellularization of tissue sections. Importantly, the development of small scale acellular scaffolds could provide tissue-specific 3D-ECM platforms to be used as an alternative to standard 2D-cell cultures on artificial materials such as plastic. This will allow the introduction of *in vitro* experimental conditions closer to human physiology and pathology.

The main aim addressed in this chapter was to develop a novel methodology for improving the generation of small size 3D-ECM scaffold from sections of healthy human liver. This methodology, based on high g-force oscillation/high flow shear stress and markedly reduced processing time, represents an alternative to the established agitation-decellularization procedures so far reported[124,153] which are characterized by lengthy procedures and prolonged exposure to detergents leading to suboptimal decellularization.

Therefore, the next section of this chapter will describe the development and characterisation of small scale liver tissue scaffolds and the tissue engineering with different types of human hepatic cells.

4.2 Methods

4.2.1 Source of human livers

The work described in this paper was performed on healthy human livers that were harvested for transplantation and then judged unsuitable because of prolonged graft cold ischaemic time, the presence of extra-hepatic malignancy or other important extra-hepatic co-morbidities in donors or recipients. Livers included in this study were defined “healthy” because of the absence of any degree of tissue fibrosis and fat accumulation by histological analysis. The study was approved by the UCL Royal Free Biobank Ethical Review Committee (NRES Rec Reference: 11/WA/0077). Informed consent for research was confirmed via the NHSBT ODT organ retrieval pathway, and the project was also approved by the NHSBT Research Governance Committee. Donor livers were processed in accordance with the UCL Royal Free Biobank protocols under the Research Tissue Bank Human Tissue Act licence, prior to use in research. Human livers obtained at the Royal Free London Foundation Trust were coordinated, received and recorded by the UCL Tissue Access for Patient Benefit organisation (TAPb) which links research activities between UCL Royal Free Biobank, the Royal Free Trust and UCL. TAPb has full governance in place for this purpose which has involved NHSBT ODT pathway, the Human Tissue Authority licensing, and the local Trust / UCL Research offices.

4.2.2 Decellularization Protocols

Human livers (n=4) were perfused with PBS-1X allowing removal of blood and were stored at -80°C for at least 24h for the purposes of initial destruction of the various cellular compartments.

Afterwards, human livers were thawed at 4°C overnight and liver tissue cubes (LTCs) (n>200/liver) were obtained by scalpel cleavage (125mm^3) and stored at -80°C.

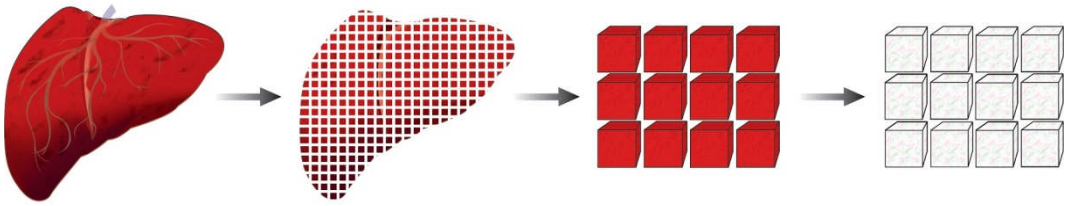

Figure 4.1. Schematic view of the process for developing human liver cubic scaffolds.

Initially liver cubes were thawed in a water bath at 37 °C for 1 hour, followed by the addition of 1.2 ml of 1% PBS for 15 minutes. Once thawed the cubes were transferred into 2ml safe-lock tubes (Eppendorf). A standardized 1.5 ml of each solution is added to its respective tube and different protocols were performed. The agitation regime for the decellularization of the LTC is shown in Table 4.1 and 4.2.

The reagent mixture was characterized by : 3%SDC, 0.5%SDS, 0.3%Triton X100, 4.3% NaCl, 0.0025% Trypsin/EDTA.

Step	Solution	Time (hours)
1	Deionised Water	24
2	PBS 1X	0.5
3	Reagent Mixture	5.5
4	PBS 1X	0.5
5	DNase Solution	3
6	PBS 1X	0.5
- Repeat steps (1-6) 4 times for protocols OS1 and MS - Repeat steps (1-6) 8 times for protocol OS2		

Table 4.1. Protocol description: orbital shaker (OS) and magnetic stirrer (MS).

Step	Solution	Time (minutes)	Repetitions
1	Deionised Water	2	5-20
2	Reagent Mixture	2	1
3	Reagent Mixture	4	2
4	Hypertonic Saline 9%	2	5
5	Deionised Water	2	5
6	Reagent Mixture	2	1
7	Reagent Mixture	4	2
8	PBS 1X	5	3
• If necessary, repeat steps 5-8			

Table 4.2. Protocol description: high g-force oscillation.

4.2.3 Histology and immunostaining analysis

Four μm sections were taken from formalin fixed paraffin embedded blocks and were de-waxed and rehydrated prior to staining (Xylene + IDA).

Histochemical stains: All sections were stained with Haematoxylin and Eosin (H&E) (Leica, Germany), Picro-Sirius Red (SR) (Hopkin & Williams) (BDH

Chemicals Ltd, Cellpath Ltd) and Miller's Elastic stain with a Picro-Sirius red counter stain (VWR, Leica, Raymond A Lamb).

Immunocytochemistry: sections to be stained with Collagen I, III, IV, fibronectin and laminin were incubated in 0.5% Trypsin/0.5% Chymotrypsin/1% Calcium Chloride (BDH) in Tris buffered saline pH 7.6 (TBS) for 30 minutes at 37 °C. Sections stained with alpha-fetoprotein (AFP), Factor VIII, TGFβ receptorCD31 were microwaved (640W) for 5 minutes, 10 minutes, 15 minutes and20 mins respectively and EPCAM and PDGFβ receptor pressure cooked for 3 minutes and 4 minutes respectively, in sodium citrate buffer (pH 6.0).

Slides were blocked in peroxidase blocking solution (Novocastra) for 5 minutes, washed in TBS for 5 mins and then incubated for 1 hour in the following primary antibodies; AFP (1:200; Dako, A0008), collagen I (1:200; Abcam, ab34710), collagen III (1:500; Abcam, ab7778), collagen IV (1:25; Dako, M0785), EPCAM (1:50; Leica Biosystems, NCL-ESA), (fibronectin (1:100; Millipore, MAB1937), laminin (1:200; Millipore, MAB1924), and Factor VIII (1:1000; Dako, A0082), PDGF-βR (1:50) and TGF-βR (1:50).

Primary antibodies were detected by usage of the Novolink^{TM} kit (Novocastra RE7280-K). Sections were dehydrated, cleared and mounted, and images were captured with an Axiocam IcC5.

4.2.4 DNA quantification

To assess total DNA content within native tissue and acellular matrices, the DNeasy Blood and Tissue kit was used according to the manufacturer's manual (Qiagen). Briefly, specimens were digested with Proteinase K overnight. DNA samples were purified using buffers provided by the company and measured spectrophotometrically (Nanodrop, Thermo Scientific, US). Optical densities at 260 nm and 280 nm were used to estimate the purity and yield of nucleic acids.

4.2.5 Collagen quantification

The collagen content of native tissue and decellularized tissue was quantified using the total collagen assay kit according to the manufacturer's manual (QuickZyme Biosciences, The Netherlands). Briefly, samples were hydrolyzed in 6M HCl at 95°C for 20 hours, the hydrolysates were mixed with a chromogen solution staining the hydroxyproline residues and color was developed at 60°C for

1 hour. The absorbance for each sample was determined at 555 nm using a FLUOstar Omega microplate reader (BMG labtech, Germany) and the collagen quantity was calculated by usage of a standard curve of pure collagen hydrolysates.

4.2.6 CAM assay

Chicken chorioallantoic membrane (CAM) angiogenic assay

CAM assay was performed to assess the angiogenic properties of the decellularized liver *in vivo*[177,227]. Briefly, fertilized chicken eggs (Henry Stewart and Co.) were incubated at 37°C at constant humidity. At day 3 of incubation 2 ml of albumin were aspirated from the acute end of the egg using a 21-G gauge needle attached to a 5 ml syringe. An oval window of approximately 3 cm in diameter was cut into the shell to reveal the embryo and CAM vessels. The window was sealed with Sellotape and the eggs were returned to the incubator for a further 5 days. At day 8 of incubation, 1 mm^3 ALTCs were placed on the CAM between branches of the blood vessels. Sterile inert mesh loaded with PBS or 200 ng/mL VEGF (Sigma) was used as a negative and positive control respectively. CAMs were examined daily until 7 days after placement of matrices, and photographed *in ovo* with a stereomicroscope equipped with a Camera System (Leica) to quantify the blood vessels surrounding the matrices. To assess angiogenesis, the number of blood vessels converging towards decellularized matrices was counted manually. Only blood vessels less than 10 mm in diameter were counted by blinded assessors (n = 4), with the mean of the counts being considered.

4.2.7 Scanning Electron Microscopy (SEM)

Samples were fixed in 2.5% glutaraldehyde in 0.1 M phosphate buffer and left for 24 hours at 4°C. Following washing with 0.1 M phosphate buffer, samples were cut into segments of approximately 1 cm length and cryoprotected in 25% sucrose, 10% glycerol in 0.05 M PBS (pH 7.4) for 2 hours, then fast frozen in Nitrogen slush and fractured at approximately -160°C. Next, samples were then placed back into the cryoprotectant at room temperature and allowed to thaw. After washing in 0.1 M phosphate buffer (pH 7.4), the material was fixed in 1% OsO4 / 0.1 M phosphate buffer (pH 7.3) at 3°C for 1½ hours and washed again in

0.1 M phosphate buffer (pH 7.4). After rinsing with dH_2O, specimens were dehydrated in a graded ethanol-water series to 100% ethanol, critical point dried using CO_2 and finally mounted on aluminum stubs using sticky carbon taps. The fractured material was mounted to present fractured surfaces across the parenchyma to the beam and coated with a thin layer of Au/Pd (approximately 2nm thick) using a Gatan ion beam coater. Images were recorded with a 7401 FEG scanning electron microscope (Jeol, USA).

4.2.8 Second harmonic generation (SHG) microscopy and autofluorescence imaging

Both native tissue and decellularized liver scaffolds were cryoprotected and sections were then set in a mold and covered in OCT cold embedding media and frozen. The OCT blocks containing the liver tissue/scaffolds were cryosectioned to a thickness of 20 μm and mounted on glass slides. Prior to measurements samples were thawed for 15 min in PBS.

All SHG images were obtained using a custom built multiphoton microscope incorporating an upright confocal microscope (SP5, Leica) and a mode-locked Ti:Sapphire Laser (Mai Tai, Newport Spectra-Physics). Images of the SHG signal from collagen I were collected using an 820 nm excitation with SHG signal obtained with a 414/46 nm bandpass filter and multiphoton autofluorescence signal obtained with a 525/40 nm bandpass filter. A 25X, 0.95 NA water-immersion objective (Leica) was used to deliver excitation signal and to collect the SHG emission signal from the sample. Images with a 600 μm x 600 μm field of view were obtained with 2048 pixel resolution and a line rate of 10Hz giving a pixel resolution of ~0.3μm with 3X averaging on each acquisition to reduce the effect of noise.

4.2.9 Atomic Force Microscopy (AFM)

AFM sample preparation:

Tissue samples for AFM measurement were prepared by taking tissue slices from a cube of liver tissue. Thick tissue slices were cut from the tissue cube using a scalpel, under liquid conditions and were kept in PBS at room temperature prior to attachment to a petri dish for analysis within 30 minutes. A slice of tissue

measuring 5mm x 2mm x 2mm was attached to a petri dish using two droplets of Cyanoacrylate adhesive, applied with a 10 µl pipette tip, placed at the extremities of the sample. After tissue slice attachment (1-2 min) the slice was immersed in PBS in order for the AFM measurements to be conducted within a 2 h time period. In the case of tissue scaffold samples, scaffold cubes were removed from storage in PBS at 4°C and excess liquid removed with a tissue prior to attachment. As previously described for the tissue slices, tissue scaffold cubes were attached to petri dishes with two droplets of adhesive at the extremities. After attachment (1-2 min) scaffolds were immersed in PBS and imaged within 2 h.

AFM Measurements:

Measurements of the tissue slices and scaffold cubes have been conducted on a JPK Nanowizard-1 (JPK Instruments) operating in force spectroscopy mode, mounted on an inverted optical microscope (IX-81, Olympus). AFM pyramidal cantilevers (MLCT, Bruker) with a spring constant of 0.07 N/m were used with a 35 µm glass bead attached to cantilever tip. Prior to measurements with the adapted cantilevers, their sensitivity was calculated by measuring the slope of force-distance curve in the AFM software on an empty region of the petri dish. For indentation tests on the sample, the cantilever was aligned over regions in the middle of the samples using the optical microscope. For each sample 30-50 force curves were acquired in 6-10 different 100 µm regions, this arrangement allowed force-curves to be acquired in locations at least 50-100 µm apart. Force-curve acquisition was carried out with an approach speed of 5µm/s and a maximum set force of 1.5 nN. Elastic modules were calculated from the force-distance curves by fitting the contact region of the approach curve with the Hertz contact model, using the AFM software.

4.2.10 Raman Spectroscopy

Raman spectra were collected using an inverted optical microscope (Eclipse Ti, Nikon) equipped with a 63x/ 1.2NA oil immersion objective. A 785 nm excitation laser, with the power of 50 mW at the sample, was used for excitation. The Raman back-scattered light was collected by the same objective and collimated towards an optical spectrometer (RiverD International) equipped with a deep-

depletion back-illuminated CCD (Andor Technology, UK). Raman maps were measured by raster-scanning the A movable stage (Prior Pro-scan ii) is equipped to allow spectral imaging. For measurements, the samples were placed on a 1 mm thick quarz window. Raman spectral mapping were recorded for tissue areas of 4 x 4 mm2 with a step size of 20 μm. The integration time at each pixel was 0.5 seconds. Auto-fluorescence images of the tissue samples were recorded for the same areas using a confocal scanner (C2, Nikon) integrated to the Raman microscope. The excitation was based on a laser at 405 nm (10mW) and detection in the range 450-480 nm.

4.2.11 Proteomics

Proteomic analysis was performed on 5μm slide of tissue (native and ALTC) previously fixed in formalin. The slide was removed by scalpel cleavage and it was analysed following the method of Rodriguez et al[228]. Following extraction into 10mM Tris/1mM EDTA/0.002% Zwittergen buffer (99 °C, 1.5 h) and sonication (1 h), samples were trypsinized (1.5 mg w/v) overnight at 37 °C and then reduced with dithiothreitol (50 μg) at 99 °C for 5 minutes. Digests were run on a nanoACQUITY™ UPLC system (Waters Ltd., Elstree, Hertfordshire, WD6 3SZ) coupled to an Orbitrap Velos Mass Spectrometer (Thermo Electron, Bremen, Germany. MS data files were analyzed using Mascot[229].

4.2.13 Cell Culture

The LX2 cell line is a well-established hepatic stellate cell line that was generated by spontaneous immortalization in low serum conditions[30]. Cells are cultured in Iscove's Modified DMEM supplemented with 2 mM/L glutamine, 0.1 mM/L non-essential amino acids, 1.0 mM/L sodium pyruvate and 20% Foetal Bovine Serum (FBS). HepG2 (ATCC® HTB-52™, VA, USA) are derived from human hepatoblastoma and were cultured in Eagle's Minimum Essential medium (EMEM), supplemented with Glutamax, 0.1 mM/L non-essential amino acids, 1.0 mM/L sodium pyruvate and 10% FBS. Human umbilical vein endothelial cells (HUVEC pooled; PromoCell) were cultured in low-serum (2% V/V) ECGM with supplemental mix (PromoCell) and used between passage 3 and 5. All cells were cultured under standard conditions in a humidified incubator with 5% CO_2 at

37°C. Every 3 days the complete culture medium was changed and sub-confluent cells were trypsinized and passaged at a split ratio 1:3.

4.2.14 Repopulation and culture of engineered human liver

Scaffolds were kept overnight in complete medium [day -1]. Cells were re-suspended at a concentration of 2 million cells per 50 µl ($2x10^6$/50µL) per scaffold (n≥12 per cell line). Cells were drawn up in a 0.5 ml insulin syringe and released drop by drop to finally cover the decellularized tissue. Seeded scaffolds were kept for 2.5h in a humidified environment at 37 °C with 5% CO_2 allowing cell attachment followed by addition of complete culture medium [day 0]. The culture medium was changed at day 1 and afterwards every 3 days. At days 7 and 14 (LX2, HepG2) and days 3 and 7 days (HUVEC) following seeding, the scaffolds were placed in 10% formaldehyde and assessed by histology and immunohistochemistry or fixed in 2.5% glutaraldehyde for SEM analysis. In addition, reseeded samples (quadruplicates) were snap frozen for further gene expression analysis.

4.2.15 RNA extraction and qRT-PCR.

Total RNA was extracted from 2D and 3D cultures using TRIzol reagent and RNeasy Universal Mini Kit (Qiagen). One microgram of total RNA was reverse transcribed with random primers and MultiScribe RT enzyme (Applied Biosystems, Paisley UK).

Gene expression was measured using Taqman gene expression assays with the Applied Biosystems® 7500 Real-Time PCR system (Supplementary Table 2).

Gene Name	Gene Abbreviation	Taqman Gene Assay No.
Glyceraldehyde-3-phosphate dehydrogenase	GAPDH	Hs02758991_g1
Collagen Type 1, alpha 1 chain	Col1A1	Hs00164004_m1
Transforming growth factor, beta 1	TGFβ1	Hs00998133_m1
Lysyl oxidase	LOX	Hs00942480_m1
Interleukin 8	IL-8	Hs00174103_m1
Integrin, alpha 6	ITGA6	Hs01041011_m1
Albumin	ALB	Hs00609411_m1
UDP glucuronosyltransferase 1 polypeptide A1	UGT1A1	Hs02511055_s1
Cytochrome P450 1A2	CYP1A2	Hs00167927_m1

Table 4.3. RT-PCR probes list.

4.2.16 Statistical analyses.

Results were expressed as mean±s.d. All data was analysed with ANOVA or Student's t-test. Two-tailed p values less than 0.05 were considered statistically significant. Expression levels for each gene were calculated using the delta Ct method[230] and normalized to the ones of GAPDH as reference gene. Graphs depict averages ± SEM of the relative gene expression data (n=3 or 4/group). Statistical analysis was performed with two-way ANOVA with Bonferroni's multiple comparisons test, using Prism GraphPad software.

4.3 Results

4.3.1 Optimization of the agitation-decellularization procedure of human acellular liver tissue cubes

The procedure was carried out by employing a stepwise protocol using increasing g-force intensities in order to remove immunogenic cellular materials whilst preserving ECM proteins as well as reducing the processing time and exposure to detergents. Therefore, the first step was to define the g-force value to be employed during agitation-decellularization and then apply this value consistently in the different protocols.

4.3.1.1 Determining G- force

The agitation systems were characterized by different agitation speeds defined by different g-force values. The g-force, which refers to the relative centrifuge force (RCF), is expressed as $\mathrm{RCF} = 1.118 * 10^5 * \mathrm{r} * (\mathrm{rpm})^2$ and was adopted to estimate the g-force value employed in previously published protocols using either orbital shaker or magnetic stirrer [133,140,142].

The novel system that we planned to use for decellularizing biological tissue considers a tissue sample undergoing harmonic motion with frequency f Hz and amplitude Û m and assuming it starts at zero displacement (i.e x=0 and t=0) will occupy the position $x = \hat{U}sin(f * 2 * \pi * t)$ (considering the difference in density between the tissue and it surrounding solution is negligible). Furthermore, a particle (or tissue in this case) which moves under simple harmonic motion will be represented by the equation $x'' = -w2x$, where $w = 2 * pi * f$. Reformulating these equation according to Newton second law, Force (F) equals mass (m) multiplied by acceleration (a) [F=ma], results in the equation $F = -m[(2 * \pi * f)2] * \hat{U}sin(f * 2 * \pi * t)$. This is extremised when |sin|=1. Therefore, it will be at its maximum/minimum when $F = +/-\hat{U}m[2 * \pi * f)2]$. Finally by dividing the equation by the force experienced by gravity (mg), the equation for $\mathrm{g}-force = (\hat{U}/g) * [(2 * pi * f)2]$.

4.3.1.2 Protocol optimization.

Healthy human LTCs were employed for optimizing the protocol of agitation decellularization (Figure 4.2). Initial experiments illustrated in Figure 4.3 and 4.4 employed low g-force intensity (0.4g). After 8 (Figure 4.3) and 16 (Figure 4.4) days of agitation with an orbital shaker (protocol OS1 or OS8 and OS2 or OS16), the resultant tissue appeared macroscopically brownish indicating a non-complete tissue decellularization. Histological examination (Hematoxylin and Eosin (H&E) and Sirius Red (SR) revealed the presence of cellular materials within the tissue (Figure 4.3, 4.4). Although, DNA quantification showed a significant reduction in the total amount of DNA after the procedure ($p<0.001$; Figure 4.6) this was still above the standard threshold of 50ng/mg of tissue[222] .

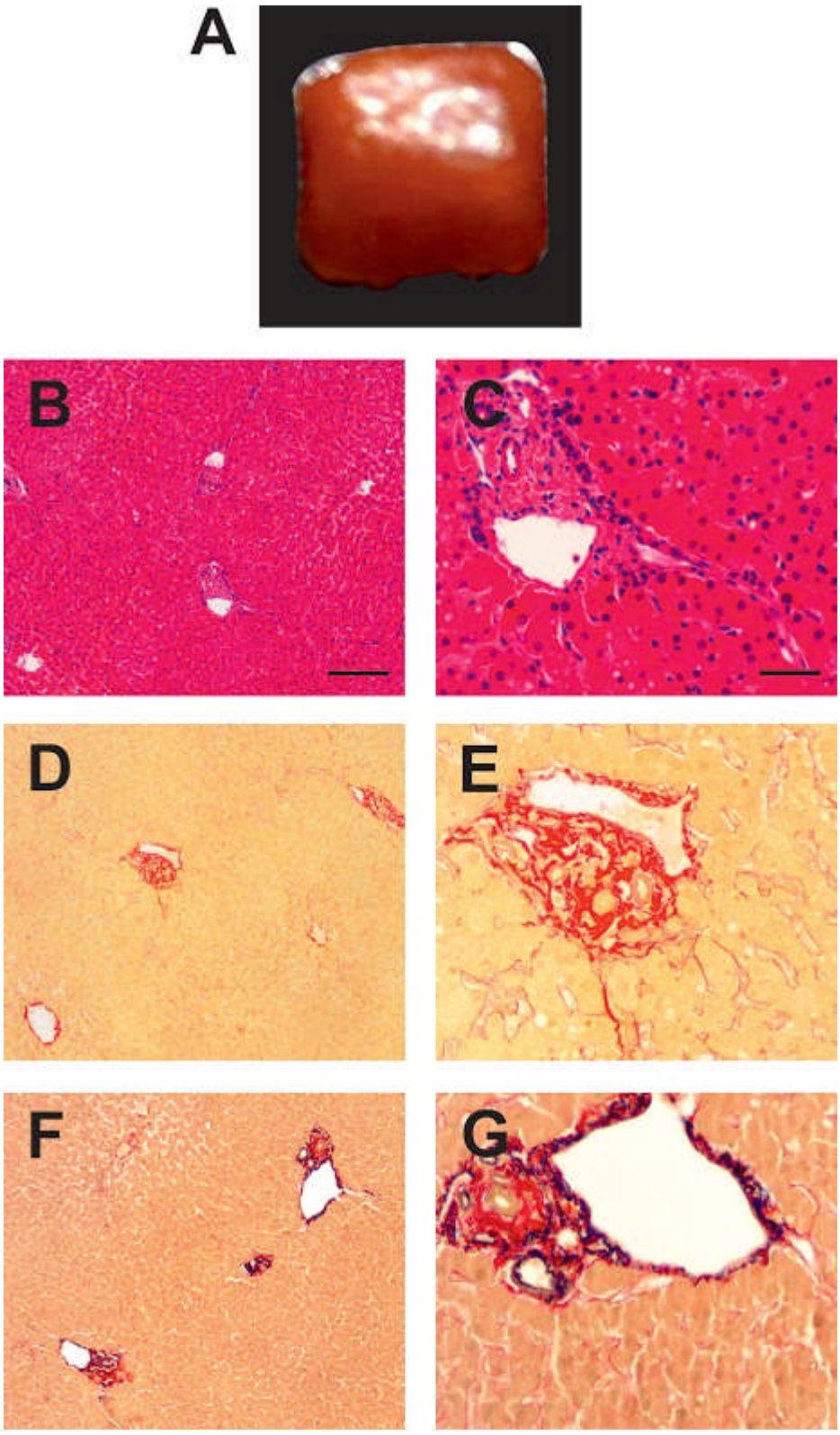

Figure 4.2. Histological characterization of native liver cubes. Macroscopic appearance of native liver (A) and histological characterization confirming absence of both fat deposition (B,C) and fibrosis (D-G). Scale bar B,D,F=200 μm and C,E,G = 50 μm.

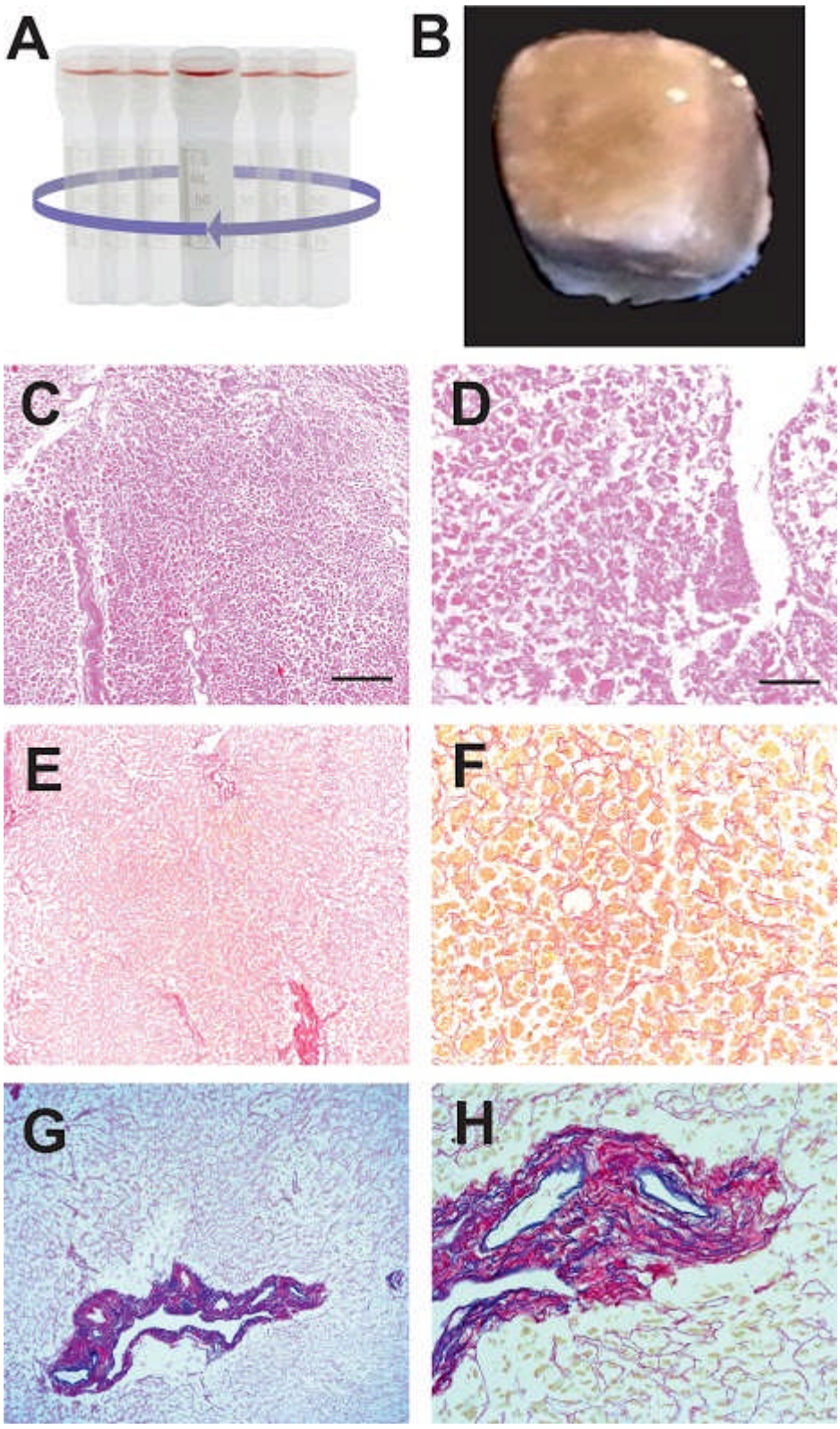

Figure 4.3. Histological characterization of orbital shaker protocol-1. Schematic view of the sample movement (A). Macroscopic appearance and histological analysis after decellularisation using an orbital shaker after 8 days (B), showing elimination of nuclear material (blue; H&E, C,D) and preservation of elastin (purple; EVG, G,H) but failure to eliminate cellular material (yellow; SR, E,F). Scale bar C,E,G,=200 μm and D,F,H= 50 μm.

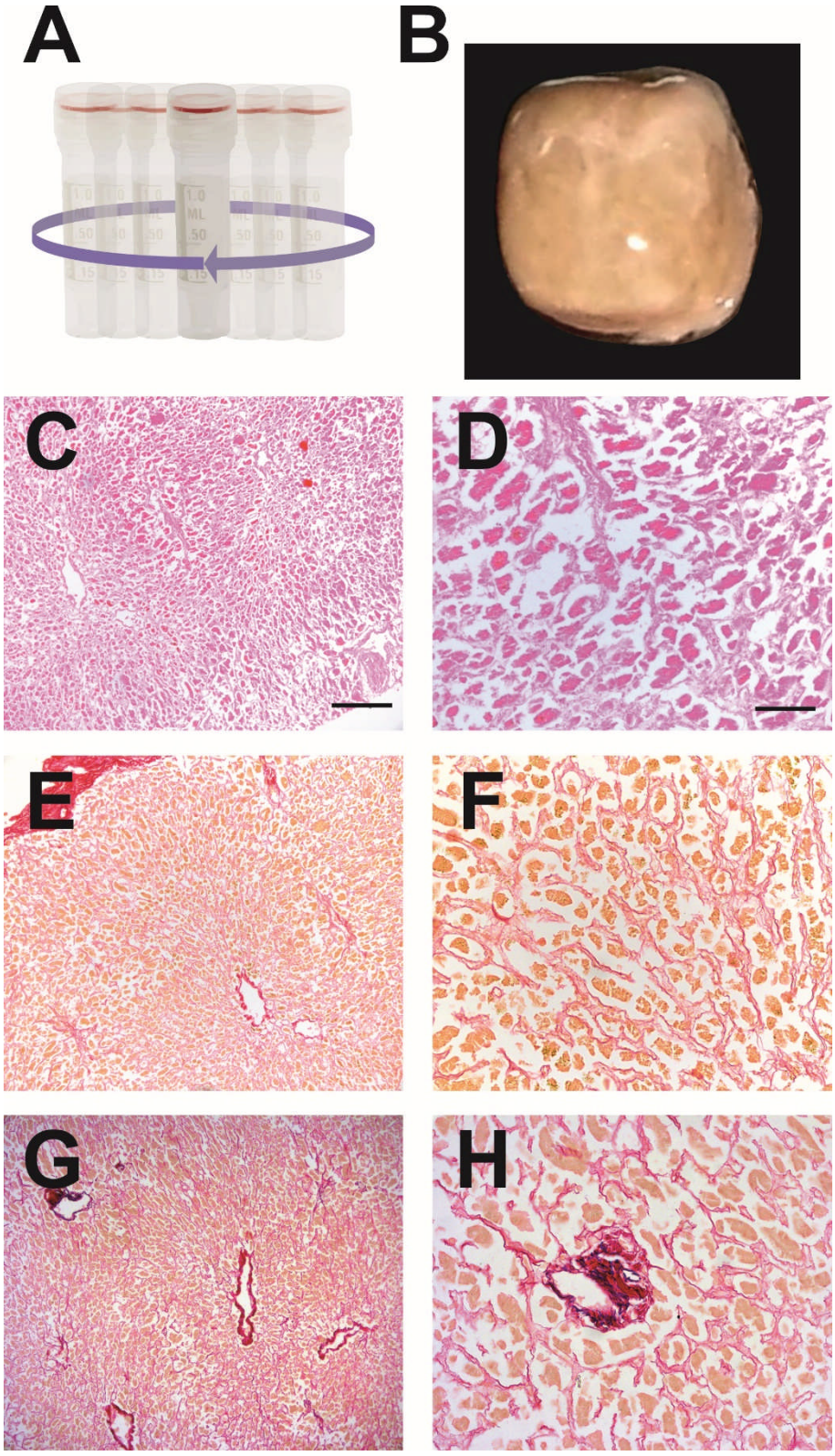

Figure 4.4. Histological characterization of orbital shaker protocol-2. Schematic view of the sample movement (A). Macroscopic appearance and histological analysis after decellularization using an orbital shaker after 16 days (B), showing elimination of nuclear material (blue; H&E, C,D) and preservation of elastin (purple; EVG, G,H) but failure to eliminate cellular material (yellow; SR, E,F). Scale bar C,E,G,=200 μm and D,F,H= 50 μm.

Subsequently, the g-force was increased up to 5-9g obtained by agitating the tissue with a magnetic stirrer (protocol MS1). After 8 days of agitation the tissue turned translucent (Figure 4.5B) and histological staining confirmed preservation of collagen and elastin filaments, while nuclear materials were removed. This latter finding was confirmed by DNA quantification which showed significant reduction of DNA ($p<0.001$) and the amount of DNA was slightly below 50ng/mg (Figure 4.6).

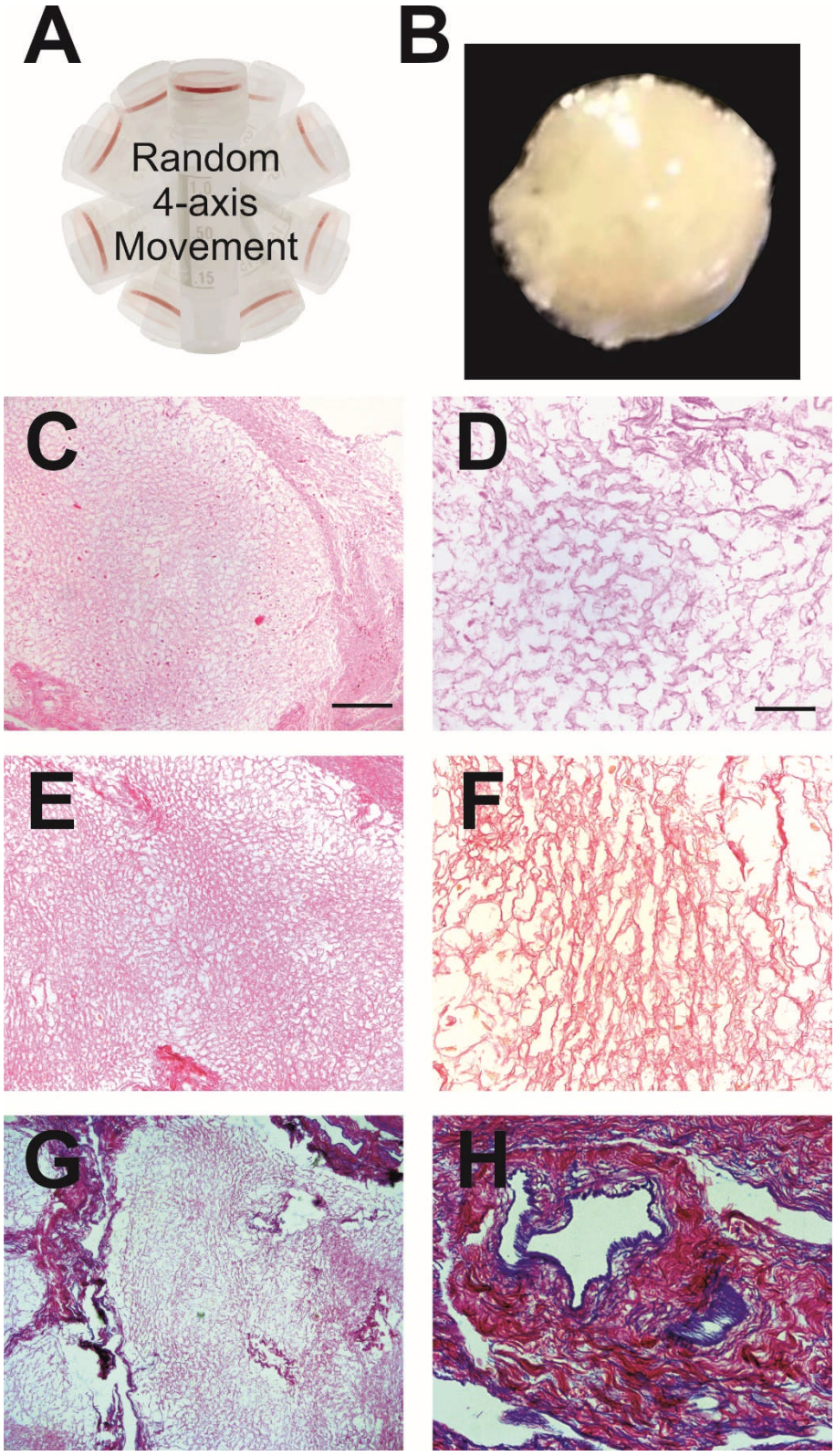

Figure 4.5. Histological characterization of magnetic stirrer protocol. Schematic view of the sample movement (A). Macroscopic appearance and histological images of decellularized liver cubes using a magnetic stirrer after 8 days, showing complete elimination of nuclear (blue; H&E, C,D) and cellular material (yellow; SR, E,F), and preservation of elastin (purple; EVG, G,H). Scale bar C,E,G,=200 μm and D,F,H= 50 μm.

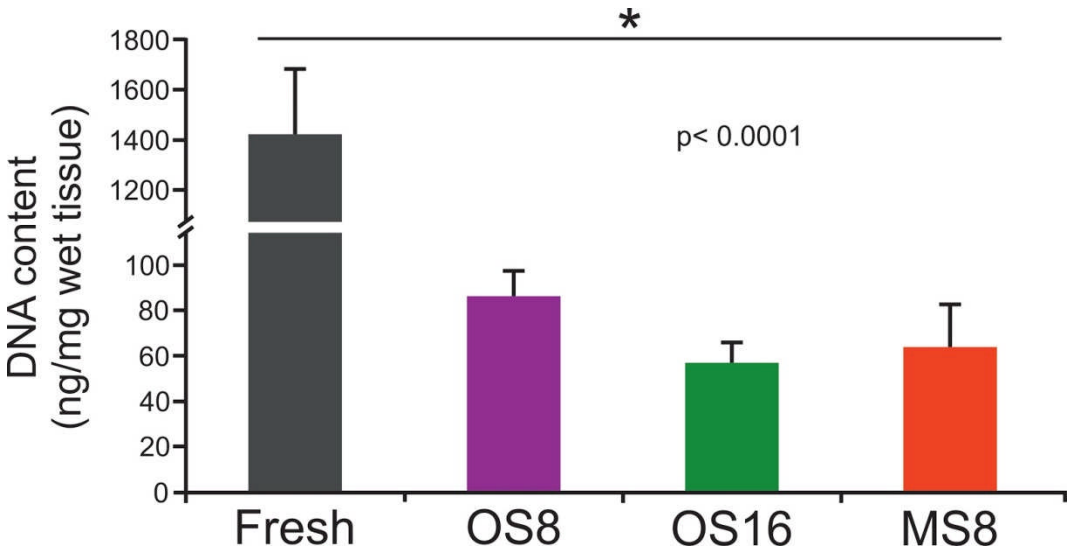

Figure 4.6. DNA quantification comparison between native liver and decellularisation protocols. The figure shows significant ($p<0.0001$) elimination of DNA in all decellularization protocols, although all protocols were above the desired quantity of 50ng/mg.

Lastly, the applied g-force was further increased up to 45g in order to minimize the time of exposure to detergents and to enhance the distribution of reagents/solution within the tissue. Remarkably, the LTCs turned translucent in just three hours (Figure 4.7A) in comparison to native tissue (Figure 4.2A). H&E staining confirmed complete removal of nuclear materials (Figure 4.7 B,C) while collagen and elastin filaments were preserved in the acellular liver tissue cube (ALTC) as showed by SR and Elastin Van Gieson (EVG) staining, respectively (Figure 4.7 D-G). Indeed, nuclei removal was confirmed by DNA quantification showing a more evident reduction of the total amount of DNA compared previously described protocols ($p<0.001$) (Figure 4.8 A). Collagen content relative to wet weight was increased ($p<0.01$; Figure 4.8 B). These observations suggested that by employing high flow shear stress it is possible to obtain, in a significant reduced processing time, an ALTC with preserved collagen and elastin filaments while cellular material was successfully removed.

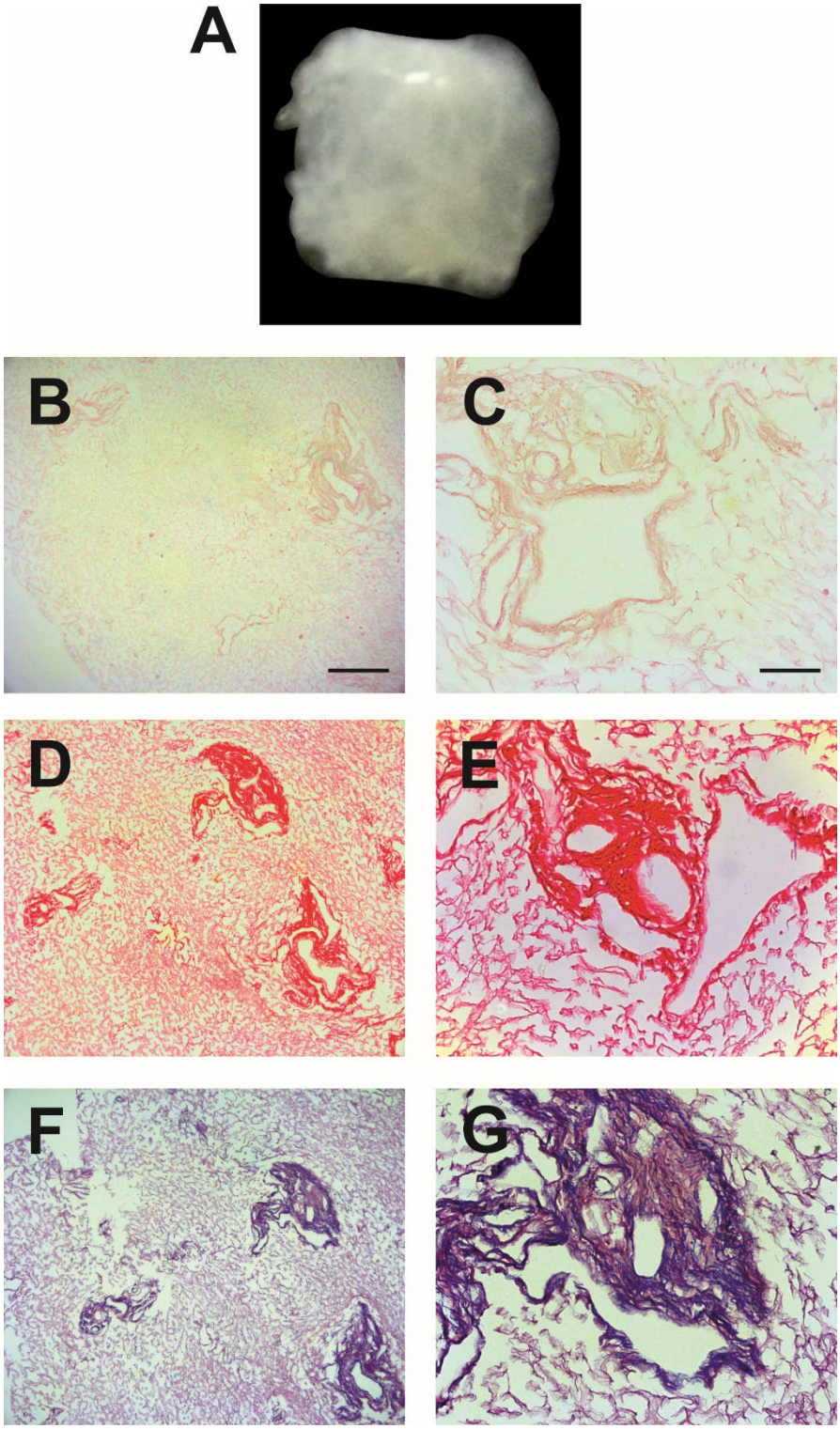

Figure 4.7. Histological characterization of high g-force protocol. Macroscopic appearance and histological analysis after decellularization (A), confirmed elimination of nuclear (blue; H&E, B,C) and cellular material (yellow; SR, D,E), preservation of collagen (red; SR, D,E), and elastin (purple; EVG, F,G). Scale bar B,D,F = 200 μm and C,E,G= 50 μm.

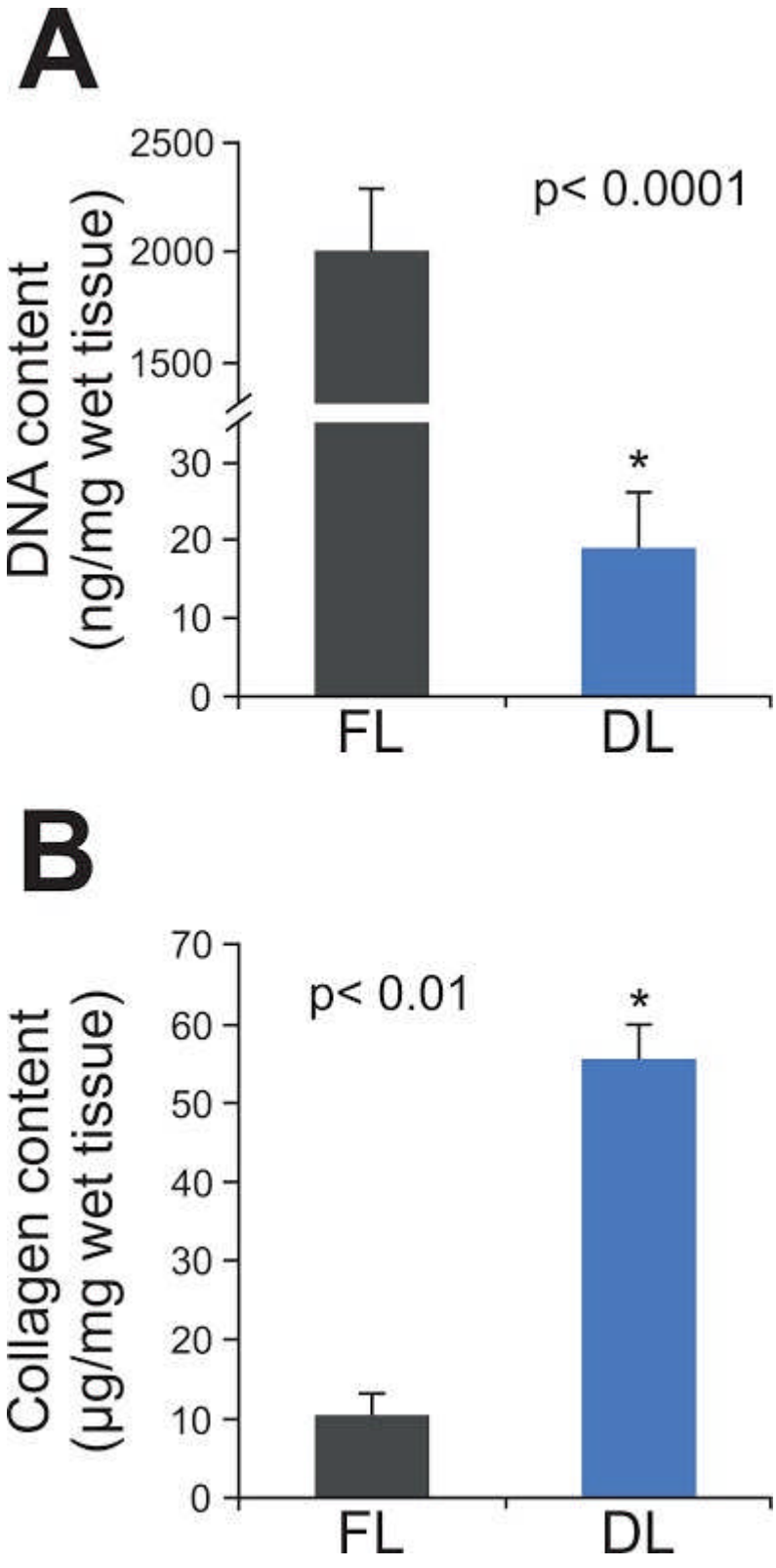

Figure 4.8. DNA and collagen quantification comparison between native and decellularised tissue by employing high-g force protocol. The figure shows significant ($p<0.0001$) elimination of DNA in ALTCs (A). Collagen quantification of fresh liver samples and ALTCs showing significant increase ($p<0.01$) in the total collagen content after decellularization (B).

4.3.2 ECM protein distribution and composition.

Next, the expression and distribution of the extracellular matrix (ECM) proteins in ALTCs was analysed. Immunohistochemistry analysis showed that the expression and distribution of key ECM components, namely collagen type I, collagen type III, collagen IV, fibronectin and laminin (Figure 4.9) were maintained in ALTCs when compared to native liver tissue.

Furthermore, the composition of ECM proteins within the ALTCs was qualitatively investigated by proteomic analysis (Table 4.4). The protein score, which reflects the sum of the ion scores of all peptides that were identified, was increased for all proteins identified after decellularization when compared with the native tissue.

Notably, the main fibrillar and structural collagens (collagen alpha-1,-3,-6) as well as laminins were preserved after decellularization. In addition, other ECM proteins were identified only within the acellular scaffold and were mainly represented by proteoglycans (lumican and mimecan) and glycoprotein (vitronectin).

In contrast to this, other ECM proteins were identified exclusively in the native tissue such as laminin B1 and prelaminin-A/C.

Overall, this analysis confirmed the preservation of key ECM components in the acellular scaffold.

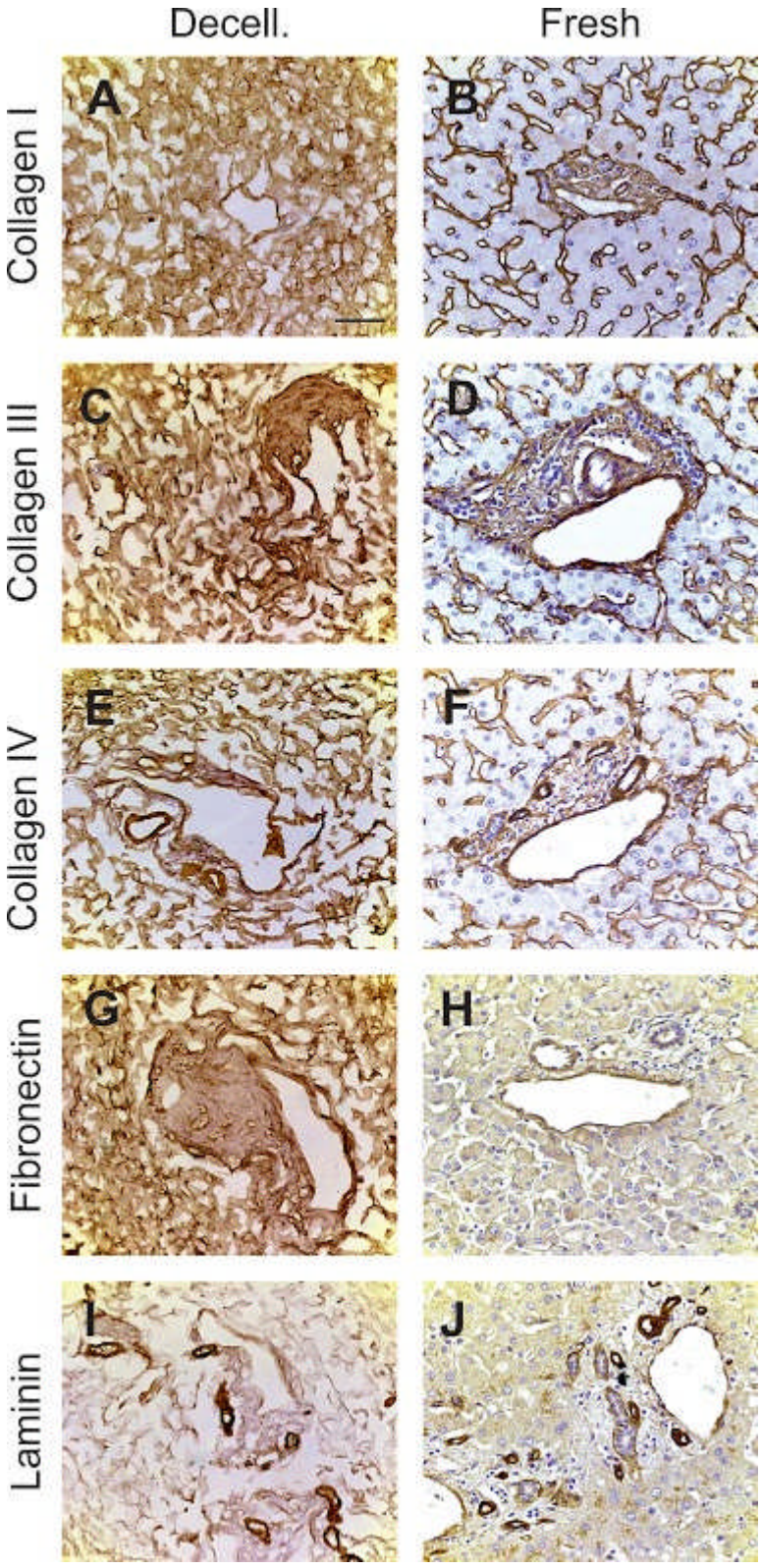

Figure 4.9. Immunohistochemistry of ECM proteins. Comparison of different ECM protein expression and distribution evaluated by immunohistochemistry between decellularized cubes (left panel) and fresh samples (right panel) showing preservation of the ECM proteins after decellularization. Scale bar =100 μm.

A

Native Tissue

UniProt Entry Name	Protein	Gene	Organism	PE	SV	Protein Score
CO1A1_HUMAN	Collagen alpha-1(I) chain	COL1A1	Homo sapiens	1	5	97
CO3A1_HUMAN	Collagen alpha-1(III) chain	COL3A1	Homo sapiens	1	4	36
CO6A1_HUMAN	Collagen alpha-1(VI) chain	COL6A1	Homo sapiens	1	3	69
CO1A2_HUMAN	Collagen alpha-2(I) chain	COL1A2	Homo sapiens	1	7	112
CO6A3_HUMAN	Collagen alpha-3(VI) chain	COL6A3	Homo sapiens	1	5	131
FINC_HUMAN	Fibronectin	FN1	Homo sapiens	1	4	31
LMNB1_HUMAN	Lamin-B1	LMNB1	Homo sapiens	1	2	17
LMNA_HUMAN	Prelamin-A/C	LMNA	Homo sapiens	1	1	92

B

Decellularised Tissue

UniProt Entry Name	Protein	Gene	Organism	PE	SV	Protein Score
CO1A1_HUMAN	Collagen alpha-1(I) chain	COL1A1	Homo sapiens	1	5	379
CO3A1_HUMAN	Collagen alpha-1(III) chain	COL3A1	Homo sapiens	1	4	59
CO6A1_HUMAN	Collagen alpha-1(VI) chain	COL6A1	Homo sapiens	1	3	204
CO1A2_HUMAN	Collagen alpha-2(I) chain	COL1A2	Homo sapiens	1	7	268
CO4A2_HUMAN	Collagen alpha-3(VI) chain	COL4A2	Homo sapiens	1	4	58
CO6A2_HUMAN	Collagen alpha-2(VI) chain	COL6A2	Homo sapiens	1	4	206
CO6A3_HUMAN	Collagen alpha-3(VI) chain	COL6A3	Homo sapiens	1	5	783
FINC_HUMAN	Fibronectin	FN1	Homo sapiens	1	4	171
LAMA5_HUMAN	Laminin subunit alpha-5	LAMA5	Homo sapiens	1	8	81
LAMB2_HUMAN	Laminin subunit beta-2	LAMB2	Homo sapiens	1	2	31
LUM_HUMAN	Lumican	LUM	Homo sapiens	1	2	28
MIME_HUMAN	Mimecan	OGN	Homo sapiens	1	1	85
VTNC_HUMAN	Vitronectin	VTN	Homo sapiens	1	1	105

Table 4.4. Proteomic analysis of different ECM proteins in fresh liver samples and ALTCs (A and B, respectively).

4.3.3 3D architecture and ultrastructure.

Scanning electron microscopy (SEM) was used to 1) compare native tissue (Figure 4.10 A-C) with decellularized tissue as well as 2) to evaluate how the

decellularization affected the micro-structure of the ECM (Figure 4.10 D-F). The overall liver tissue micro-structure appeared maintained. Key architectural structures such as portal tracts were recognised with their typical features and distribution within the scaffold (Figure 4.10 D, asterisk). The areas corresponding to the liver lobule were characterised by a three-dimensional network of connective tissue fibres arranged in a honeycomb-like structure (Figure 4.10 E). Most notably, the hepatocyte pocket was preserved and was surrounded by a detailed network of ECM proteins (Figure 4.10 F). Overall, these data confirm the preservation of the 3D liver microanatomy and ultrastructure following decellularization.

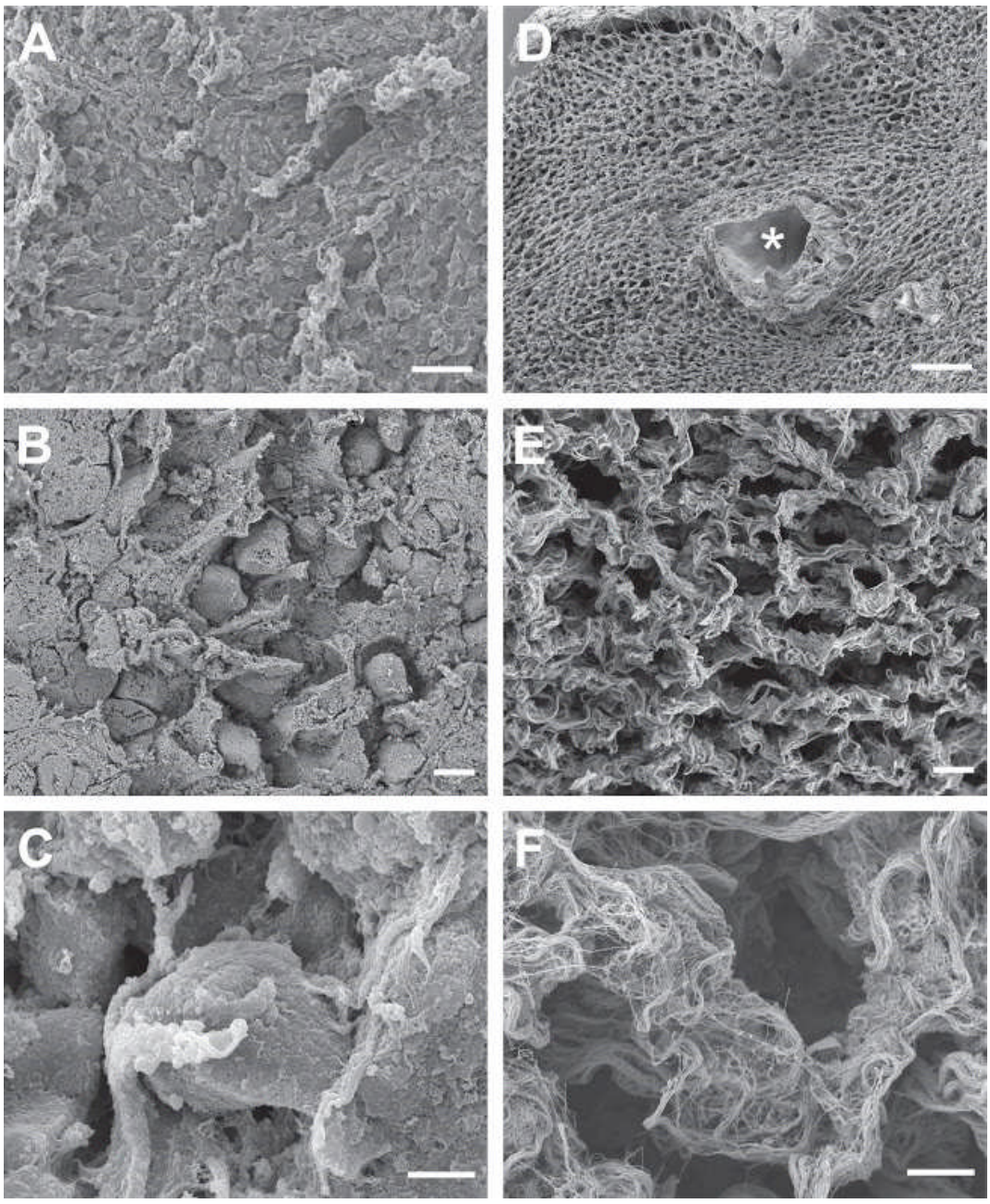

Figure 4.10. Ultrastructural characaterisation of native and decellularised liver. SEM imaging of (A-C) fresh liver samples, and (D-F) decellularized liver cubes (asterisks showing preservation of portal tract). Scale bars A,D = 100 μm and B,C,E,F= 10 μm.

Visualisation of the collagen type I organisation was conducted via second harmonic generation (SHG) microscopy alongside multiphoton microscopy (MPM) allowing autofluorescence from elastin to be visualised. Distinctly differing organisation and distribution of collagen type I in the decellularized and native tissue sections are seen through the SHG signal, with the decellularized tissue containing more concentrated regions than the native tissue sections probably due to the removal of cellular materials which outdistance the 3D organisation of collagen fibres (Figures 4.11). Furthermore, regions on the scaffold show areas where collagen fibres are aligned indicating stiffer regions where there is reinforcement due to a more dense distribution of collagen. In contrast, collagen observed in the native tissue sections is seen to predominantly surround regions in the tissue that are indicated in the MPM signal. This indicates that the decellularization procedure does not affect the hepatic 3D architecture while collagen type I fibres appeared to be more concentrated and aligned due to cellular removal.

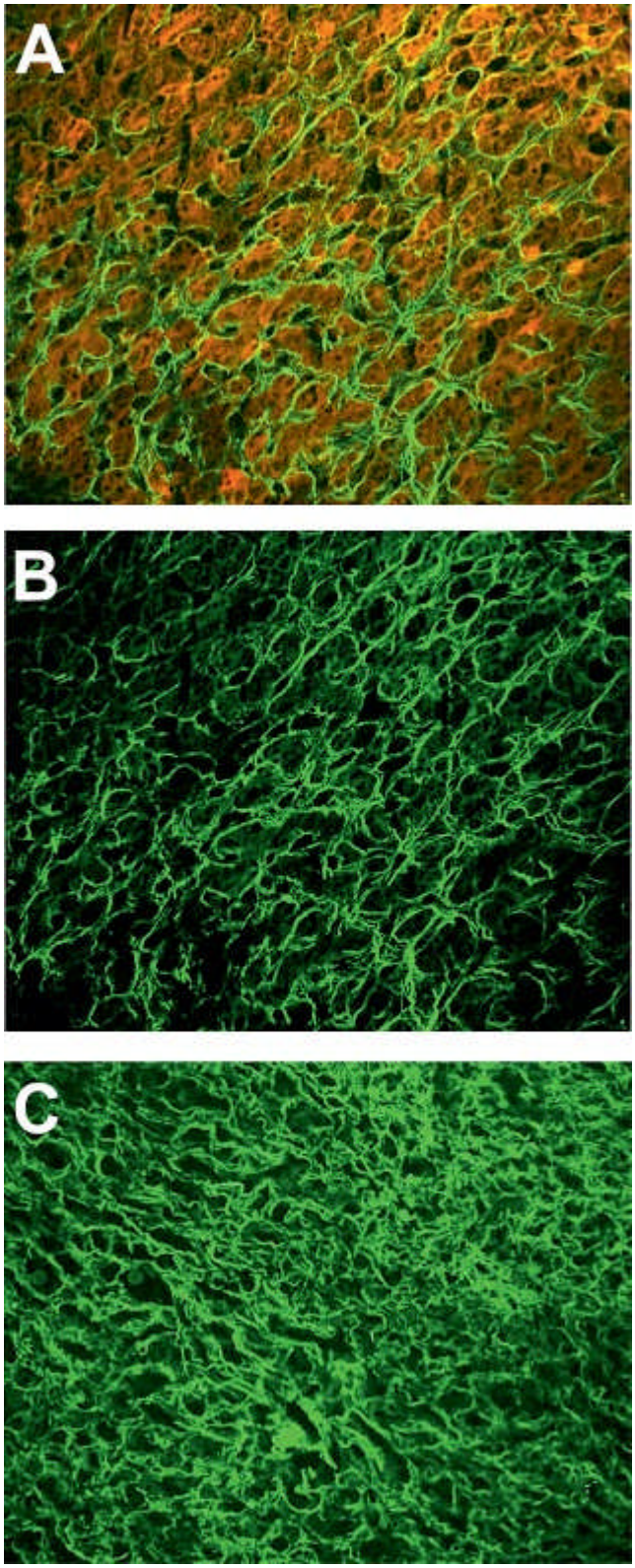

Figure 4.11. Second harmonic generation analysis of native and decellualarised liver. The figure shows fibrillar collagens (green) structure of (A) fresh liver samples with the presence of cells (red), (B) fresh liver samples with the subtraction of cells and (C) ALTCs .

4.3.4 Biochemical and biomechanical features of decellularized liver tissue.

Raman spectroscopy is an optical technique based on inelastic scattering of light that can provide detailed molecular analysis of biological samples[231]. This technique has a high chemical specificity as the shifts in the energy of laser photons provide information regarding molecular vibrations in the sample. The biochemical spectral Raman fingerprint has previously been used to detect tissue pathology (e.g. cancer, fibrotic tissue) and to characterise the ECM generated from tissue engineered constructs[232,233].

The results obtained from confocal auto-fluorescence microscopy and Raman spectral analysis on two ALTCs obtained in two independent experiments from the same liver (Figure 4.12 A, B) showed tissue auto-fluorescence emission in the wavelength between 450 – 480 nm when excited at 405 nm, which is an indication of high content of collagen in the samples[234]. Furthermore, the confocal fluorescence images allowed selection of areas for Raman spectroscopy measurements. Areas of 4x4 mm^2 were selected to ensure that spectral variations due to sample heterogeneity are captured.

To understand the chemical composition of the samples, as well as variations across the sample, the spectral maps were analysed using Principal Component Analysis. The present pseudo-colour images based on the first six components highlighted the overall morphology of the tissue samples (Figure 4.12 C, D). The typical Raman spectra selected from each sample indicated strong fluorescence emission (Figure 4.12 E, F). The Raman spectra were similar to Raman spectra of collagen[235], showing strong Raman bands at 851 cm-1 and 950 cm-1 assigned to proline and hydroxyproline, 1004 cm-1 corresponding to phenylalanine, amide III bands at 1246 cm-1, 1271 cm-1, CH2 deformations at 1450 cm-1 and Amide I at 1660 cm-1. However, due to the low signal-to-noise ratio, they cannot be used to discriminate different types of collagen. Therefore, a K-means (k=3) clustering method was applied to the entire dataset to understand the main spectral features. The centroid spectra for both samples are illustrated in figure 4.13, which represent the overall dominant bands of the samples including also the spectra differences between A and B. It is worth noting that the two samples have similar averaged spectra, with very low spectral differences. Furthermore, the Raman

spectra indicate that no bands typically measured in the Raman spectra of cells could be detected[236].

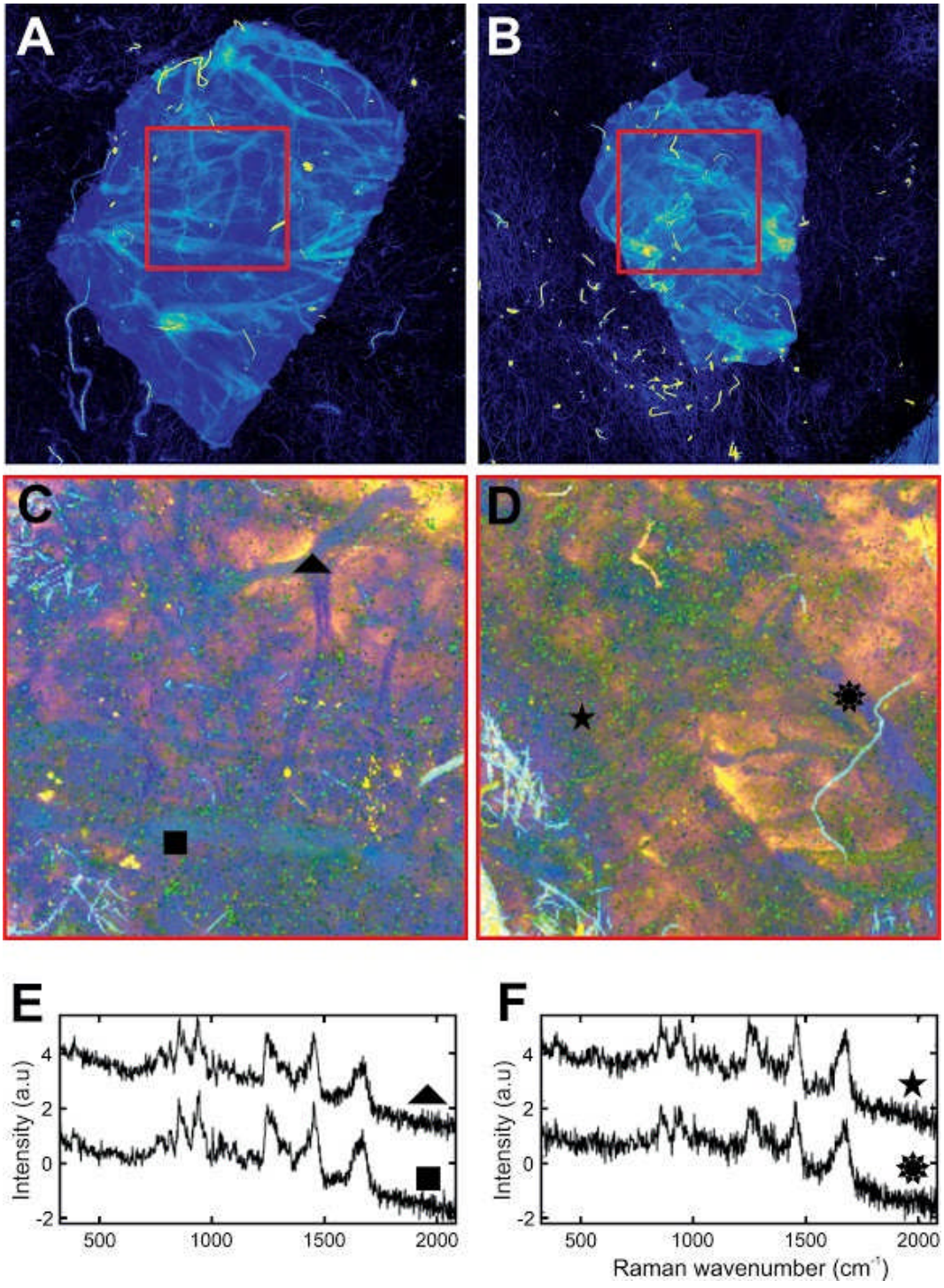

Figure 4.12. Ramen spectroscopy analysis of two different ALTCs. (A, B) Confocal auto-fluorescence microscopy showing preservation of the vascular trees. (C,D) Pseudo-colour images based on the first six component, highlighting the overall morphology of the ALTCs. (E, F) Raman spectra from different points on the cubes, showing similar spectra pattern to collagen.

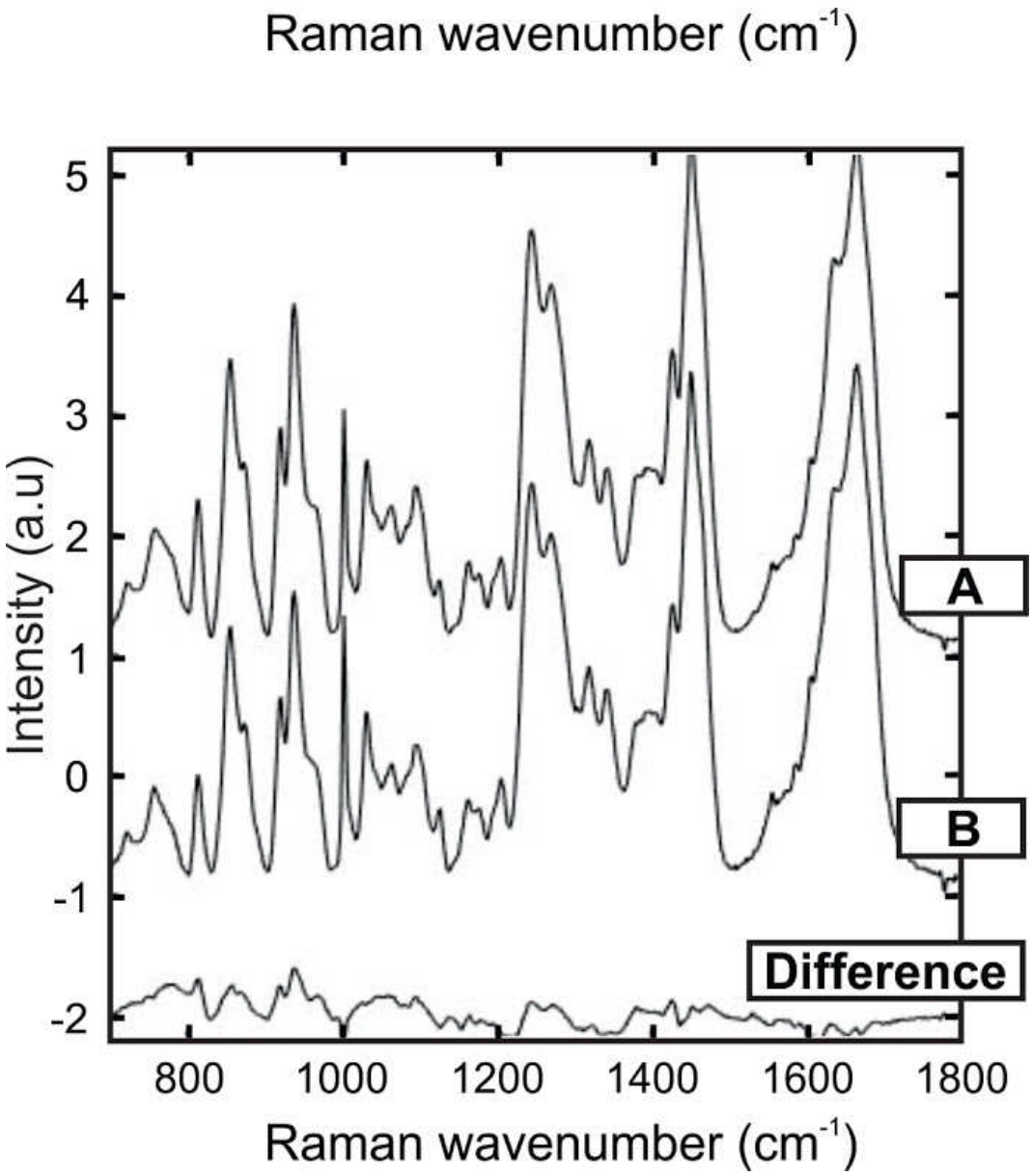

Figure 4.13. Differences between Raman spectra of two different ALTCs. Biochemical peaks of collagen proteins demonstrating no variability between the 2 different ALTCs.

Biomechanical characterisation of decellularized and native liver tissue was conducted with atomic force microscopy (AFM). Calculation of the Young's modulus from the AFM force curves demonstrated a significant difference ($p<0.05$) between the stiffness of decellularized liver tissue and the native tissue (Figure 4.14). As previously published in other works related to biological scaffolds [237], the Young's modulus calculated for the decellularised liver tissue was 2.051±0.39 kPa (SEM), around twice as great as that calculated for the native liver tissue (0.98±0.14 kPa).

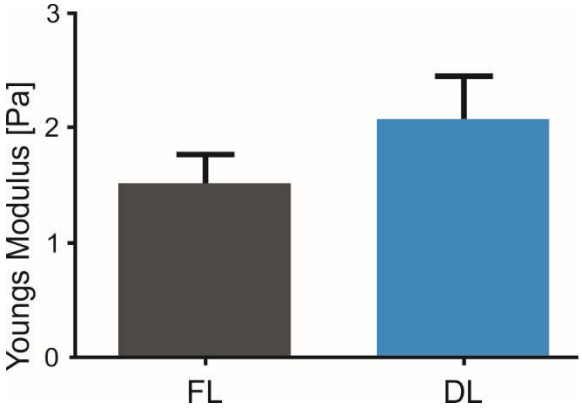

Figure 4.14. Biomechanical properties of native and decellularised liver. Atomic Force Microscopy (AFM) comparison of tissue stiffness between fresh and ALTCs.

4.3.5 Pro-angiogenic properties of acellular human liver scaffold

The chicken egg chorioallantoic membrane (CAM) assay was used to test *in vivo* the ability of ALTCs to attract blood vessels (Figure 4.15 A-D). Fragments of decellularized liver cubes were placed on the CAM and observed macroscopically for 7 days. The scaffolds integrated well with the developing environment of the chicken egg and representative images of ALTCs placed *in ovo* at 7 days of incubation demonstrated attraction of blood vessels in a spoke-wheel pattern (Figure 4.15 A). The effect of ALTCs on directed blood vessel growth was quantified by counting the total number of blood vessels converging towards the ALTCs. After 7 days from implantation the number of vessels growing towards ALTCs was significantly increased in comparison to the same sample at day 0 and to the membrane loaded with PBS that was used as a negative control (Figure 4.15 D, $p<0.05$). Interestingly, angiogenesis induced by the ALTCs 7 days post implantation into the CAM, was also statistically higher than pro-angiogenic cytokine VEGF-loaded membrane used as positive control (Figure 4D).

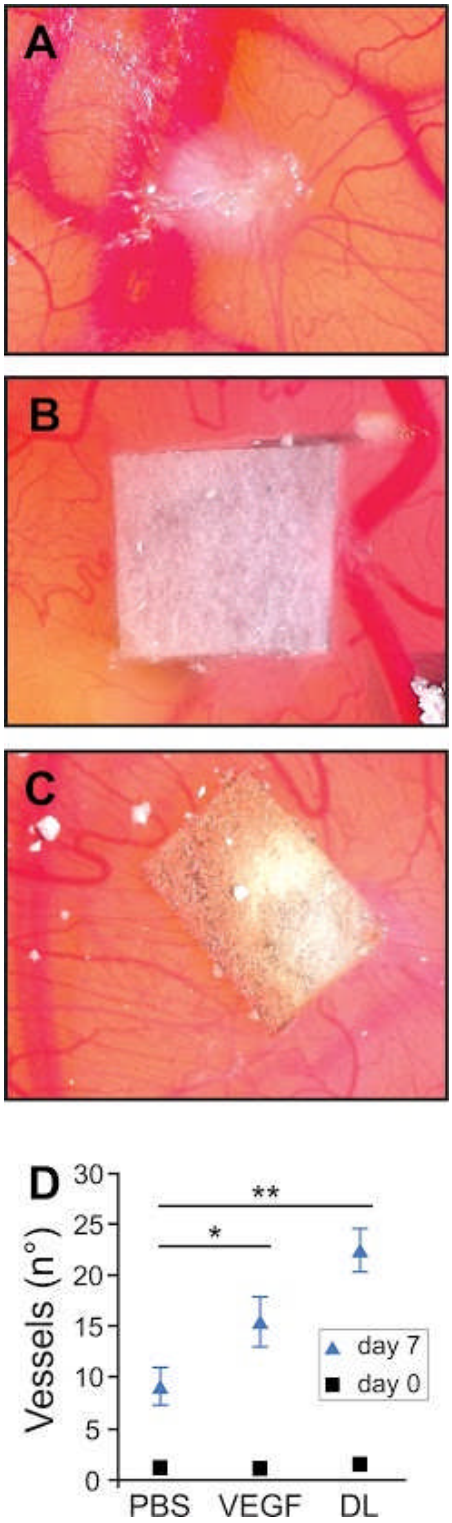

Figure 4.15. Chorioallantoic membrane (CAM) assay. CAM assay of (A) decellularized liver cube (B) sponge soaked in PBS, and (C) sponge soaked in VEGF. (D) Quantification of observed vessels at 0 days and 7 days, showing a significant difference between the decellularized liver cubes when compared to both sponges.

4.3.6 Re-endothelization of acellular liver tissue cubes.

After testing the pro-angiogenic capabilities of ALTCs, we assessed the recellularization of intra-hepatic vessels by employing human umbilical endothelial vein cells (HUVECs). HUVECs were seeded into the ALTC and engineered tissues were evaluated after 7 days of culture. After 7 days endothelial cells were uniformly lining the luminal surface of large vessels (Figure 4.16 A-C). In addition, the homogeneous expression of platelet endothelial cell adhesion molecule (PECAM-1) (Figure 4.16 D-F) and FVIII confirmed the maintenance of endothelial-like features (Figure 4.16 G-I).

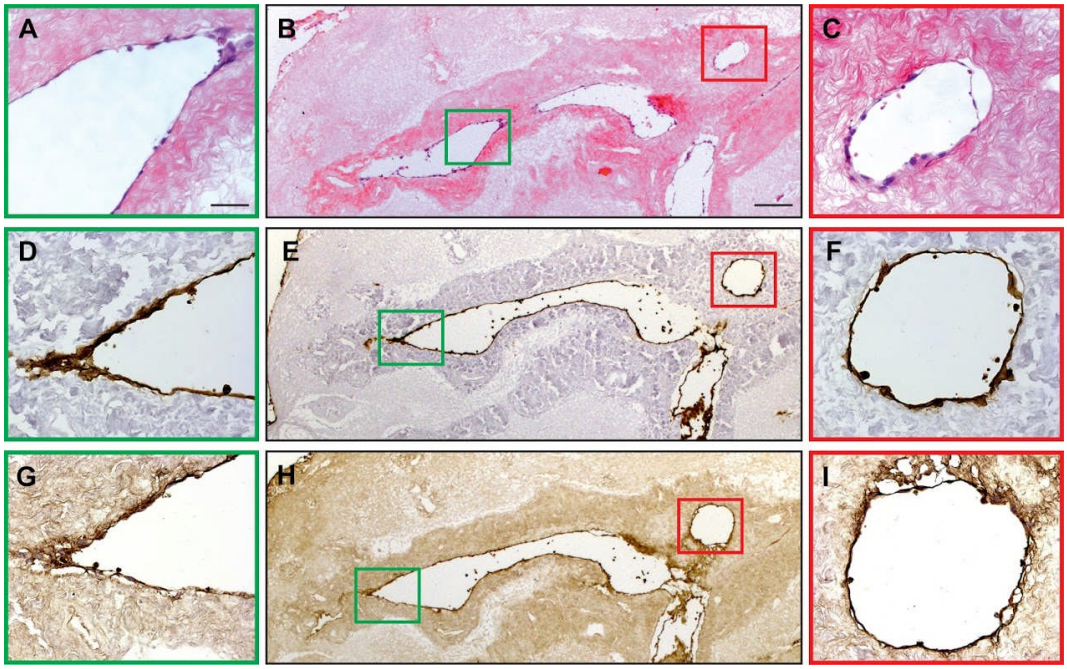

Figure 4.16. Histological and immunohistochemical characterisation of recellularised ALTCs with HUVECs, characterised by (A-C) H&E, (D-F) CD31 and (G-I) FVIII. Scale bars A,C,D,F,G,I = 50 μm or B,E,H = 200 μm.

4.3.7 Bioengineering of ALTCs scaffolds with human liver cell types

Next, the capability to repopulate the ALTCs with different hepatic cell types was explored and evaluated after 7 and 14 days of *in vitro* culture. After 7 days of seeding, HepG2 cells were found attached to the surface of the scaffold and showed to repopulate the scaffold after 14 days, respectively (Figure 4.17 A, D). HepG2 cells were characterized by an epithelioid phenotype as shown by SEM and were diffusely spread and engrafted into the ECM scaffold (Figure 4.18). Immunohistochemical staining revealed a strong positivity for alpha feto protein (AFP) at 7 days which was sustained after 14 days of incubation (Figure 4.17 B, E). In addition, cell adhesion within the acellular tissue was confirmed by a sustained expression of the epithelial cell adhesion marker (EpCAM) at both 7 and 14 days (Figure 4.17 C, F). Moreover, the expression of human albumin and the phase II metabolism enzyme UGT1A1 were evaluated in order to assess the metabolic activity of the engrafted hepatocytes. Quantitative RT-PCR revealed that the expression level of albumin was higher in the recellularized liver at 14 days when compared with a standard 2D culture, thus suggesting that the 3D acellular tissue was able to maintain the differentiated phenotype for a longer time period (Figure 4.19 A, $p < 0.001$ versus 2D culture). This finding was also supported by higher level of expression in the recellularized liver of phase II metabolism enzyme UGT1A1 at 14 days (Figure 4.19 B, $p < 0.005$ versus 2D culture).

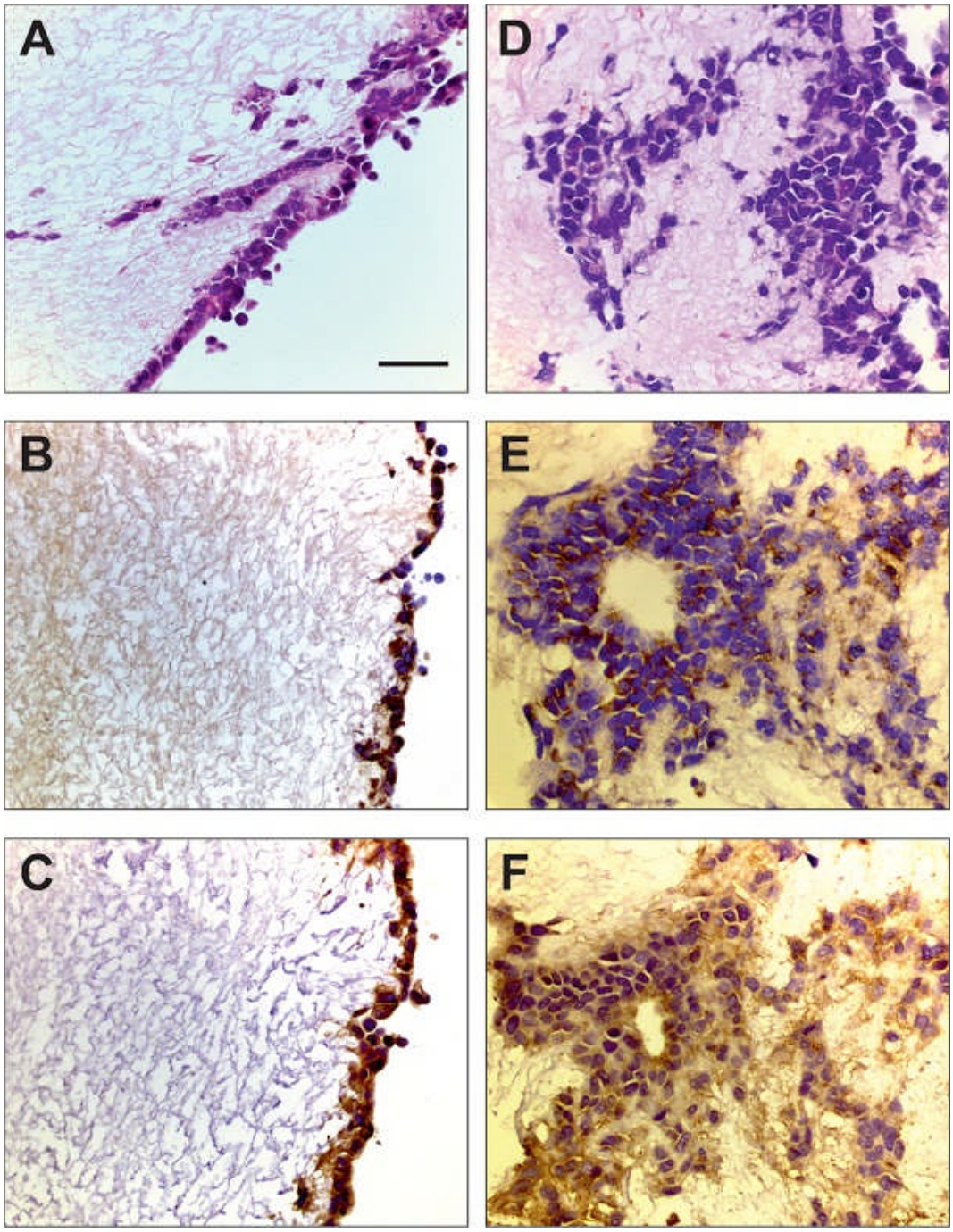

Figure 4.17. Histological and immunohistochemical characterisation of recellularised ALTCs with HepG2. Reseeded HepG2 were confirmed with (A,D) H&E staining and expression of (B,E) AFP and (C-F) EPCAM at both 7 (left panel) and 14 days (right panel). Scale bars = 50 μm.

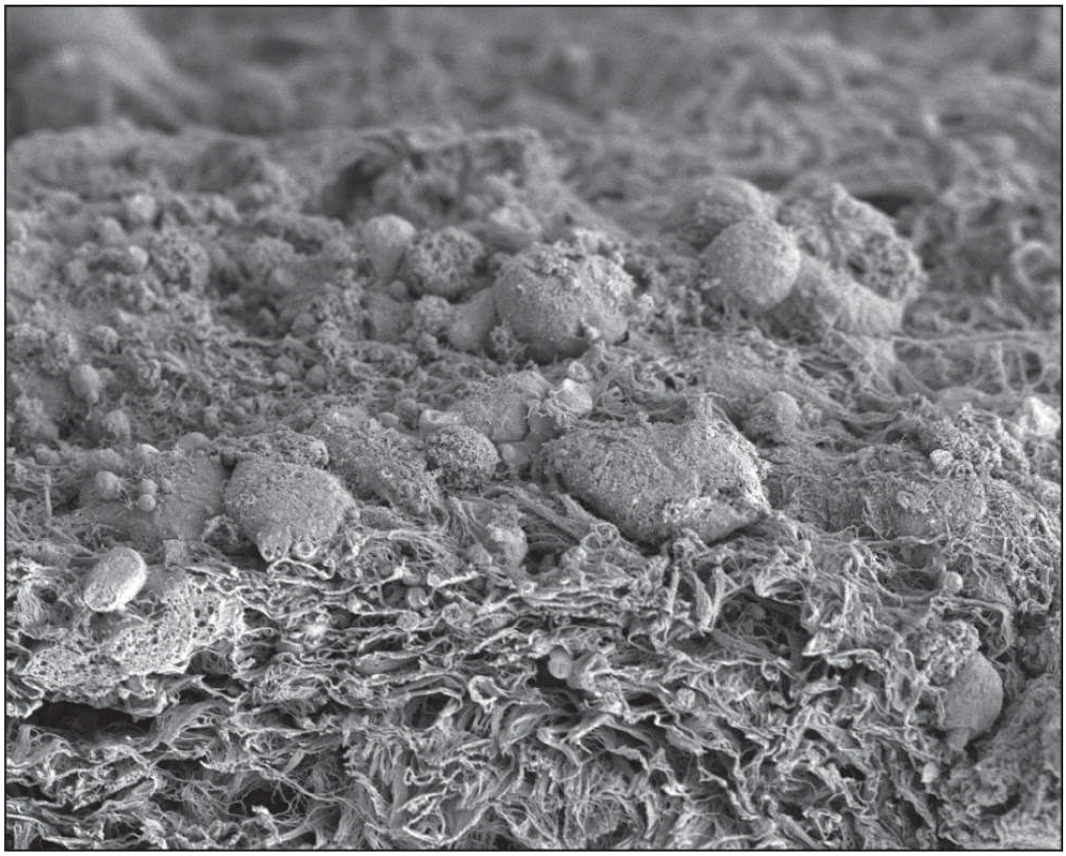

Figure 4.18. SEM image of engrafted Hepg2. The figure indicates epithelioid phenotype after seeding in decellularised liver. Scale bars = 10 μm.

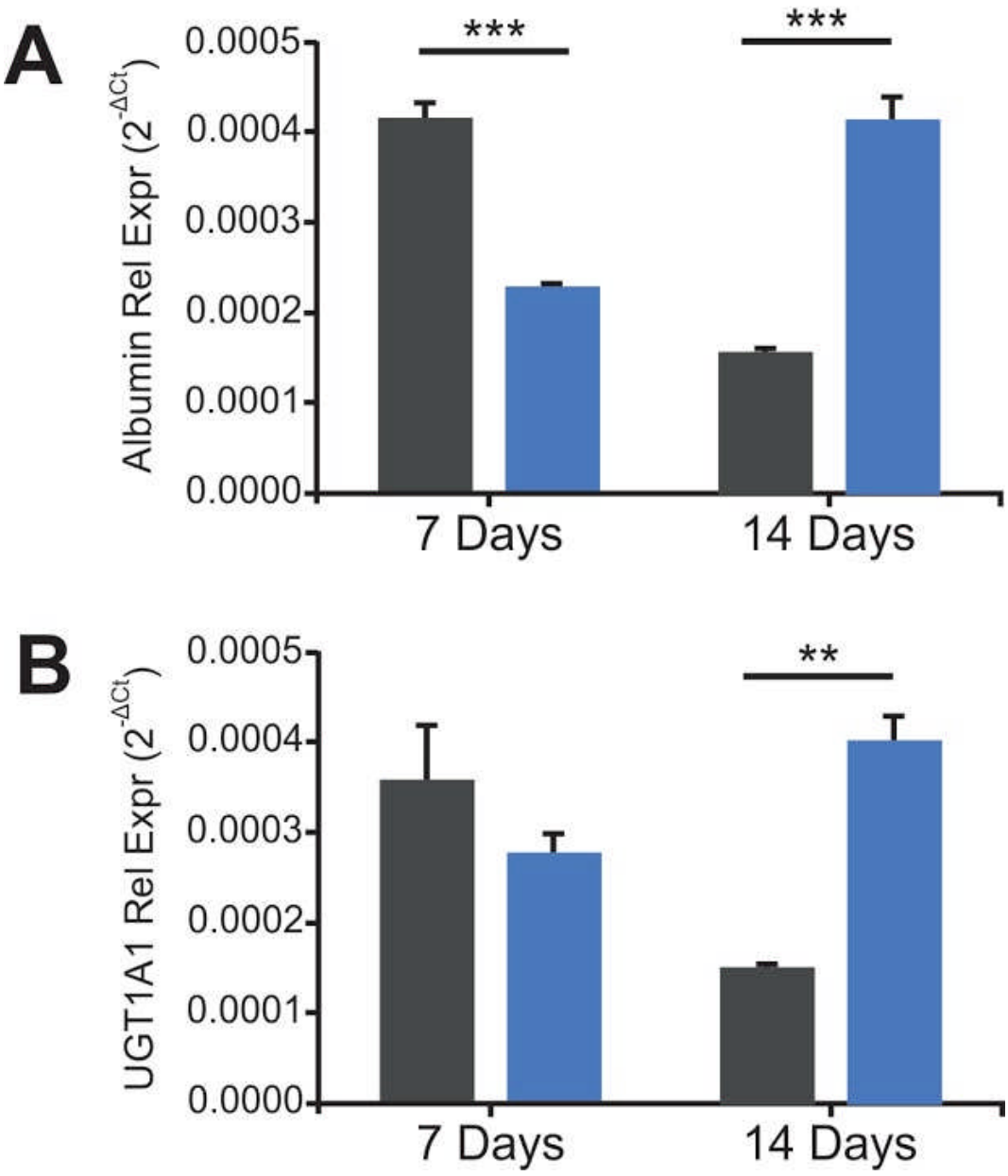

Figure 4.19. Gene expression analysis of engineered ALTCs with Hepg2. Quantitative comparison of (A) albumin and (B) UGT1A1 gene expressions of HepG2 grown on 2D plastic and those reseeded on decellularized liver cubes.

Similarly, H&E staining demonstrated the progressive engraftment of LX2 cells into the scaffold after 14 days compared to 7 days (Figure 4.20 A, B). SEM analysis further demonstrated that LX2 cells migrated within the decellularized sinusoidal space acquiring a definite fibroblast-like cell phenotype (Figure 4.21).

The pro-fibrogenic phenotype of the cells migrated into the scaffold was assessed by the expression of cellular markers typical of liver fibrosis[39]. The expression of

key growth factor receptors such as platelet derived growth factor beta receptor (PDGFβ-R) (Figure 4.20 C, D) and transforming growth factor beta receptor (TGFβ-R) (Figure 4.20 E, F) was detected by immunohistochemistry. However, an interesting difference in the mRNA expression of two keys pro-fibrogenic molecules, namely collagen type-1 and lysil oxydase (LOX) was observed by comparing cells cultured in 3D-scaffolds versus standard 2D conditions. Indeed, collagen type-1A1 expression was significant reduced in 3D culture ($p<0.01$) (Figure 4.22 A) while LOX2 was significantly increased in cells cultured in 3D conditions when compared with 2D culture ($p<0.001$) (Figure 4.22 B).

All together these findings demonstrated sufficient viability and function after scaffold engineering.

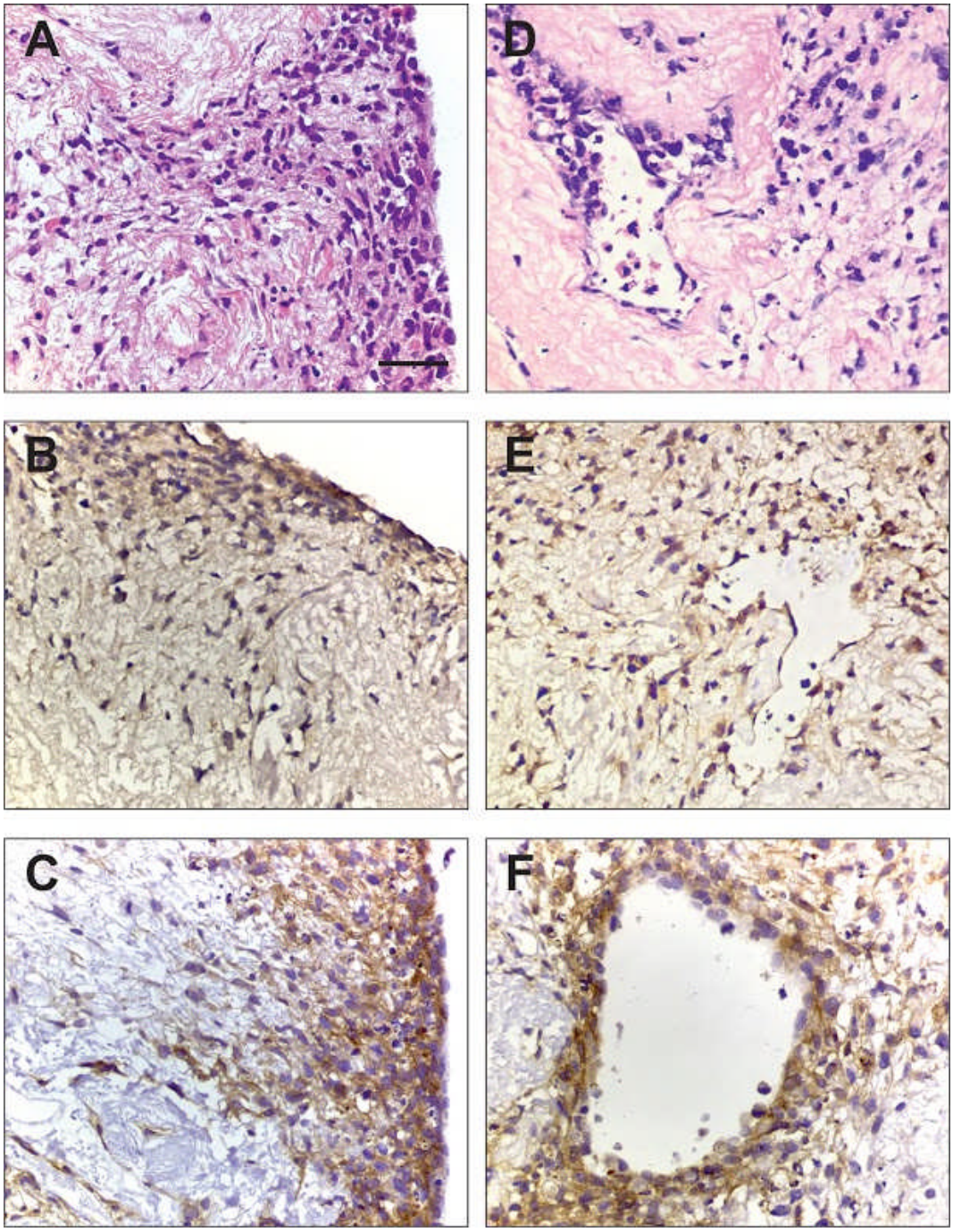

Figure 4.20. Histological and immunohistochemical characterisation of recellularised ALTCs with LX2. Reseeded LX2 were confirmed with (A,D) H&E staining, and expression of (B,E) PDGFB-β and (C,F) TFG-β at both 7 (left panel) and 14 days (right panel). Scale bars = 50 μm.

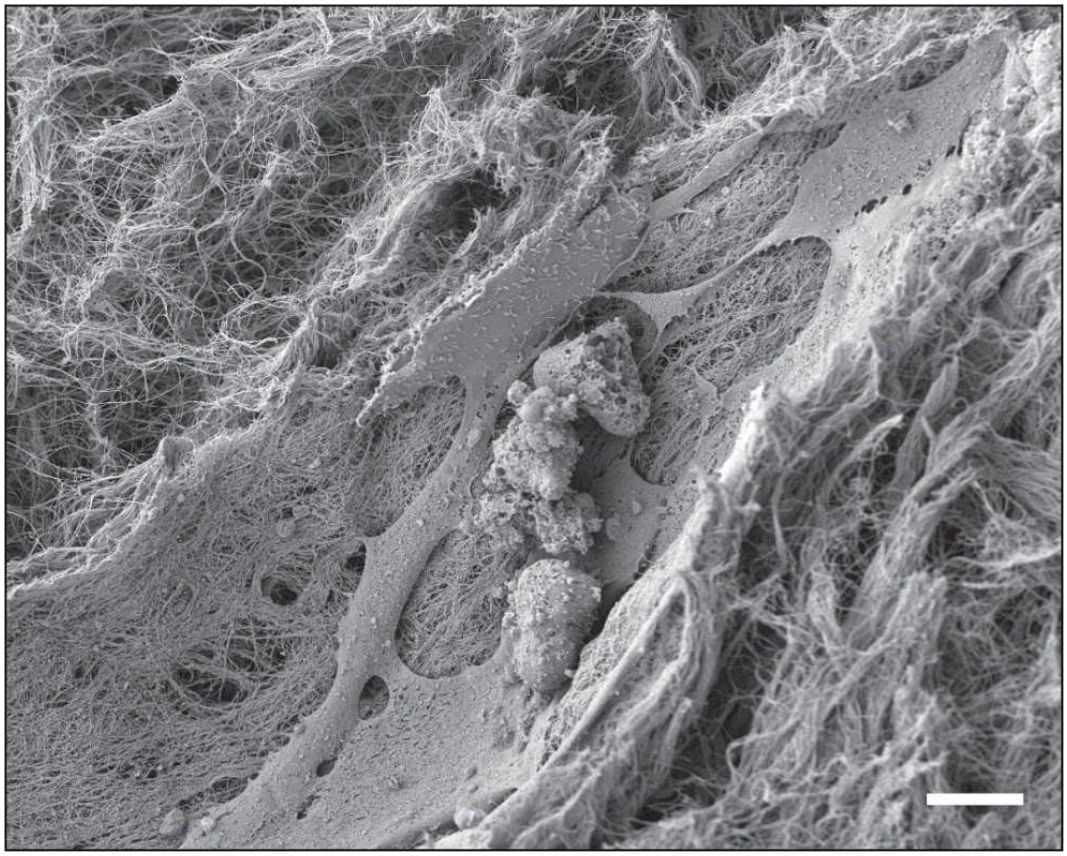

Figure 4.21. SEM image of engrafted LX2. The figure indicates fibroblast-like phenotype after seeding in ALTCs. Scale bars = 10 μm.

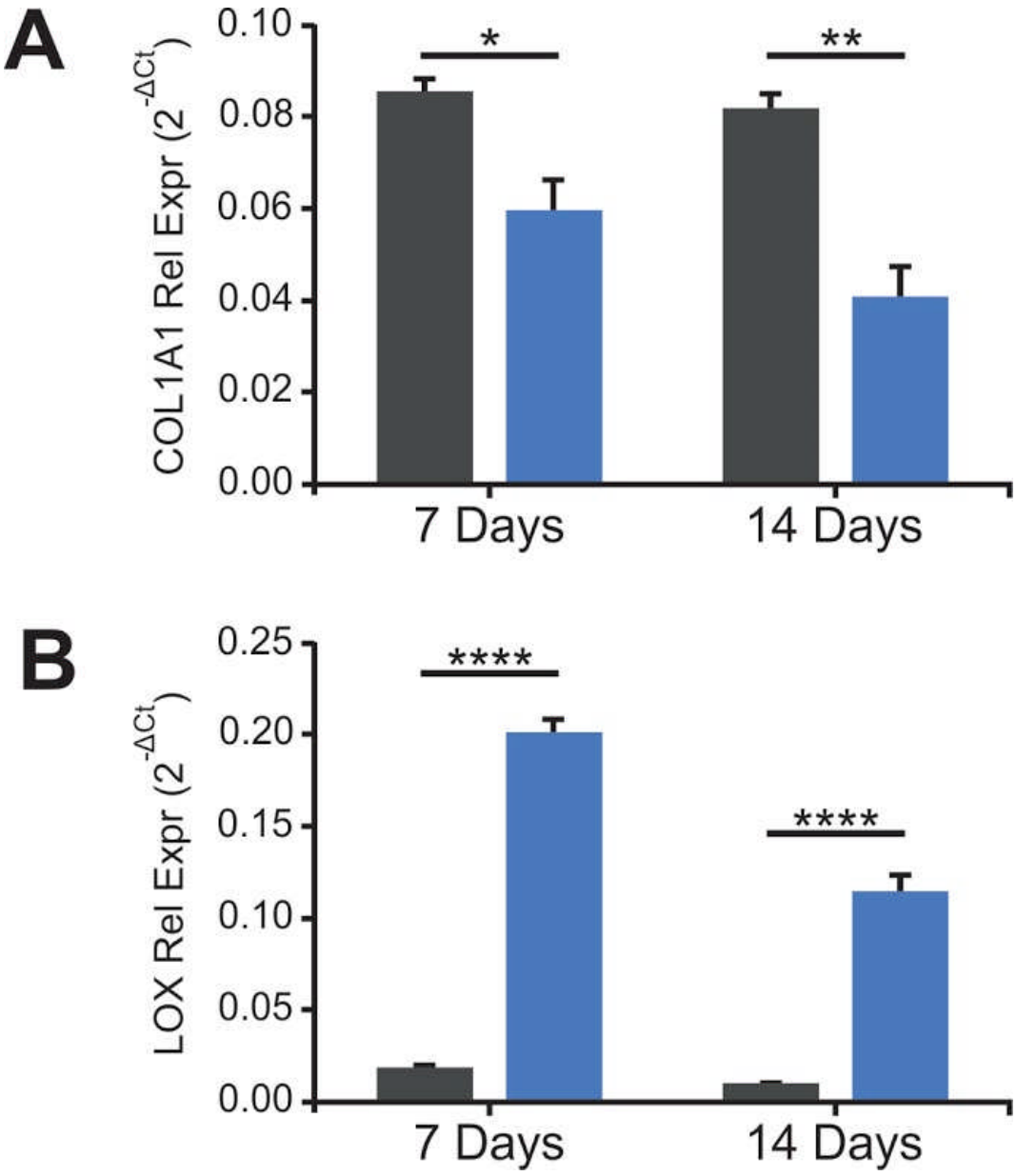

Figure 4.22. Gene expression analysis of engineered ALTCs with LX2. Quantitative comparison of (A) COL1A1 and (B) LOX gene expressions of LX2 grown on 2D plastic and those reseeded on ALTCs.

4.4 Discussion

This work demonstrates that small scale human liver biological scaffolds can be derived by a process of agitation-decellularization employing high flow shear stress (high g-force) which reduces processing time. The resultant 3D-human liver scaffolds are characterized by the preservation of the essential biochemical, physical and topographical properties and in addition can be engineered with different types of human liver cells.

The field of agitation-decellularization was pioneered by Meezan and colleagues in 1975[153], who proposed this methodology for studying the basement membrane microstructure. Subsequently, this methodology has been adapted to decellularize sections of different tissues, including xenogenic liver, by incubating the native tissue with different detergents without defining the mechanical forces[109,124,133,140-142,238].

A key contribution of the work described in this chapter is the development of a novel decellularization protocol based on high g-force oscillation leading to the successful removal of immunogenic cellular materials, while maintaining the ECM protein composition and 3D architecture.

These results offer a key advance towards the use of whole healthy human livers unsuitable for liver transplantation or wedges of resected liver tissue for functional tissue engineering aimed at providing platforms for human disease modelling and assessment of drug efficacy/toxicity.

Along these lines, a necessary step is represented by the ability of the decellularized tissue to be repopulated by organ-specific cell types. Indeed, human parenchymal (HepG2) and non-parenchymal (LX2) cell lines engrafted within the human acellular liver tissue developed with the newly proposed protocol. Although a successful engraftment was shown also with primary human hepatocyte and hepatic stellate cells, the standardisation of the tissue engineering protocol was obtained with the above mentioned cell lines in order to reduce the variability inherent to the use of different isolates of primary human cells. The expression of phenotype-specific markers for both human parenchymal and non-parenchymal liver cells indicated that the engrafted cells maintain differentiation and functionality. This was proven by the fact that HepG2 cells grown in 3D-scaffolds were able to maintain higher cellular differentiation features following

prolonged culture when compared to the same cell preparation grown on standard 2D-plastic conditions.

Similarly, LX2 cells grown in 3D-scaffolds retained the phenotype of activated cells. Importantly, the mRNA expression of key pro-fibrogenic genes (collagen type-1 and LOX2) showed remarkable difference with the same cell preparation grown on standard 2D-plastic conditions. These results underwrite the existence of uncertainties on the accuracy and validity of target definition for a given pathological process obtained by performing *in vitro* studies on artificial 2D plastic systems.

Although small scale scaffolds cannot be perfused directly through the main vasculature system, the ALTC maintain the vasculature structure and protein composition of the native tissue. This was confirmed by demonstrating the selective re-endothelization of human endothelial cells in ALTCs.

Altogether the current results provide an innovative basis for further developments in the area of all human *in vitro* 3D-platforms for the study of disease pathophysiology, pharmacological target discovery and drug toxicity assessment.

Chapter 5: Discussion and future work

Recent advances in the field of regenerative medicine hold promise for the regeneration of different tissues and organs for clinical use. Tissue engineering of simple structures such as bladder[239], urethra[240] and veins[241] has already been translated into important clinical applications. However research on more complex parenchymal organs has been less extensive.

Before starting the work described in this thesis, there were no publications demonstrating human liver tissue decellularisation. As outlined in Chapter 1, Paul Lin et al. were the first to attempt animal liver tissue decellularisation in 2004 for tissue engineering purpose[124]. In their experiments key functions of primary rat hepatocytes seeded on (i) monolayer culture over absorbed collagen, (ii) cultured between collagen gels and (ii) in decellularised porcine liver tissue scaffolds were addressed.
They found that albumin and urea secretion (per viable cells) was significantly higher in the decellularised porcine liver tissue scaffolds than in the other two culture models, leading to the conclusion that biological scaffolds are superior to other traditional techniques in preserving hepatocyte function. However, although porcine livers are very similar to human livers in size, their ultrastructure differs significantly.

Indeed, porcine livers have well defined lobules as they are outlined with connective tissue. This connective tissue is absent in healthy human livers between lobules and are only present in diseased livers (e.g. cirrhosis)[242]. There is actually no animal liver with similar ultrastructure to human livers.

In the experiments concerning liver tissue engineering described in Chapters 2 and 4 it has been shown that an acellular natural matrix can be obtained from human liver without disruption of the structural and mechanical characteristics of the native tissue. The data described in this thesis provide a novel system capable of effectively decellularising healthy human liver tissue cubes and whole human livers[156]. This was achieved after employing and comparing previously described protocols which were shown to be effective for the decellularisation of animal

livers[44-46,243,244]. When compared to previously used methods, different reagents/enzymes were used. However, the breakthrough in the methodology was provided by the introduction of the retrograde perfusion (inflow from the central vein) which was more effective for the homogenous removal of cellular materials while preserving structural proteins, when compared with the antegrade system (inflow from the portal vein). Initially, the removal of cellular debris and DNA material was assessed both qualitatively and quantitatively. In addition, ECM protein preservation was histologically compared and further immunohistochemically analysed. Importantly, the resulting integrity of the vascular network represents a key premise for the re-endothelialization and reconstruction of the vascular network. In addition, the short time needed to obtain the natural scaffold could have a positive impact for its clinical application.

The method described in Chapter 4 is definitely of relevance for liver tissue bioengineering to be employed as a three-dimensional platform for drug testing and biological assays in vitro as a complementary or alternative approach to experimental animal models.

Indeed, the novel agitation-decellularisation protocol presented in Chapter 4 is an innovative and effective matching the principles of the 3Rs, which are replacement, refinement and reduction of animals in research. The mission of the National Center for the Replacement, Refinement and Reduction of Animal Research (NC3Rs), as stated on their website, is to "use the 3Rs principles to accelerate scientific discovery, support innovation and technological developments, and address societal concerns about animal research." These decellularised liver cubes would(i) accelerate scientific discovery, (ii) support innovation and (iii) reduce and replace animal use in many scientific research.

Lastly, as described in Chapter 3 we have demonstrated that a 3D ECM scaffold with a conserved vascular tree can be obtained from amyloidotic mouse liver with retention of the natural structure and specific amyloidogenic properties of the amyloid[185]. Decellularized amyloid organs provide an innovative experimental model to further investigate the relationship between the ECM and amyloid fibrils, including studies of the seeding effect of natural fibrils on amyloidogenic

protein precursors perfused in vivo and characterization of possible effects of natural amyloid fibrils on classical organ recellularization. High resolution, 3D images of amyloid in its natural environment may also be informative about the recently discovered putative expansive forces generated by fibril growth[245].

Overall, the way to progress towards potential clinical applications should be directed at: a) the evaluation of different protocols for recellularization by employing perfusion bio-reactors allowing optimal cell homing when different cell types are employed, either singularly or together; b) proteomic studies to assess the preservation of ECM proteins and the presence of residual cellular materials; c) the assessment of the metabolic requirements and functionality of the bioengineered liver, d) an estimation of the accuracy of different types of cell repopulation in reproducing 3D scenarios of liver pathophysiology fundamental for liver disease modelling as well as for drug toxicity/efficacy testing, and e) addressing ECM-disease associated biomarkers by performing proteomic evaluation of decellularised tissues derived from livers with different background of diseases.

References:

1 Sherlock, S. *Diseases of the Liver and Biliary System*. 11th Edition edn, (Blakwell Scientific Publications, 1955).

2 Irwin M. Arias *et al. The Liver Biology and Pathobiology*. 5th Edition edn, (Wiley, 2009).

3 Kmiec, Z. Cooperation of liver cells in health and disease. *Advances in anatomy, embryology, and cell biology* **161**, III-XIII, 1-151 (2001).

4 Godoy, P. *et al.* Recent advances in 2D and 3D in vitro systems using primary hepatocytes, alternative hepatocyte sources and non-parenchymal liver cells and their use in investigating mechanisms of hepatotoxicity, cell signaling and ADME. *Archives of Toxicology* **87**, 1315-1530, doi:10.1007/s00204-013-1078-5 (2013).

5 Friedman, S. L. Molecular regulation of hepatic fibrosis, an integrated cellular response to tissue injury. *Journal of Biological Chemistry* **275**, 2247-2250, doi:10.1074/jbc.275.4.2247 (2000).

6 Coulouarn, C. *et al.* Hepatocyte-Stellate Cell Cross-Talk in the Liver Engenders a Permissive Inflammatory Microenvironment That Drives Progression in Hepatocellular Carcinoma. *Cancer Research* **72**, 2533-2542, doi:10.1158/0008-5472.can-11-3317 (2012).

7 Bataller, R. & Brenner, D. A. Liver fibrosis. *The Journal of clinical investigation* **115**, 209-218, doi:10.1172/jci24282 (2005).

8 Rombouts, K. *Stellate Cells in Health Disease*. Vol. Hepatic Stellate Cell Culture Models: One History, Many Approaches. (Elsevier, 2014).

9 Hautekeete, M. L. & Geerts, A. The hepatic stellate (Ito) cell: Its role in human liver disease. *Virchows Archiv* **430**, 195-207, doi:10.1007/bf01324802 (1997).

10 Martinez-Hernandez, A. & Amenta, P. S. The hepatic extracellular matrix. I. Components and distribution in normal liver. *Virchows Archiv. A, Pathological anatomy and histopathology* **423**, 1-11 (1993).

11 Schuppan, D. Structure of the extracellular matrix in normal and fibrotic liver: collagens and glycoproteins. *Seminars in liver disease* **10**, 1-10, doi:10.1055/s-2008-1040452 (1990).

12 Rojkind, M., Giambrone, M. A. & Biempica, L. Collagen types in normal and cirrhotic liver. *Gastroenterology* **76**, 710-719 (1979).

13 NHS. *Liver disease*, <http://www.nhs.uk/conditions/liver-disease/Pages/Introduction.aspx> (2014).

14 Pawlak, M. *et al.* The transrepressive activity of peroxisome proliferator-activated receptor alpha is necessary and sufficient to prevent liver fibrosis in mice. *Hepatology (Baltimore, Md.)* **60**, 1593-1606, doi:10.1002/hep.27297 (2014).

15 Iavarone, M. & Colombo, M. HBV infection and hepatocellular carcinoma. *Clinics in liver disease* **17**, 375-397, doi:10.1016/j.cld.2013.05.002 (2013).

16 Rizzetto, M. & Alavian, S. M. Hepatitis delta: the rediscovery. *Clinics in liver disease* **17**, 475-487, doi:10.1016/j.cld.2013.05.007 (2013).

17 Rizzetto, M. & Ciancio, A. Epidemiology of hepatitis D. *Seminars in liver disease* **32**, 211-219, doi:10.1055/s-0032-1323626 (2012).

18 Farci, P. & Niro, G. A. Clinical features of hepatitis D. *Seminars in liver disease* **32**, 228-236, doi:10.1055/s-0032-1323628 (2012).

19 Shepard, C. W., Finelli, L. & Alter, M. J. Global epidemiology of hepatitis C virus infection. *The Lancet. Infectious diseases* **5**, 558-567, doi:10.1016/s1473-3099(05)70216-4 (2005).

20 Gower, E., Estes, C., Blach, S., Razavi-Shearer, K. & Razavi, H. Global epidemiology and genotype distribution of the hepatitis C virus infection. *Journal of hepatology* **61**, S45-57, doi:10.1016/j.jhep.2014.07.027 (2014).
21 Baffy, G., Brunt, E. M. & Caldwell, S. H. Hepatocellular carcinoma in non-alcoholic fatty liver disease: an emerging menace. *Journal of hepatology* **56**, 1384-1391, doi:10.1016/j.jhep.2011.10.027 (2012).
22 Zoulim, F. *et al.* Hepatitis C virus treatment in the real world: optimising treatment and access to therapies. *Gut* **64**, 1824-1833, doi:10.1136/gutjnl-2015-310421 (2015).
23 Byrne, C. D. & Targher, G. NAFLD: a multisystem disease. *Journal of hepatology* **62**, S47-64, doi:10.1016/j.jhep.2014.12.012 (2015).
24 Wree, A., Broderick, L., Canbay, A., Hoffman, H. M. & Feldstein, A. E. From NAFLD to NASH to cirrhosis-new insights into disease mechanisms. *Nat Rev Gastroenterol Hepatol* **10**, 627-636, doi:10.1038/nrgastro.2013.149 (2013).
25 Ertle, J. *et al.* Non-alcoholic fatty liver disease progresses to hepatocellular carcinoma in the absence of apparent cirrhosis. *International journal of cancer* **128**, 2436-2443, doi:10.1002/ijc.25797 (2011).
26 Tilg, H. & Moschen, A. R. Evolution of inflammation in nonalcoholic fatty liver disease: the multiple parallel hits hypothesis. *Hepatology (Baltimore, Md.)* **52**, 1836-1846, doi:10.1002/hep.24001 (2010).
27 Netdoctor. *Alcoholic liver disease*, <http://www.netdoctor.co.uk/conditions/liver-kidney-and-urinary-system/a5008/alcoholic-liver-disease/> (2010).
28 Bellentani, S. *et al.* Drinking habits as cofactors of risk for alcohol induced liver damage. The Dionysos Study Group. *Gut* **41**, 845-850 (1997).
29 Heneghan, M. A., Yeoman, A. D., Verma, S., Smith, A. D. & Longhi, M. S. Autoimmune hepatitis. *Lancet (London, England)* **382**, 1433-1444, doi:10.1016/s0140-6736(12)62163-1 (2013).
30 Selmi, C. *et al.* Primary biliary cirrhosis in monozygotic and dizygotic twins: genetics, epigenetics, and environment. *Gastroenterology* **127**, 485-492 (2004).
31 Lazaridis, K. N. *et al.* Increased prevalence of antimitochondrial antibodies in first-degree relatives of patients with primary biliary cirrhosis. *Hepatology (Baltimore, Md.)* **46**, 785-792, doi:10.1002/hep.21749 (2007).
32 Karlsen, T. H. & Boberg, K. M. Update on primary sclerosing cholangitis. *Journal of hepatology* **59**, 571-582, doi:10.1016/j.jhep.2013.03.015 (2013).
33 Bosch, J., Garcia-Pagan, J. C., Berzigotti, A. & Abraldes, J. G. Measurement of portal pressure and its role in the management of chronic liver disease. *Seminars in liver disease* **26**, 348-362, doi:10.1055/s-2006-951603 (2006).
34 Mehal, W. Z., Iredale, J. & Friedman, S. L. Scraping fibrosis: expressway to the core of fibrosis. *Nature medicine* **17**, 552-553, doi:10.1038/nm0511-552 (2011).
35 Novo, E. & Parola, M. Redox mechanisms in hepatic chronic wound healing and fibrogenesis. *Fibrogenesis Tissue Repair* **1**, 5, doi:10.1186/1755-1536-1-5 (2008).
36 Casini, A., Cunningham, M., Rojkind, M. & Lieber, C. S. Acetaldehyde increases procollagen type I and fibronectin gene transcription in cultured rat fat-storing cells through a protein synthesis-dependent mechanism. *Hepatology (Baltimore, Md.)* **13**, 758-765 (1991).
37 Casini, A. *et al.* Neutrophil-derived superoxide anion induces lipid peroxidation and stimulates collagen synthesis in human hepatic stellate cells: role of nitric oxide. *Hepatology (Baltimore, Md.)* **25**, 361-367, doi:10.1053/jhep.1997.v25.pm0009021948 (1997).

38 Parola, M. *et al.* HNE interacts directly with JNK isoforms in human hepatic stellate cells. *J Clin Invest* **102**, 1942-1950, doi:10.1172/jci1413 (1998).
39 Pinzani, M. Pathophysiology of Liver Fibrosis. *Digestive diseases (Basel, Switzerland)* **33**, 492-497, doi:10.1159/000374096 (2015).
40 Dr Steve Pereira, D. H. R., Dr Simon Bramhall. Liver cancer. Fighting liver diseade. *British Liver Trust* (2011).
41 Gastroenterology, B. S. o. <http://www.bsg.org.uk/clinical/commissioning-report/management-of-patients-with-chronic-liver-diseases.html> (2014).
42 Li, W. X., Li, Z., Gao, P. J., Gao, J. & Zhu, J. Y. Histological differentiation predicts post-liver transplantation survival time. *Clinics and Research in Hepatology and Gastroenterology* **38**, 201-208, doi:10.1016/j.clinre.2013.11.002 (2014).
43 NHS. *Liver Transplant*, <http://www.nhs.uk/Conditions/Liver-transplant/Pages/Introduction.aspx> (2014).
44 Shupe, T., Williams, M., Brown, A., Willenberg, B. & Petersen, B. E. Method for the decellularization of intact rat liver. *Organogenesis* **6**, 134-136 (2010).
45 Uygun, B. E. *et al.* Organ reengineering through development of a transplantable recellularized liver graft using decellularized liver matrix. *Nature medicine* **16**, 814-820, doi:10.1038/nm.2170 (2010).
46 Baptista, P. M. *et al.* The use of whole organ decellularization for the generation of a vascularized liver organoid. *Hepatology (Baltimore, Md.)* **53**, 604-617, doi:10.1002/hep.24067 (2011).
47 Barakat, O. *et al.* Use of Decellularized Porcine Liver for Engineering Humanized Liver Organ. *Journal of Surgical Research* **173**, E11-E25, doi:10.1016/j.jss.2011.09.033 (2012).
48 Kunz-Schughart, L. A., Freyer, J. P., Hofstaedter, F. & Ebner, R. The use of 3-D cultures for high-throughput screening: The multicellular spheroid model. *Journal of Biomolecular Screening* **9**, 273-285, doi:10.1177/1087057104265040 (2004).
49 Breslin, S. & O'Driscoll, L. Three-dimensional cell culture: the missing link in drug discovery. *Drug discovery today* **18**, 240-249, doi:10.1016/j.drudis.2012.10.003 (2013).
50 Schuetz, E. G. *et al.* REGULATION OF GENE-EXPRESSION IN ADULT-RAT HEPATOCYTES CULTURED ON A BASEMENT-MEMBRANE MATRIX. *Journal of Cellular Physiology* **134**, 309-323, doi:10.1002/jcp.1041340302 (1988).
51 Dunn, J. C., Tompkins, R. G. & Yarmush, M. L. Long-term in vitro function of adult hepatocytes in a collagen sandwich configuration. *Biotechnology progress* **7**, 237-245, doi:10.1021/bp00009a007 (1991).
52 Tchaparian, E. H., Houghton, J. S., Uyeda, C., Grillo, M. P. & Jin, L. Effect of culture time on the basal expression levels of drug transporters in sandwich-cultured primary rat hepatocytes. *Drug metabolism and disposition: the biological fate of chemicals* **39**, 2387-2394, doi:10.1124/dmd.111.039545 (2011).
53 Kotani, N. *et al.* Culture period-dependent changes in the uptake of transporter substrates in sandwich-cultured rat and human hepatocytes. *Drug metabolism and disposition: the biological fate of chemicals* **39**, 1503-1510, doi:10.1124/dmd.111.038968 (2011).
54 Birgersdotter, A., Sandberg, R. & Ernberg, I. Gene expression perturbation in vitro - A growing case for three-dimensional (3D) culture systems. *Seminars in Cancer Biology* **15**, 405-412, doi:10.1016/j.semcancer.2005.06.009 (2005).
55 Bhadriraju, K. & Chen, C. S. Engineering cellular microenvironments to improve cell-based drug testing. *Drug discovery today* **7**, 612-620 (2002).

56 Nussler, A. K. *et al.* The suitability of hepatocyte culture models to study various aspects of drug metabolism. *Altex-Alternativen Zu Tierexperimenten* **18**, 91-101 (2001).
57 Horning, J. L. *et al.* 3-D tumor model for in vitro evaluation of anticancer drugs. *Molecular Pharmaceutics* **5**, 849-862, doi:10.1021/mp800047v (2008).
58 Stokes, W. S. & Annals, N. Y. A. S. Best practices for the use of animals in toxicological research and testing. *Animal Models: Their Value in Predicting Drug Efficacy and Toxicity* **1245**, 17-20, doi:10.1111/j.1749-6632.2011.06334.x (2011).
59 Morgan, E. T. Regulation of hepatic drug metabolizing enzymes in animal models of infectious and inflammatory diseases. *Drug Metabolism Reviews* **38**, 19-19 (2006).
60 Abass, K., Reponen, P., Mattila, S., Rautio, A. & Pelkonen, O. Comparative metabolism of benfuracarb in in vitro mammalian hepatic microsomes model and its implications for chemical risk assessment. *Toxicology Letters* **224**, 290-299, doi:10.1016/j.toxlet.2013.08.009 (2014).
61 Smith, D. A. Species differences in metabolism and pharmacokinetics: are we close to an understanding? *Drug Metab Rev* **23**, 355-373, doi:10.3109/03602539109029764 (1991).
62 Edmondson, R., Broglie, J. J., Adcock, A. F. & Yang, L. J. Three-Dimensional Cell Culture Systems and Their Applications in Drug Discovery and Cell-Based Biosensors. *Assay and Drug Development Technologies* **12**, 207-218, doi:10.1089/adt.2014.573 (2014).
63 Kola, I. The state of innovation in drug development. *Clinical Pharmacology & Therapeutics* **83**, 227-230, doi:10.1038/sj.clpt.6100479 (2008).
64 Marga, F., Neagu, A., Kosztin, I. & Forgacs, G. Developmental biology and tissue engineering. *Birth Defects Research* **81**, 320-328, doi:10.1002/bdrc.20109 (2007).
65 Lee, J., Cuddihy, M. J. & Kotov, N. A. Three-dimensional cell culture matrices: State of the art. *Tissue Engineering Part B-Reviews* **14**, 61-86, doi:10.1089/teb.2007.0150 (2008).
66 Zietarska, M. *et al.* Molecular description of a 3D in vitro model for the study of epithelial ovarian cancer (EOC). *Molecular Carcinogenesis* **46**, 872-885, doi:10.1002/mc.20315 (2007).
67 O'Brien, L. E., Zegers, M. M. P. & Mostov, K. E. Opinion - Building epithelial architecture: insights from three-dimensional culture models. *Nature Reviews Molecular Cell Biology* **3**, 531-537, doi:10.1038/nrm859 (2002).
68 Kim, Y. & Rajagopalan, P. 3D Hepatic Cultures Simultaneously Maintain Primary Hepatocyte and Liver Sinusoidal Endothelial Cell Phenotypes. *Plos One* **5**, doi:10.1371/journal.pone.0015456 (2010).
69 Lee, S. A. *et al.* Spheroid-based three-dimensional liver-on-a-chip to investigate hepatocyte-hepatic stellate cell interactions and flow effects. *Lab on a Chip* **13**, 3529-3537, doi:10.1039/c3lc50197c (2013).
70 Gumbiner, B. M. Regulation of cadherin-mediated adhesion in morphogenesis. *Nature Reviews Molecular Cell Biology* **6**, 622-634, doi:10.1038/nrm1699 (2005).
71 Nagai, H. *et al.* Differentiation of liver epithelial (stem-like) cells into hepatocytes induced by coculture with hepatic stellate cells. *Biochemical and Biophysical Research Communications* **293**, 1420-1425, doi:10.1016/s0006-291x(02)00406-0 (2002).
72 Pan, K., Zhou, H., Zhang, Z., Gao, Y. & Xu, X. Evaluation of co-cultured CL-1 hepatocytes and hepatic stellate cells in rotatory cell culture system. *Nan fang yi ke da xue xue bao = Journal of Southern Medical University* **33** (2013).

73 Kasuya, J., Sudo, R., Mitaka, T., Ikeda, M. & Tanishita, K. Hepatic Stellate Cell-Mediated Three-Dimensional Hepatocyte and Endothelial Cell Triculture Model. *Tissue Engineering Part A* **17**, 361-370, doi:10.1089/ten.tea.2010.0033 (2011).
74 Larsen, M., Artym, V. V., Green, J. A. & Yamada, K. M. The matrix reorganized: extracellular matrix remodeling and integrin signaling. *Current Opinion in Cell Biology* **18**, 463-471, doi:10.1016/j.ceb.2006.08.009 (2006).
75 Cukierman, E., Pankov, R. & Yamada, K. M. Cell interactions with three-dimensional matrices. *Curr Opin Cell Biol* **14**, 633-639 (2002).
76 Cukierman, E., Pankov, R., Stevens, D. R. & Yamada, K. M. Taking cell-matrix adhesions to the third dimension. *Science* **294**, 1708-1712, doi:10.1126/science.1064829 (2001).
77 Hynes, R. O. Integrins: Bidirectional, allosteric signaling machines. *Cell* **110**, 673-687, doi:10.1016/s0092-8674(02)00971-6 (2002).
78 Qin, J., Vinogradova, O. & Plow, E. F. Integrin bidirectional signaling: a molecular view. *Plos Biology* **2**, 726-729, doi:10.1371/journal.pbio.0020169 (2004).
79 Legate, K. R., Wickstroem, S. A. & Faessler, R. Genetic and cell biological analysis of integrin outside-in signaling. *Genes & Development* **23**, 397-418, doi:10.1101/gad.1758709 (2009).
80 Pelham, R. J., Jr. & Wang, Y. L. Cell locomotion and focal adhesions are regulated by the mechanical properties of the substrate. *The Biological bulletin* **194**, 348-349; discussion 349-350 (1998).
81 Geiger, B., Bershadsky, A., Pankov, R. & Yamada, K. M. Transmembrane extracellular matrix-cytoskeleton crosstalk. *Nature Reviews Molecular Cell Biology* **2**, 793-805, doi:10.1038/35099066 (2001).
82 Bissell, M. J., Radisky, D. C., Rizki, A., Weaver, V. M. & Petersen, O. W. The organizing principle: microenvironmental influences in the normal and malignant breast. *Differentiation* **70**, 537-546, doi:10.1046/j.1432-0436.2002.700907.x (2002).
83 Astashkina, A., Mann, B. & Grainger, D. W. A critical evaluation of in vitro cell culture models for high-throughput drug screening and toxicity. *Pharmacology & Therapeutics* **134**, 82-106, doi:10.1016/j.pharmthera.2012.01.001 (2012).
84 Kaully, T., Kaufman-Francis, K., Lesman, A. & Levenberg, S. Vascularization-The Conduit to Viable Engineered Tissues. *Tissue Engineering Part B-Reviews* **15**, 159-169, doi:10.1089/ten.teb.2008.0193 (2009).
85 Kellner, K. *et al.* Determination of oxygen gradients in engineered tissue using a fluorescent sensor. *Biotechnology and Bioengineering* **80**, 73-83, doi:10.1002/bit.10352 (2002).
86 Griffith, L. G. & Swartz, M. A. Capturing complex 3D tissue physiology in vitro. *Nature Reviews Molecular Cell Biology* **7**, 211-224, doi:10.1038/nrm1858 (2006).
87 Kim, K., Ohashi, K., Utoh, R., Kano, K. & Okano, T. Preserved liver-specific functions of hepatocytes in 3D co-culture with endothelial cell sheets. *Biomaterials* **33**, 1406-1413, doi:10.1016/j.biomaterials.2011.10.084 (2012).
88 Landry, J., Bernier, D., Ouellet, C., Goyette, R. & Marceau, N. SPHEROIDAL AGGREGATE CULTURE OF RAT-LIVER CELLS - HISTOTYPIC REORGANIZATION, BIOMATRIX DEPOSITION, AND MAINTENANCE OF FUNCTIONAL ACTIVITIES. *Journal of Cell Biology* **101**, 914-923, doi:10.1083/jcb.101.3.914 (1985).
89 Fennema, E., Rivron, N., Rouwkema, J., van Blitterswijk, C. & de Boer, J. Spheroid culture as a tool for creating 3D complex tissues. *Trends in Biotechnology* **31**, 108-115, doi:10.1016/j.tibtech.2012.12.003 (2013).

90 Tostoes, R. M. *et al.* Human liver cell spheroids in extended perfusion bioreactor culture for repeated-dose drug testing. *Hepatology (Baltimore, Md.)* **55**, 1227-1236, doi:10.1002/hep.24760 (2012).
91 Kobayashi, A. *et al.* REGULATION OF DIFFERENTIATION AND PROLIFERATION OF RAT HEPATOCYTES BY LACTOSE-CARRYING POLYSTYRENE. *Artificial Organs* **16**, 564-567 (1992).
92 Drewitz, M. *et al.* Towards automated production and drug sensitivity testing using scaffold-free spherical tumor microtissues. *Biotechnology Journal* **6**, 1488-1496, doi:10.1002/biot.201100290 (2011).
93 Tsuda, Y. *et al.* The use of patterned dual thermoresponsive surfaces for the collective recovery as co-cultured cell sheets. *Biomaterials* **26**, 1885-1893, doi:10.1016/j.biomaterials.2004.06.005 (2005).
94 Tsang, V. L. *et al.* Fabrication of 3D hepatic tissues by additive photopatterning of cellular hydrogels. *Faseb Journal* **21**, 790-801, doi:10.1096/fj.06-7117com (2007).
95 Rimann, M. & Graf-Hausner, U. Synthetic 3D multicellular systems for drug development. *Current Opinion in Biotechnology* **23**, 803-809, doi:10.1016/j.copbio.2012.01.011 (2012).
96 Miranda, J. P. *et al.* Extending hepatocyte functionality for drug-testing applications using high-viscosity alginate-encapsulated three-dimensional cultures in bioreactors. *Tissue engineering. Part C, Methods* **16**, 1223-1232, doi:10.1089/ten.TEC.2009.0784 (2010).
97 Janiak, M., Hashmi, H. R. & Janowskawieczorek, A. Use of the matrigel-based assay to measure the invasiveness of leukemic-cells. *Experimental Hematology* **22**, 559-565 (1994).
98 Celiz, A. D. *et al.* Materials for stem cell factories of the future. *Nature Materials* **13**, 570-579, doi:10.1038/nmat3972 (2014).
99 Skardal, A. *et al.* Tissue specific synthetic ECM hydrogels for 3-D in vitro maintenance of hepatocyte function. *Biomaterials* **33**, 4565-4575, doi:10.1016/j.biomaterials.2012.03.034 (2012).
100 Lee, J. S. *et al.* Liver Extracellular Matrix Providing Dual Functions of Two-Dimensional Substrate Coating and Three-Dimensional Injectable Hydrogel Platform for Liver Tissue Engineering. *Biomacromolecules* **15**, 206-218, doi:10.1021/bm4015039 (2014).
101 Flynn, L. E. The use of decellularized adipose tissue to provide an inductive microenvironment for the adipogenic differentiation of human adipose-derived stem cells. *Biomaterials* **31**, 4715-4724, doi:10.1016/j.biomaterials.2010.02.046 (2010).
102 Cortiella, J. *et al.* Influence of acellular natural lung matrix on murine embryonic stem cell differentiation and tissue formation. *Tissue engineering. Part A* **16**, 2565-2580, doi:10.1089/ten.tea.2009.0730 (2010).
103 Cartmell, J. S. & Dunn, M. G. Effect of chemical treatments on tendon cellularity and mechanical properties. *Journal of biomedical materials research* **49**, 134-140 (2000).
104 Burk, J. *et al.* Freeze-thaw cycles enhance decellularization of large tendons. *Tissue engineering. Part C, Methods* **20**, 276-284, doi:10.1089/ten.TEC.2012.0760 (2014).
105 Jackson, D. W., Grood, E. S., Arnoczky, S. P., Butler, D. L. & Simon, T. M. Cruciate reconstruction using freeze dried anterior cruciate ligament allograft and a ligament augmentation device (LAD). An experimental study in a goat model. *The American journal of sports medicine* **15**, 528-538 (1987).

106 Szynkaruk, M., Kemp, S. W., Wood, M. D., Gordon, T. & Borschel, G. H. Experimental and clinical evidence for use of decellularized nerve allografts in peripheral nerve gap reconstruction. *Tissue engineering. Part B, Reviews* **19**, 83-96, doi:10.1089/ten.TEB.2012.0275 (2013).
107 Prasertsung, I., Kanokpanont, S., Bunaprasert, T., Thanakit, V. & Damrongsakkul, S. Development of acellular dermis from porcine skin using periodic pressurized technique. *Journal of biomedical materials research. Part B, Applied biomaterials* **85**, 210-219, doi:10.1002/jbm.b.30938 (2008).
108 Hopkinson, A. *et al.* Optimization of amniotic membrane (AM) denuding for tissue engineering. *Tissue engineering. Part C, Methods* **14**, 371-381, doi:10.1089/ten.tec.2008.0315 (2008).
109 Dahl, S. L., Koh, J., Prabhakar, V. & Niklason, L. E. Decellularized native and engineered arterial scaffolds for transplantation. *Cell transplantation* **12**, 659-666 (2003).
110 Woods, T. & Gratzer, P. F. Effectiveness of three extraction techniques in the development of a decellularized bone-anterior cruciate ligament-bone graft. *Biomaterials* **26**, 7339-7349, doi:10.1016/j.biomaterials.2005.05.066 (2005).
111 Goissis, G. *et al.* Preparation and characterization of collagen-elastin matrices from blood vessels intended as small diameter vascular grafts. *Artificial organs* **24**, 217-223 (2000).
112 De Filippo, R. E., Yoo, J. J. & Atala, A. Urethral Replacement Using Cell Seeded Tubularized Collagen Matrices. *The Journal of Urology* **168**, 1789-1793, doi:http://dx.doi.org/10.1016/S0022-5347(05)64414-X (2002).
113 Rosario, D. J. *et al.* Decellularization and sterilization of porcine urinary bladder matrix for tissue engineering in the lower urinary tract. *Regenerative medicine* **3**, 145-156, doi:10.2217/17460751.3.2.145 (2008).
114 DeQuach, J. A., Yuan, S. H., Goldstein, L. S. & Christman, K. L. Decellularized porcine brain matrix for cell culture and tissue engineering scaffolds. *Tissue engineering. Part A* **17**, 2583-2592, doi:10.1089/ten.TEA.2010.0724 (2011).
115 Christman, K. L. & Young, D. A. (Google Patents, 2012).
116 Everaerts, F. J. L., Torrianni, M. W., Everaerts, F. M., Trescony, P. V. & den Hartog, W. (Google Patents, 2013).
117 Klebe, R. J. Cell attachment to collagen: the requirement for energy. *Journal of cellular physiology* **86**, 231-236, doi:10.1002/jcp.1040860206 (1975).
118 Seddon, A. M., Curnow, P. & Booth, P. J. Membrane proteins, lipids and detergents: not just a soap opera. *Biochimica et biophysica acta* **1666**, 105-117, doi:10.1016/j.bbamem.2004.04.011 (2004).
119 Grauss, R. W. *et al.* Histological evaluation of decellularised porcine aortic valves: matrix changes due to different decellularisation methods. *European Journal of Cardio-Thoracic Surgery* **27**, 566-571, doi:10.1016/j.ejcts.2004.12.052 (2005).
120 Nari, G. A. *et al.* Preparation of a three-dimensional extracellular matrix by decellularization of rabbit livers. *Revista espanola de enfermedades digestivas : organo oficial de la Sociedad Espanola de Patologia Digestiva* **105**, 138-143 (2013).
121 Rieder, E. *et al.* Decellularization protocols of porcine heart valves differ importantly in efficiency of cell removal and susceptibility of the matrix to recellularization with human vascular cells. *The Journal of thoracic and cardiovascular surgery* **127**, 399-405, doi:10.1016/j.jtcvs.2003.06.017 (2004).

122 Chen, R. N., Ho, H. O., Tsai, Y. T. & Sheu, M. T. Process development of an acellular dermal matrix (ADM) for biomedical applications. *Biomaterials* **25**, 2679-2686 (2004).
123 Hudson, T. W., Liu, S. Y. & Schmidt, C. E. Engineering an improved acellular nerve graft via optimized chemical processing. *Tissue engineering* **10**, 1346-1358, doi:10.1089/ten.2004.10.1346 (2004).
124 Lin, P., Chan, W. C., Badylak, S. F. & Bhatia, S. N. Assessing porcine liver-derived biomatrix for hepatic tissue engineering. *Tissue engineering* **10**, 1046-1053, doi:10.1089/ten.2004.10.1046 (2004).
125 Ketchedjian, A. *et al.* Recellularization of decellularized allograft scaffolds in ovine great vessel reconstructions. *The Annals of thoracic surgery* **79**, 888-896; discussion 896, doi:10.1016/j.athoracsur.2004.09.033 (2005).
126 Hudson, T. W. *et al.* Optimized acellular nerve graft is immunologically tolerated and supports regeneration. *Tissue engineering* **10**, 1641-1651, doi:10.1089/ten.2004.10.1641 (2004).
127 Liao, J., Joyce, E. M. & Sacks, M. S. Effects of decellularization on the mechanical and structural properties of the porcine aortic valve leaflet. *Biomaterials* **29**, 1065-1074, doi:10.1016/j.biomaterials.2007.11.007 (2008).
128 Guyette, J., Gilpin, S. E., Charest, J. M. & Tapias, L. F. Perfusion decellularization of whole organs. *Nature Protocols* **9**, 1451-1468 (2014).
129 Jensen, T. *et al.* A rapid lung de-cellularization protocol supports embryonic stem cell differentiation in vitro and following implantation. *Tissue engineering. Part C, Methods* **18**, 632-646, doi:10.1089/ten.TEC.2011.0584 (2012).
130 Petersen, T. H., Calle, E. A., Colehour, M. B. & Niklason, L. E. Matrix composition and mechanics of decellularized lung scaffolds. *Cells, tissues, organs* **195**, 222-231, doi:10.1159/000324896 (2012).
131 Gilbert, T. W., Sellaro, T. L. & Badylak, S. F. Decellularization of tissues and organs. *Biomaterials* **27**, 3675-3683, doi:10.1016/j.biomaterials.2006.02.014 (2006).
132 Pierschbacher, M. D., Grzesiak, J. J. & Kirchhofer, D. (Google Patents, 1998).
133 Bader, A. *et al.* Tissue engineering of heart valves--human endothelial cell seeding of detergent acellularized porcine valves. *European journal of cardio-thoracic surgery : official journal of the European Association for Cardio-thoracic Surgery* **14**, 279-284 (1998).
134 Gamba, P. G. *et al.* Experimental abdominal wall defect repaired with acellular matrix. *Pediatric surgery international* **18**, 327-331, doi:10.1007/s00383-002-0849-5 (2002).
135 McFetridge, P. S., Daniel, J. W., Bodamyali, T., Horrocks, M. & Chaudhuri, J. B. Preparation of porcine carotid arteries for vascular tissue engineering applications. *Journal of biomedical materials research. Part A* **70**, 224-234, doi:10.1002/jbm.a.30060 (2004).
136 Nonaka, P. N. *et al.* Effects of freezing/thawing on the mechanical properties of decellularized lungs. *Journal of biomedical materials research. Part A* **102**, 413-419, doi:10.1002/jbm.a.34708 (2014).
137 Brendel, K. & Duhamel, R. C. (Google Patents, 1989).
138 Bishopric, N. H., Dousman, L. & Yao, Y. M. (Google Patents, 1999).
139 Gleason, K. *How to convert Centrifuge RPM to RCF or G-force*, 2012).
140 Elder, B. D., Eleswarapu, S. V. & Athanasiou, K. A. Extraction techniques for the decellularization of tissue engineered articular cartilage constructs. *Biomaterials* **30**, 3749-3756, doi:10.1016/j.biomaterials.2009.03.050 (2009).

141 Schenke-Layland, K. *et al.* Impact of decellularization of xenogeneic tissue on extracellular matrix integrity for tissue engineering of heart valves. *Journal of structural biology* **143**, 201-208 (2003).
142 Steinhoff, G. *et al.* Tissue engineering of pulmonary heart valves on allogenic acellular matrix conduits: in vivo restoration of valve tissue. *Circulation* **102**, Iii50-55 (2000).
143 Fitzpatrick, J. C., Clark, P. M. & Capaldi, F. M. Effect of Decellularization Protocol on the Mechanical Behavior of Porcine Descending Aorta. *International Journal of Biomaterials* **2010**, 11, doi:10.1155/2010/620503 (2010).
144 Takami, Y. (Google Patents, 2005).
145 Hung, S. H., Su, C. H., Lee, F. P. & Tseng, H. Larynx decellularization: combining freeze-drying and sonication as an effective method. *Journal of voice : official journal of the Voice Foundation* **27**, 289-294, doi:10.1016/j.jvoice.2013.01.018 (2013).
146 Azhim, A., Syazwani, N., Morimoto, Y., Furukawa, K. & Ushida, T. The use of sonication treatment to decellularize aortic tissues for preparation of bioscaffolds. *Journal of biomaterials applications* **29**, 130-141, doi:10.1177/0885328213517579 (2014).
147 Azhim, A., Yamagami, K., Muramatsu, K., Morimoto, Y. & Tanaka, M. The use of sonication treatment to completely decellularize blood arteries: a pilot study. *Conference proceedings : ... Annual International Conference of the IEEE Engineering in Medicine and Biology Society. IEEE Engineering in Medicine and Biology Society. Conference* **2011**, 2468-2471, doi:10.1109/iembs.2011.6090685 (2011).
148 Oliveira, A. C. *et al.* Evaluation of small intestine grafts decellularization methods for corneal tissue engineering. *PloS one* **8**, e66538, doi:10.1371/journal.pone.0066538 (2013).
149 Sarig, U. *et al.* Thick acellular heart extracellular matrix with inherent vasculature: a potential platform for myocardial tissue regeneration. *Tissue engineering. Part A* **18**, 2125-2137, doi:10.1089/ten.TEA.2011.0586 (2012).
150 Hodde, J. P., Badylak, S. F., Brightman, A. O. & Voytik-Harbin, S. L. Glycosaminoglycan content of small intestinal submucosa: a bioscaffold for tissue replacement. *Tissue engineering* **2**, 209-217, doi:10.1089/ten.1996.2.209 (1996).
151 Crapo, P. M., Gilbert, T. W. & Badylak, S. F. An overview of tissue and whole organ decellularization processes. *Biomaterials* **32**, 3233-3243, doi:10.1016/j.biomaterials.2011.01.057 (2011).
152 Yang, B. *et al.* Development of a porcine bladder acellular matrix with well-preserved extracellular bioactive factors for tissue engineering. *Tissue engineering. Part C, Methods* **16**, 1201-1211, doi:10.1089/ten.TEC.2009.0311 (2010).
153 Meezan, E., Hjelle, J. T., Brendel, K. & Carlson, E. C. A simple, versatile, nondisruptive method for the isolation of morphologically and chemically pure basement membranes from several tissues. *Life sciences* **17**, 1721-1732 (1975).
154 Ott, H. C. *et al.* Perfusion-decellularized matrix: using nature's platform to engineer a bioartificial heart. *Nature medicine* **14**, 213-221, doi:10.1038/nm1684 (2008).
155 Song, J. J. *et al.* Regeneration and experimental orthotopic transplantation of a bioengineered kidney. *Nature medicine* **19**, 646-651, doi:10.1038/nm.3154 (2013).

156 Mazza, G. *et al.* Decellularized human liver as a natural 3D-scaffold for liver bioengineering and transplantation. *Scientific reports* **5**, 13079, doi:10.1038/srep13079 (2015).
157 Murray, C. J. & Lopez, A. D. Measuring the global burden of disease. *The New England journal of medicine* **369**, 448-457, doi:10.1056/NEJMra1201534 (2013).
158 BASL & BSG. A Time Act: Improving Liver Health and Outcomes in Liver Disease (2009).
159 Dutkowski, P. *et al.* The model for end-stage liver disease allocation system for liver transplantation saves lives, but increases morbidity and cost: a prospective outcome analysis. *Liver transplantation : official publication of the American Association for the Study of Liver Diseases and the International Liver Transplantation Society* **17**, 674-684, doi:10.1002/lt.22228 (2011).
160 Brown, K. A. Liver transplantation. *Curr Opin Gastroenterol* **21**, 331-336 (2005).
161 Busuttil, R. W. & Tanaka, K. The utility of marginal donors in liver transplantation. *Liver Transpl.* **9**, 651-663, doi:10.1053/jlts.2003.50105 (2003).
162 Fox, I. J. *et al.* Treatment of the Crigler-Najjar syndrome type I with hepatocyte transplantation. *N. Engl. J. Med.* **338**, 1422-1426, doi:10.1056/nejm199805143382004 (1998).
163 Dhawan, A. *et al.* Hepatocyte transplantation for inherited factor VII deficiency. *Transplantation* **78**, 1812-1814 (2004).
164 Muraca, M. *et al.* Hepatocyte transplantation as a treatment for glycogen storage disease type 1a. *Lancet* **359**, 317-318, doi:10.1016/s0140-6736(02)07529-3 (2002).
165 Sokal, E. M. *et al.* Hepatocyte transplantation in a 4-year-old girl with peroxisomal biogenesis disease: technique, safety, and metabolic follow-up. *Transplantation* **76**, 735-738, doi:10.1097/01.tp.0000077420.81365.53 (2003).
166 Horslen, S. P. *et al.* Isolated hepatocyte transplantation in an infant with a severe urea cycle disorder. *Pediatrics* **111**, 1262-1267 (2003).
167 Struecker, B., Raschzok, N. & Sauer, I. M. Liver support strategies: cutting-edge technologies. *Nat Rev Gastroenterol Hepatol* **11**, 166-176, doi:10.1038/nrgastro.2013.204 (2014).
168 Muerza-Cascante, M. L., Haylock, D., Hutmacher, D. W. & Dalton, P. D. Melt electrospinning and its technologization in tissue engineering. *Tissue engineering. Part B, Reviews* **21**, 187-202, doi:10.1089/ten.TEB.2014.0347 (2015).
169 Mandrycky, C., Wang, Z., Kim, K. & Kim, D. H. 3D bioprinting for engineering complex tissues. *Biotechnology advances*, doi:10.1016/j.biotechadv.2015.12.011 (2015).
170 Badylak, S. F. The extracellular matrix as a scaffold for tissue reconstruction. *Seminars in cell & developmental biology* **13**, 377-383 (2002).
171 Ren, H. *et al.* Evaluation of two decellularization methods in the development of a whole-organ decellularized rat liver scaffold. *Liver Int* **33**, 448-458, doi:10.1111/liv.12088 (2013).
172 Pan, M. X. *et al.* An efficient method for decellularization of the rat liver. *J. Formos. Med. Assoc.* **113**, 680-687, doi:10.1016/j.jfma.2013.05.003 (2014).
173 Kajbafzadeh, A. M., Javan-Farazmand, N., Monajemzadeh, M. & Baghayee, A. Determining the optimal decellularization and sterilization protocol for preparing a tissue scaffold of a human-sized liver tissue. *Tissue Eng Part C Methods* **19**, 642-651, doi:10.1089/ten.TEC.2012.0334 (2013).

174 Wang, Y. *et al.* Lineage restriction of human hepatic stem cells to mature fates is made efficient by tissue-specific biomatrix scaffolds. *Hepatology (Baltimore, Md.)* **53**, 293-305, doi:10.1002/hep.24012 (2011).
175 Soto-Gutierrez, A. *et al.* A whole-organ regenerative medicine approach for liver replacement. *Tissue engineering. Part C, Methods* **17**, 677-686, doi:10.1089/ten.tec.2010.0698 (2011).
176 Barakat, O. *et al.* Use of decellularized porcine liver for engineering humanized liver organ. *J. Surg. Res.* **173**, e11-25, doi:10.1016/j.jss.2011.09.033 (2012).
177 Totonelli, G. *et al.* A rat decellularized small bowel scaffold that preserves villus-crypt architecture for intestinal regeneration. *Biomaterials* **33**, 3401-3410, doi:10.1016/j.biomaterials.2012.01.012 (2012).
178 Quint, C. *et al.* Decellularized tissue-engineered blood vessel as an arterial conduit. *Proceedings of the National Academy of Sciences* **108**, 9214-9219, doi:10.1073/pnas.1019506108 (2011).
179 Halliday, P., Sheil, A. G. R., Bookllil, M. J. & Gaudry, P. L. Preparation of the Porcine Liver for Allotransplantation. *Aust. N. Z. J. Surg.* **40**, 374-380, doi:10.1111/j.1445-2197.1971.tb04097.x (1971).
180 Baptista, P. M., Vyas, D., Moran, E., Wang, Z. & Soker, S. Human liver bioengineering using a whole liver decellularized bioscaffold. *Methods Mol. Biol.* **1001**, 289-298, doi:10.1007/978-1-62703-363-3_24 (2013).
181 Mirmalek-Sani, S. H., Sullivan, D. C., Zimmerman, C., Shupe, T. D. & Petersen, B. E. Immunogenicity of decellularized porcine liver for bioengineered hepatic tissue. *Am. J. Pathol.* **183**, 558-565, doi:10.1016/j.ajpath.2013.05.002 (2013).
182 Xu, L. *et al.* Human hepatic stellate cell lines, LX-1 and LX-2: new tools for analysis of hepatic fibrosis. *Gut* **54**, 142-151, doi:10.1136/gut.2004.042127 (2005).
183 Cheng, Y. *et al.* In vitro culture of tumour-derived hepatocytes in decellularised whole-liver biological scaffolds. *Digestion* **87**, 189-195, doi:10.1159/000349949 (2013).
184 Pan, T. L. *et al.* Network analysis and proteomic identification of vimentin as a key regulator associated with invasion and metastasis in human hepatocellular carcinoma cells. *J. Proteomics* **75**, 4676-4692, doi:10.1016/j.jprot.2012.02.017 (2012).
185 Mazza, G. *et al.* Amyloid persistence in decellularized liver: biochemical and histopathological characterization. *Amyloid : the international journal of experimental and clinical investigation : the official journal of the International Society of Amyloidosis*, 1-7, doi:10.3109/13506129.2015.1110518 (2015).
186 Pepys, M. B. Amyloidosis. *Annu. Rev. Med.* **57**, 223-241, doi:10.1146/annurev.med.57.121304.131243 (2006).
187 Bellotti, V. & Chiti, F. Amyloidogenesis in its biological environment: challenging a fundamental issue in protein misfolding diseases. *Curr. Opin. Struct. Biol.* **18**, 771-779, doi:10.1016/j.sbi.2008.10.001 (2008).
188 Bonsib, S. M. & Plattner, S. B. Acellular scanning electron microscopy of spicular renal amyloidosis. *Ultrastruct. Pathol.* **10**, 497-504 (1986).
189 Baptista, P. M. *et al.* The use of whole organ decellularization for the generation of a vascularized liver organoid. *Hepatology (Baltimore, Md.)* **53**, 604-617, doi:10.1002/hep.24067 (2011).
190 Guyette, J. P. *et al.* Perfusion decellularization of whole organs. *Nat. Protoc.* **9**, 1451-1468, doi:10.1038/nprot.2014.097 (2014).

191 Uygun, B. E. *et al.* Organ reengineering through development of a transplantable recellularized liver graft using decellularized liver matrix. *Nat. Med.* **16**, 814-820, doi:10.1038/nm.2170 (2010).
192 Mazza, G. *et al.* Decellularized human liver as a natural 3D-scaffold for liver bioengineering and transplantation. *Sci. Rep.* **5**, 13079, doi:10.1038/srep13079 (2015).
193 Badylak, S. F., Taylor, D. & Uygun, K. Whole-organ tissue engineering: decellularization and recellularization of three-dimensional matrix scaffolds. *Annu. Rev. Biomed. Eng.* **13**, 27-53, doi:10.1146/annurev-bioeng-071910-124743 (2011).
194 Maghsoudlou, P. *et al.* Preservation of micro-architecture and angiogenic potential in a pulmonary acellular matrix obtained using intermittent intra-tracheal flow of detergent enzymatic treatment. *Biomaterials* **34**, 6638-6648, doi:10.1016/j.biomaterials.2013.05.015 (2013).
195 Simons, J. P. *et al.* Pathogenetic mechanisms of amyloid A amyloidosis. *Proc. Natl. Acad. Sci. U.S.A.* **110**, 16115-16120, doi:10.1073/pnas.1306621110 (2013).
196 Puchtler, H., Waldrop, F. S. & Meloan, S. N. A review of light, polarization and fluorescence microscopic methods for amyloid. *Appl. Pathol.* **3**, 5-17 (1985).
197 Axelrad, M. A., Kisilevsky, R., Willmer, J., Chen, S. J. & Skinner, M. Further characterization of amyloid-enhancing factor. *Lab. Invest.* **47**, 139-146 (1982).
198 Hawkins, P. N., Wootton, R. & Pepys, M. B. Metabolic studies of radioiodinated serum amyloid P component in normal subjects and patients with systemic amyloidosis. *J. Clin. Invest.* **86**, 1862-1869, doi:10.1172/jci114917 (1990).
199 Botto, M. *et al.* Amyloid deposition is delayed in mice with targeted deletion of the serum amyloid P component gene. *Nat. Med.* **3**, 855-859 (1997).
200 Hawkins, P. N., Myers, M. J., Epenetos, A. A., Caspi, D. & Pepys, M. B. Specific localization and imaging of amyloid deposits in vivo using 123I-labeled serum amyloid P component. *J. Exp. Med.* **167**, 903-913 (1988).
201 Eriksen, N., Ericsson, L. H., Pearsall, N., Lagunoff, D. & Benditt, E. P. Mouse amyloid protein AA: Homology with nonimmunoglobulin protein of human and monkey amyloid substance. *Proc. Natl. Acad. Sci. U.S.A.* **73**, 964-967 (1976).
202 Baltz, M. L., Caspi, D., Hind, C. R. K., Feinstein, A. & Pepys, M. B. in *Amyloidosis* (eds G.G. Glenner *et al.*) Ch. 14, 115-121 (Springer US, 1986).
203 Garcia, C. A., Abell-Aleff, P. C., Gamb, S. I. & Miller, D. V. Ultrastructural analysis of amyloidoma. *Ultrastruct. Pathol.* **33**, 123-127, doi:10.1080/01913120902785468 (2009).
204 Totonelli, G. *et al.* A rat decellularized small bowel scaffold that preserves villus-crypt architecture for intestinal regeneration. *Biomaterials* **33**, 3401-3410, doi:10.1016/j.biomaterials.2012.01.012 (2012).
205 Richards, D. B. *et al.* Therapeutic Clearance of Amyloid by Antibodies to Serum Amyloid P Component. *The New England journal of medicine* **373**, 1106-1114, doi:10.1056/NEJMoa1504942 (2015).
206 Snow, A. D., Willmer, J. & Kisilevsky, R. Sulfated glycosaminoglycans: a common constituent of all amyloids? *Lab Invest* **56**, 120-123 (1987).
207 Stoppini, M. & Bellotti, V. Systemic amyloidosis: lessons from beta2-microglobulin. *The Journal of biological chemistry* **290**, 9951-9958, doi:10.1074/jbc.R115.639799 (2015).
208 Valleix, S. *et al.* Hereditary systemic amyloidosis due to Asp76Asn variant beta2-microglobulin. *The New England journal of medicine* **366**, 2276-2283, doi:10.1056/NEJMoa1201356 (2012).

209 Mangione, P. P. *et al.* Structure, folding dynamics, and amyloidogenesis of D76N beta2-microglobulin: roles of shear flow, hydrophobic surfaces, and alpha-crystallin. *The Journal of biological chemistry* **288**, 30917-30930, doi:10.1074/jbc.M113.498857 (2013).
210 Marcoux, J. *et al.* A novel mechano-enzymatic cleavage mechanism underlies transthyretin amyloidogenesis. *EMBO molecular medicine* **7**, 1337-1349, doi:10.15252/emmm.201505357 (2015).
211 Folkman, J. & Hochberg, M. Self-regulation of growth in three dimensions. *The Journal of experimental medicine* **138**, 745-753 (1973).
212 Bornstein, P. & Sage, E. H. Matricellular proteins: extracellular modulators of cell function. *Current opinion in cell biology* **14**, 608-616 (2002).
213 Mishra, D. K. *et al.* Human lung cancer cells grown on acellular rat lung matrix create perfusable tumor nodules. *The Annals of thoracic surgery* **93**, 1075-1081, doi:10.1016/j.athoracsur.2012.01.011 (2012).
214 Sokocevic, D. *et al.* The effect of age and emphysematous and fibrotic injury on the re-cellularization of de-cellularized lungs. *Biomaterials* **34**, 3256-3269, doi:10.1016/j.biomaterials.2013.01.028 (2013).
215 Trautwein, C., Friedman, S. L., Schuppan, D. & Pinzani, M. Hepatic fibrosis: Concept to treatment. *Journal of hepatology* **62**, S15-24, doi:10.1016/j.jhep.2015.02.039 (2015).
216 Schuppan, D., Ruehl, M., Somasundaram, R. & Hahn, E. G. Matrix as a modulator of hepatic fibrogenesis. *Seminars in liver disease* **21**, 351-372, doi:10.1055/s-2001-17556 (2001).
217 Marastoni, S., Ligresti, G., Lorenzon, E., Colombatti, A. & Mongiat, M. Extracellular matrix: a matter of life and death. *Connective tissue research* **49**, 203-206, doi:10.1080/03008200802143190 (2008).
218 Engler, A. J., Sen, S., Sweeney, H. L. & Discher, D. E. Matrix elasticity directs stem cell lineage specification. *Cell* **126**, 677-689, doi:10.1016/j.cell.2006.06.044 (2006).
219 Discher, D. E., Janmey, P. & Wang, Y. L. Tissue cells feel and respond to the stiffness of their substrate. *Science (New York, N.Y.)* **310**, 1139-1143, doi:10.1126/science.1116995 (2005).
220 Nelson, C. M. & Bissell, M. J. Of extracellular matrix, scaffolds, and signaling: tissue architecture regulates development, homeostasis, and cancer. *Annual review of cell and developmental biology* **22**, 287-309, doi:10.1146/annurev.cellbio.22.010305.104315 (2006).
221 Wells, R. G. The role of matrix stiffness in regulating cell behavior. *Hepatology (Baltimore, Md.)* **47**, 1394-1400, doi:10.1002/hep.22193 (2008).
222 Crapo, P. M., Gilbert, T. W. & Badylak, S. F. An overview of tissue and whole organ decellularization processes. *Biomaterials* **32**, 3233-3243, doi:10.1016/j.biomaterials.2011.01.057 (2011).
223 Mazza, G., De Coppi, P., Gissen, P. & Pinzani, M. Hepatic regenerative medicine. *Journal of hepatology* **63**, 523-524, doi:10.1016/j.jhep.2015.05.001 (2015).
224 Guyette, J. P. *et al.* Perfusion decellularization of whole organs. *Nature protocols* **9**, 1451-1468, doi:10.1038/nprot.2014.097 (2014).
225 Orlando, G. *et al.* Discarded human kidneys as a source of ECM scaffold for kidney regeneration technologies. *Biomaterials* **34**, 5915-5925, doi:10.1016/j.biomaterials.2013.04.033 (2013).
226 Gilpin, S. E. *et al.* Perfusion decellularization of human and porcine lungs: bringing the matrix to clinical scale. *The Journal of heart and lung*

transplantation : the official publication of the International Society for Heart Transplantation **33**, 298-308, doi:10.1016/j.healun.2013.10.030 (2014).
227 Baiguera, S., Macchiarini, P. & Ribatti, D. Chorioallantoic membrane for in vivo investigation of tissue-engineered construct biocompatibility. *Journal of biomedical materials research. Part B, Applied biomaterials* **100**, 1425-1434, doi:10.1002/jbm.b.32653 (2012).
228 Rodriguez, F. J. *et al.* Immunoglobulin derived depositions in the nervous system: novel mass spectrometry application for protein characterization in formalin-fixed tissues. *Laboratory investigation; a journal of technical methods and pathology* **88**, 1024-1037, doi:10.1038/labinvest.2008.72 (2008).
229 Perkins, D. N., Pappin, D. J. C., Creasy, D. M. & Cottrell, J. S. Probability-based protein identification by searching sequence databases using mass spectrometry data. *ELECTROPHORESIS* **20**, 3551-3567, doi:10.1002/(SICI)1522-2683(19991201)20:18<3551::AID-ELPS3551>3.0.CO;2-2 (1999).
230 Schmittgen, T. D. & Livak, K. J. Analyzing real-time PCR data by the comparative CT method. *Nat. Protocols* **3**, 1101-1108 (2008).
231 Kong, K., Kendall, C., Stone, N. & Notingher, I. Raman spectroscopy for medical diagnostics--From in-vitro biofluid assays to in-vivo cancer detection. *Advanced drug delivery reviews* **89**, 121-134, doi:10.1016/j.addr.2015.03.009 (2015).
232 Gentleman, E. *et al.* The effects of strontium-substituted bioactive glasses on osteoblasts and osteoclasts in vitro. *Biomaterials* **31**, 3949-3956, doi:10.1016/j.biomaterials.2010.01.121 (2010).
233 Gentleman, E. *et al.* Comparative materials differences revealed in engineered bone as a function of cell-specific differentiation. *Nature materials* **8**, 763-770, doi:10.1038/nmat2505 (2009).
234 Monici, M. Cell and tissue autofluorescence research and diagnostic applications. *Biotechnology annual review* **11**, 227-256, doi:10.1016/s1387-2656(05)11007-2 (2005).
235 Nguyen, T. T. *et al.* Characterization of Type I and IV Collagens by Raman Microspectroscopy: Identification of Spectral Markers of the Dermo-Epidermal Junction. *Spectroscopy: An International Journal* **27**, 7, doi:10.1155/2012/686183 (2012).
236 Notingher, I. & Hench, L. L. Raman microspectroscopy: a noninvasive tool for studies of individual living cells in vitro. *Expert review of medical devices* **3**, 215-234, doi:10.1586/17434440.3.2.215 (2006).
237 Goh, S. K. *et al.* Perfusion-decellularized pancreas as a natural 3D scaffold for pancreatic tissue and whole organ engineering. *Biomaterials* **34**, 6760-6772, doi:10.1016/j.biomaterials.2013.05.066 (2013).
238 Loneker, A. E., Faulk, D. M., Hussey, G. S., D'Amore, A. & Badylak, S. F. Solubilized liver extracellular matrix maintains primary rat hepatocyte phenotype in-vitro. *Journal of biomedical materials research. Part A*, doi:10.1002/jbm.a.35636 (2015).
239 Atala, A., Bauer, S. B., Soker, S., Yoo, J. J. & Retik, A. B. Tissue-engineered autologous bladders for patients needing cystoplasty. *Lancet (London, England)* **367**, 1241-1246, doi:10.1016/s0140-6736(06)68438-9 (2006).
240 Raya-Rivera, A. *et al.* Tissue-engineered autologous urethras for patients who need reconstruction: an observational study. *Lancet (London, England)* **377**, 1175-1182, doi:10.1016/s0140-6736(10)62354-9 (2011).
241 Olausson, M. *et al.* Transplantation of an allogeneic vein bioengineered with autologous stem cells: a proof-of-concept study. *Lancet (London, England)* **380**, 230-237, doi:10.1016/s0140-6736(12)60633-3 (2012).

242 Halliday, P., Sheil, G. R., Bookallil, M. J. & Gaudry, P. L. Preparation of the porcine liver for allotransplantation. *The Australian and New Zealand journal of surgery* **40**, 374-380, doi:10.1111/j.1445-2197.1971.tb04097.x (1971).

243 Badylak, S. F., Taylor, D. & Uygun, K. Whole-organ tissue engineering: decellularization and recellularization of three-dimensional matrix scaffolds. *Annual review of biomedical engineering* **13**, 27-53, doi:10.1146/annurev-bioeng-071910-124743 (2011).

244 Baptista, P. M., Nguyen, V., Atala, A. & Soker, S. Generation of a bioartificial liver using a decellularized whole liver bioscaffold. *Tissue Engineering Part A* **14**, 738-738 (2008).

245 Herling, T. W. *et al.* Force generation by the growth of amyloid aggregates. *Proc. Natl. Acad. Sci. U.S.A.*, doi:10.1073/pnas.1417326112 (2015).